SPECTRAL ANALYSIS FOR NUCLEAR MAGNETIC RESONANCE ACROSS ULTRALOW TO HIGH MAGNETIC FIELDS

A THESIS SUBMITTED TO
THE GRADUATE SCHOOL OF ENGINEERING AND SCIENCE
OF BILKENT UNIVERSITY
IN PARTIAL FULFILLMENT OF THE REQUIREMENTS FOR
THE DEGREE OF
MASTER OF SCIENCE
IN
PHYSICS

By
Ahmed Abdulrahman Ahmed Alzaidi
December 2025

SPECTRAL ANALYSIS FOR NUCLEAR MAGNETIC RESONANCE ACROSS ULTRALOW TO HIGH MAGNETIC FIELDS
By Ahmed Abdulrahman Ahmed Alzaidi
December 2025

We certify that we have read this thesis and that in our opinion it is fully adequate, in scope and in quality, as a thesis for the degree of Master of Science.

Deniz Aybaş(Advisor)

Emre Ozan Polat

Şinasi Barış Emre

Approved for the Graduate School of Engineering and Science:

Orhan Arıkan
Director of the Graduate School

ABSTRACT

SPECTRAL ANALYSIS FOR NUCLEAR MAGNETIC RESONANCE ACROSS ULTRALOW TO HIGH MAGNETIC FIELDS

Ahmed Abdulrahman Ahmed Alzaidi
M.S. in Physics
Advisor: Deniz Aybaş
December 2025

Nuclear magnetic resonance spectroscopy spans magnetic field strengths from conventional high field (1-23 Tesla) to the emerging zero to ultralow field (ZULF) regime. In high-field NMR, Zeeman interactions dominate, yielding spectra characterized by chemical shifts and J-coupling multiplets, with inductive detection providing sensitivity scaling as the square of field strength. In ZULF NMR, J-coupling interactions govern the spin Hamiltonian, with eigenstates described by total angular momentum quantum numbers in the singlet-triplet basis, requiring non-inductive magnetometers such as SQUIDs, Optically Pumped Magnetometers, or Nitrogen-Vacancy centers providing frequency-independent sensitivity in the audio range.

Experimental characterization of dichloromethane around a Tesla magnetic field validates the theoretical framework through systematic evaluation of several fitting approaches, including exponential and oscillating signal methods. Both directly extracted frequency, phase, and relaxation parameters, confirming pulse calibration and validating exponential decay assumptions. Bloembergen-Purcell-Pound relaxation theory successfully predicted molecular relaxation times, with experimental measurements substantially shorter due to field inhomogeneity effects. Correlation time analysis confirmed operation in the extreme narrowing regime across five decades of field strength, achieving close agreement between theory and experiment and validating the inhomogeneity-dominated relaxation mechanism.

Quantum mechanical simulations using QuTiP reproduce experimental free induction decay signals and spectra with high fidelity, with both classical Bloch

equation and quantum Lindblad master equation methods achieving spectral peak agreement within experimental resolution. Multi-field spectroscopic simulations reveal systematic spectral evolution across regimes: at zero and ultralow field, heteronuclear systems exhibit characteristic triplet patterns from pure J-coupling Hamiltonians; the transition regime demonstrates quantum symmetry breaking through center peak splitting; at high field, conventional doublet patterns emerge as Zeeman interactions dominate. Field-dependent analysis across microtesla to Tesla ranges shows that while molecular relaxation remains constant in the extreme narrowing regime, effective coherence times decrease at higher fields due to increasing gradient-induced dephasing.

Keywords: nuclear magnetic resonance, high field, low field.

ÖZET

ÇOK DÜŞÜKTEN YÜKSEK MANYETİK ALANLARA NÜKLEER MANYETİK REZONANS İÇİN SPEKTRAL ANALİZ

Ahmed Abdulrahman Ahmed Alzaidi
Fizik, Yüksek Lisans
Tez Danışmanı: Deniz Aybaş
Aralık 2025

Nükleer manyetik rezonans spektroskopisi, geleneksel yüksek alan (1-23 Tesla) manyetik alan şiddetlerinden yeni ortaya çıkan sıfır ve ultra düşük alan (ZULF) rejimine kadar uzanır. Yüksek alanlı NMR'da Zeeman etkileşimleri baskındır ve kimyasal kaymalar ve J-bağlanma çoklu grupları ile karakterize edilen spektrumlar üretir; endüktif algılama, alan şiddetinin karesiyle orantılı hassasiyet sağlar. ZULF NMR'de J-bağlanma etkileşimleri spin Hamiltoniyenini yönetir ve öz durumlar tekli-üçlü tabanında toplam açısal momentum kuantum sayılarıyla tanımlanır; bu da SQUID'ler, Optik Olarak Pompalanmış Manyetometreler veya Azot-Boşluk merkezleri gibi ses aralığında frekanstan bağımsız hassasiyet sağlayan endüktif olmayan manyetometreler gerektirir.

Tesla manyetik alanı çevresindeki diklorometanın deneysel karakterizasyonu, üstel ve salınımlı sinyal yöntemleri dahil olmak üzere çeşitli uydurma yaklaşımlarının sistematik değerlendirmesi yoluyla teorik çerçeveyi doğrular. Her ikisi de doğrudan frekans, faz ve gevşeme parametrelerini çıkararak puls kalibrasyonunu onaylamış ve üstel bozunma varsayımlarını doğrulamıştır. Bloembergen-Purcell-Pound gevşeme teorisi, moleküler gevşeme sürelerini başarıyla öngörmüş, alan homojenliksizliği etkileri nedeniyle deneysel ölçümler önemli ölçüde daha kısa çıkmıştır. Korelasyon zamanı analizi, beş büyüklük mertebesindeki alan gücü boyunca aşırı daralma rejiminde çalışmayı onaylamış, teori ile deney arasında yakın uyum elde edilerek homojenliksizlik baskın gevşeme mekanizması doğrulanmıştır.

QuTiP kullanılarak yapılan kuantum mekanik simülasyonları, deneysel serbest indüksiyon bozunması sinyallerini ve spektrumlarını yüksek doğrulukla yeniden

üretir; klasik Bloch denklemi ve kuantum Lindblad ana denklemi yöntemlerinin her ikisi de deneysel çözünürlük dahilinde spektral tepe noktası uyumu sağlar. Çoklu alan spektroskopik simülasyonları, rejimler boyunca sistematik spektral evrimi ortaya koyar: sıfır ve ultra düşük alanda hetero-nükleer sistemler saf J-bağlanma Hamiltoniyenlerinden karakteristik üçlü desenler sergiler; geçiş rejimi merkez tepe bölünmesi yoluyla kuantum simetri kırılmasını gösterir; yüksek alanda Zeeman etkileşimleri hakim oldukça geleneksel ikili desenler ortaya çıkar. Mikrotesla'dan Tesla aralıklarına alan bağımlı analiz, moleküler gevşemenin aşırı daralma rejiminde sabit kalırken, etkin koherans sürelerinin artan gradyan kaynaklı faz uyumsuzluğu nedeniyle daha yüksek alanlarda azaldığını göstererek hiçbir tek alan gücünün evrensel olarak optimal olmadığını belirler.

Anahtar sözcükler: nükleer manyetik rezonans, yüksek alan, düşük alan.

Acknowledgement

First and foremost, I extend my deepest gratitude to my advisor, Assist. Prof. Deniz Aybaş, whose unwavering support, guidance, and encouragement have been the cornerstone of my academic journey. Throughout the most challenging periods of my master's studies, she stood by me with patience, understanding, and genuine care that extended far beyond her academic duties. Her mentorship has shaped not only this work but also my development as a researcher. I am profoundly grateful for everything she has done, and words cannot fully express my appreciation for her belief in me when I needed it most.

I would like to express my sincere gratitude to the members of my thesis defense committee, Prof. Şinasi Barış Emre and Assist. Prof. Emre Ozan Polat, for their valuable time, insightful comments, and constructive feedback. Their expertise and careful evaluation have greatly contributed to improving the quality of this work.

To my family, the most precious gift in my life, I owe everything. My father has been my pillar of strength, and without his sacrifices, wisdom, and endless encouragement, I would never have reached this point of success in life. His faith in my abilities has carried me through every obstacle. To my little brother Ajwad and my sister Safa, thank you for the joy, endless love, and motivation you bring into my life. Your presence reminds me of what truly matters.

I am deeply thankful for my dearest friends, Beyza and Rafed, who have been constant sources of support in every sense of the word. Through long discussions, shared struggles, and countless moments of encouragement, they have stood beside me unfailingly. Their friendship has been a source of comfort and strength throughout this journey.

My sincere thanks go to all Aybas lab group members, Silvana and Kubilay, and all my friends in the Physics Department, with whom I have shared both challenging and joyful moments. The collaborative spirit, intellectual exchanges, and

friendships formed during this time have enriched my experience immeasurably.

Finally, I extend my appreciation to the faculty members of the Physics Department for their dedication to teaching and research and for creating an environment conducive to learning and scientific inquiry.

Contents

List of Abbreviations and Symbols **xxviii**

1 NMR ZULF and High-Field **1**

1.1 Conventional High-Field NMR 2

1.2 Ultralow Field NMR 2

1.3 Motivation for Ultralow Field Spectroscopy 3

1.4 Scientific and Technological Applications 4

1.5 Thesis Organization 5

2 Background and Literature Review **7**

2.1 High-Field NMR 7

2.2 Zero to Ultralow Field NMR 15

2.2.1 Selection Rules and Detection Operator 17

2.2.2 Allowed Transitions and Frequencies at ZULF 18

2.2.3 Forbidden Transitions 18

2.3 Coupled Spin Systems: Pople Notation 19

2.4 Perturbation by a Small Longitudinal Field (ULF Regime) 21

2.4.1 Influence on Coherence and Detection 22

2.5 Detection and Instrumentation 23

2.5.1 Inductive Coils 23

2.5.2 Superconducting Quantum Interference Devices (SQUIDs) 27

2.5.3 Optically Pumped Magnetometers (OPMs) 29

2.5.4 The Nitrogen-Vacancy (NV) centers 32

2.6 Magnetic Shielding and Degaussing 35

2.6.1 Passive Magnetic Shielding 35

2.6.2 Shimming 36

2.6.3 Degaussing 37

2.7 Spin Polarization Methods 38

2.7.1 Thermal Prepolarization Using Halbach Magnets 38

2.7.2 Hyperpolarization: PHIP, SABRE, and DNP 39

3 Experimental Methods: Simulation, Signal Processing, and Fitting 41

3.1 Nuclear Spin Relaxation 41

3.1.1 Phenomenological Description: Bloch Equations and Relaxation Times T_1 and T_2 42

3.2 Signal Formation 43
3.2.1 Product Operator Formalism in NMR 43
3.2.2 Time-Domain and Frequency-Domain 51
3.3 Processing and Analysis 57
3.3.1 Zero-Filling and Truncation Artifacts 57
3.3.2 Phase Correction 58
3.3.3 Frequency Discrimination in HF and Multidimensional NMR 58
3.4 Open Quantum Systems: Microscopic Relaxation 60
3.4.1 The Redfield Master Equation 60
3.4.2 The Spectral Density Function 61
3.4.3 Computational Challenges and Optimization 65
3.5 2D NMR spectroscopy 66
3.5.1 High-Field COSY 66
3.5.2 Zero-Field Heteronuclear Correlation 72
3.6 Fitting Procedures 74
3.6.1 Nonlinear Least-Squares Optimization 74
3.6.2 The Levenberg-Marquardt Algorithm 74
3.6.3 Parameter Uncertainty and Goodness-of-Fit 75
3.6.4 Goodness-of-Fit 76

3.6.5 Application to NMR Fitting 76

4 High-Field NMR Experiments 77

4.1 Proton NMR Analysis of Dichloromethane (CH_2Cl_2) 77

4.1.1 Sample Preparation and NMR Acquisition 77

4.2 Free Induction Decay Signal Analysis and Fitting Methods 83

4.2.1 FID Signal in the Lab Frame 83

4.2.2 Magnitude Envelope Fitting Methods 84

4.2.3 Oscillating Signal Fitting Methods 85

4.2.4 Fitting Procedure and Statistical Analysis 86

4.3 Theoretical Framework and Simulation Methods 88

4.3.1 Physical Constants and Molecular Parameters 89

4.3.2 Correlation Time Calculation 89

4.3.3 Dipolar Relaxation Theory 89

4.3.4 Effective T_2^* and Field Inhomogeneity 90

4.3.5 Bloch Equation Simulation 90

4.3.6 Lindblad Master Equation Simulation 91

4.4 Results 92

4.4.1 Experimental FID and Spectral Analysis 92

4.4.2 T_2 Relaxation Analysis and Method Evaluation 94

4.4.3 Oscillating Signal Fitting Analysis 96

4.4.4 Theoretical Relaxation Calculations 100

4.4.5 Analytical Solution with Collapse Operators 100

4.4.6 Simulation Results 106

4.4.7 Experimental vs Simulated Comparison 107

4.5 Analysis 113

4.5.1 Comparison of Magnitude vs Oscillating Fits 113

4.5.2 Non-exponential Decay Character 113

4.5.3 Comparison with Theory 114

4.5.4 Validation of Quantum Simulation 114

4.5.5 Statistical Uncertainties and Fit Reliability 115

4.5.6 Individual Proton Frequency Offset 115

4.6 Conclusions 118

4.7 Magnetic Field Dependence and Advanced Techniques 118

4.7.1 Field-Dependent Relaxation Theory 119

4.8 Multi-Field Analysis: 50 μ T to 3.0 T 120

4.9 Ultra-Low Field NMR Analysis 123

4.9.1 Extreme Narrowing Regime Validation 123

4.9.2 ULF Simulation Parameters 123

4.9.3 Time-Domain and Spectral Analysis 124

4.9.4 Quantum-Classical Equivalence 125

4.9.5 Physical Interpretation 127

4.9.6 Field Dependence Summary 127

5 Multi-Field NMR Spectroscopy of Heteronuclear AX Systems 129

5.1 Introduction 129

5.2 Theoretical Framework 129

5.2.1 Hamiltonian in Different Field Regimes 129

5.2.2 Selection Rules 131

5.2.3 Initial Conditions and Evolution 131

5.3 Simulation Methodology 132

5.3.1 Numerical Implementation 132

5.3.2 Spectral Analysis 132

5.4 Results 132

5.4.1 Four-Regime Spectral Comparison 132

5.4.2 Center Peak Splitting 134

5.4.3 Heteronuclear vs. Homonuclear Systems 135

5.4.4 Discussion 136

5.4.5 Observations 136

6 Conclusions and Future Work **137**

6.1 Key Contributions 137

6.1.1 Theoretical Framework 137

6.1.2 Relaxation Dynamics 138

6.1.3 Fitting Methodologies 138

6.1.4 Quantum Simulation 139

6.1.5 Multi-Field Spectroscopy 139

6.2 Limitations 139

6.3 Future Directions 140

6.4 Concluding Remarks 140

List of Figures

2.1 Schematic depiction of nuclear spin as an inherent angular momentum property. Unlike orbital contributions, this quantum mechanical attribute exists independently of spatial motion. The resulting magnetic moment $\mu = \gamma\mathbf{I}$ constitutes the foundation of NMR phenomena. 9

2.2 Zeeman splitting of nuclear spin energy levels in high-field NMR. Left: In the absence of a magnetic field, the spin states are degenerate. Right: Application of a strong external field B_0 splits the energy levels into two states separated by $\Delta E = \hbar\omega_0 = \gamma\hbar B_0$. The α state (parallel to field, $m_I = +1/2$) has lower energy, while the β state (antiparallel, $m_I = -1/2$) has higher energy. Resonant radiofrequency (RF) radiation at frequency $\nu_0 = \omega_0/2\pi$ induces transitions between these states. 10

2.3 Spin vector dynamics under applied static field. The angular momentum $\vec{I}$ undergoes precessional motion around $\vec{B}_0$ with angular frequency $\omega_0 = \gamma B_0$ (Larmor precession). Quantum eigenstates $|\alpha\rangle = +\frac{1}{2}$ (aligned, lower energy) and $|\beta\rangle = -\frac{1}{2}$ (anti-aligned, higher energy) correspond to distinct precessional trajectories. This semiclassical representation parallels the quantum Zeeman energy-level framework. 11

2.4 Origin of chemical shift in NMR spectroscopy. Left: When an external magnetic field $\mathbf{B}_0$ is applied, the electron cloud surrounding the nucleus circulates, generating an induced magnetic field $\mathbf{B}_{\text{ind}}$ that opposes the applied field (Lenz's law). This nuclear shielding effect produces a local field. Middle: Nuclei in different chemical environments experience different shielding, resulting in distinct resonance frequencies and chemical shifts in the NMR spectrum. Right: The effect of electronic shielding vanishes at zero magnetic field. 13

2.5 Scalar J-coupling between nuclear spins. Top: In the absence of coupling, two chemically distinct nuclei (H_A and H_B) produce single peaks at their respective chemical shifts. Bottom: Scalar coupling mediated through bonding electrons (indicated by coupling constant J) splits each resonance into a multiplet. H_A appears as a doublet due to the two possible orientations of H_B, and vice versa, producing the characteristic doublet-doublet pattern in weakly coupled two-spin systems. 14

2.6 Energy levels for a two-spin system at zero magnetic field. The splitting between the singlet and triplet is set by the scalar coupling J. 17

3.1 Cyclic rotation diagrams for product operator evolution. *I*: Rotation about y-axis (RF pulse with y-phase). *II*: Rotation about x-axis (RF pulse with x-phase). *III*: Rotation about z-axis (chemical shift evolution) 47

3.2 Rotations about the z-axis (precession under chemical shift) . . . 47

3.3 Rotations about the x-axis (RF pulse with x-phase) 48

3.4 Rotations about the y-axis (RF pulse with y-phase) 48

3.5 Nutation of the net magnetization vector $\mathbf{M}$ under the influence of an RF pulse $\mathbf{B}_1$ applied perpendicular to the static field $\mathbf{B}_0$. (Above) At thermal equilibrium, $\vec{M}$ aligns with $\mathbf{B}_0$ along the z-axis. (Middle) During the RF pulse, $\vec{M}$ precesses about $\mathbf{B}_1$, rotating by an angle $\gamma B_1 t$ into the transverse plane. (Bottom right) After the pulse, $\mathbf{M}(t)$ undergoes transverse relaxation (T_2 decay); (Bottom left) longitudinal recovery (T_1), spiraling back towards equilibrium along z. 52

3.6 Nuclear magnetic relaxation. Left: Free induction decay (FID) showing transverse magnetization $M_{xy}(t)$ decaying as $\exp(-t/T_2)\cos(\omega_0 t)$ due to spin-spin relaxation with time constant T_2. The envelope decay rate determines the spectral linewidth. Right: Longitudinal relaxation showing recovery of z-magnetization $M_z(t)$ toward thermal equilibrium following a 90° pulse, characterized by the spin-lattice relaxation time T_1. The recovery reaches 63% of equilibrium magnetization at $t = T_1$. . . . 53

3.7 Distinction between T_2 and T_2^* relaxation. Left: The observed free induction decay exhibits rapid signal loss characterized by T_2^*, which includes both intrinsic molecular relaxation (T_2) and dephasing from magnetic field inhomogeneity. The true molecular transverse relaxation time T_2 (shown by dashed envelope) is longer than the observed T_2^*. The relationship $\frac{1}{T_2^*} = \frac{1}{T_2} + \frac{1}{T_2^{\text{inhom}}}$ separates intrinsic from field-dependent contributions. Right: Longitudinal relaxation T_1 recovery is unaffected by field inhomogeneity and reaches 63% at the characteristic time T_1. 54

3.8 Frequency-domain representation of NMR signal. Fourier transform of the free induction decay produces a Lorentzian lineshape centered at the resonance frequency ω_0. The full width at half maximum (FWHM) is inversely proportional to the effective transverse relaxation time T_2. Longer coherence times produce narrower spectral lines, enhancing frequency resolution. The Lorentzian lineshape arises from the exponential decay envelope of the time-domain signal. 57

3.9 Singlet S_0 population is converted into T_0 coherence and then into transverse magnetization M_x that can be detected at ZULF. . . . 72

3.10 Pulse and field sequence used for heteronuclear zero-field correlation spectroscopy. 73

4.1 Experimental FID processing flowchart. After loading the data, both quadrature conventions ($R+iI$ and $R-iI$) are tested to determine which gives a positive frequency peak. The correct convention is then used for FFT analysis, peak detection, and frequency conversion to the lab frame. Finally, both the magnitude envelope and the oscillating signal fit to extract relaxation and phase parameters. 79

4.2 Overall workflow showing two parallel paths: theoretical prediction (left branch) and experimental analysis (right branch). The simulation path calculates T_2 from first principles, generates FID via QuTiP, and produces normalized spectra. The experimental path processes measured FID through FFT and fitting. Both converge at Stage 5 for direct comparison and visualization. 80

4.3 Complete algorithm flowchart for NMR simulation 88

4.4 Experimental FID signal of CH_2Cl_2 at 1.02 T. Top left: Real component showing oscillations at Larmor frequency. Top right: Imaginary component (quadrature channel). Bottom left: Magnitude envelope showing exponential-like decay. Bottom right: Magnitude on logarithmic scale demonstrating T_2^*-dominated decay over 6.5 s acquisition time. 92

4.5 Frequency-domain analysis of CH_2Cl_2 FID. Top: Magnitude spectrum in rotating frame showing single peak at +30.21 Hz with FWHM = 0.577 Hz. Bottom: Spectrum converted to laboratory frame (236.27 Hz absolute frequency) by adding transmitter offset of 206.06 Hz, demonstrating chemical shift of 5.43 ppm relative to TMS reference. 94

4.6 Comparison of magnitude envelope fitting methods for extracting T_2^* from experimental CH_2Cl_2 FID data. Top: Four models (exponential, bi-exponential, polynomial, shifted power law) fitted to the magnitude envelope. The 10th-degree polynomial (green) achieves highest $R^2 = 0.9999$ but with 11 parameters. Bottom: Residuals showing systematic deviations for exponential models (blue, red) at early times, while polynomial residuals are near zero across the full acquisition window. 96

4.7 Direct fitting of oscillating real FID component using three models: oscillating exponential (5 params, $T_2^* = 0.556$ s), oscillating polynomial (13 params, $T_2^* = 0.640$ s), and oscillating bi-exponential (7 params, weighted $T_2^* = 0.558$ s). All models successfully extract Larmor frequency ($\sim$30.29 Hz) and phase ($\sim -2°$), with polynomial achieving best fit ($R^2 = 0.9996$) at cost of physical interpretability. Exponential model recommended for balance of accuracy and parsimony. 99

4.8 Time-domain comparison: experimental FID (blue) vs. classical Bloch equation simulation (red) for CH_2Cl_2. Top panels: Real and imaginary components showing excellent phase and frequency agreement. Bottom: Magnitude envelope demonstrating accurate $T_2^* = 0.569$ s decay reproduction over 6.5 s acquisition. Simulation uses fitted parameters: Larmor frequency 30.29 Hz, phase $-2.02°$, gradient offset 1.20 rad/s. 108

4.9 Time-domain comparison: experimental FID (black) vs. quantum Lindblad master equation simulation using QuTiP (blue). Two-spin density matrix evolution with transverse collapse operators $\hat{C}_k = \sqrt{2R_2}(\hat{I}_{x,k} - i\hat{I}_{y,k})$ accurately reproduces experimental oscillations and T_2^* decay. Agreement validates quantum mechanical formulation and confirms Lindblad equation reduces to Bloch phenomenology in weak-coupling Markovian limit. 109

4.10 Magnitude envelope: experimental data (blue) vs. Bloch equation simulation (red). Top: Full 6.5 s acquisition showing <5% deviation for $t < 2$ s. Bottom: Semi-log plot demonstrating exponential decay character with $T_2^* = 0.569$ s. Close agreement confirms classical Bloch equations with field inhomogeneity correction ($T_2' = 0.552$ s) capture observed relaxation dynamics without requiring full quantum treatment. 110

4.11 Magnitude envelope: experimental data (blue) vs. QuTiP Lindblad master equation simulation (red). Quantum simulation using two-spin Hilbert space (dimension 4) with Hamiltonian $\hat{H} = \omega_1\hat{I}_{z,1} + \omega_2\hat{I}_{z,2}$ and T_2-relaxation collapse operators matches experimental decay profile. Agreement demonstrates density matrix evolution correctly describes transverse relaxation in liquid-state NMR for magnetically equivalent nuclei. 111

4.12 Frequency-domain validation: experimental spectrum (blue dots) vs. Bloch simulation (red). Both exhibit single Lorentzian peak centered at 30.21 Hz (rotating frame) with identical FWHM = 0.577 Hz, confirming simulated $T_2^* = 0.64$ s input correctly reproduces observed linewidth via $\Delta\nu_{\text{FWHM}} = 1/(\pi T_2^*)$. Peak position validates Larmor frequency calibration; lineshape confirms inhomogeneous broadening model. 112

4.13 Frequency-domain validation: experimental spectrum (blue dots) vs. QuTiP quantum simulation (red). Peak positions coincide at 30.21 Hz with nearly identical Lorentzian lineshapes (FWHM = 0.577 Hz), validating Lindblad formalism with chosen transverse collapse operators $\hat{C}_k = \sqrt{2R_2}\,\sigma_k^-$. Quantitative agreement confirms quantum master equation approach with $R_2 = 1/T_2^* = 1.56\ \text{s}^{-1}$ accurately models dissipative NMR dynamics. 112

4.14 Comparison of simulations with and without individual proton frequency offset. (a) Real part of FID over 0–5 s shows similar oscillation in both cases. (b) Magnitude envelope: both decay with $T_2^* = 0.569$ s, but offset case shows subtle modulation. (c) Zoomed view (2–3 s) reveals beat pattern with $\Delta\omega_B = 1.2$ rad/s (red curve, dashed lines mark beat period = 2.62 s) compared to single-frequency decay with $\Delta\omega_B = 0$ (blue). (d) Zoomed magnitude (1–3.5 s) highlighting the beat modulation amplitude, barely visible because signal has decayed to <10% by the first beat minimum. (e) Difference signal (red minus blue) isolates the beat oscillation, showing ∼4.5 s periodicity. It is similar to background subtraction in spectroscopy: you remove the "uninteresting" common part to highlight what is different between the two cases. The purple trace shows purely the effect of having non-equivalent protons with a small frequency splitting. (f) FFT spectra: the 0.22 Hz splitting from $\Delta\omega_B = 1.2$ rad/s is much smaller than the 0.577 Hz linewidth, producing no visible doublet, just a slightly broader peak. This demonstrates that molecular-scale gradient effects (∼1.77 Å H–H separation) produces subtle interference patterns that are averaged out in the ensemble measurement but are correctly captured by the model. 117

4.15 Field dependence of relaxation times in CH_2Cl_2 from ULF (50 μT) to clinical MRI fields (3.0 T). Blue curve: intrinsic molecular T_2 from BPP theory, nearly constant at 3.5 s across all fields (extreme narrowing regime, $\omega\tau_c \ll 1$). Red curve: observed T_2^* showing dramatic degradation from 3.6 s at ULF to 0.5 s at 3 T due to field-dependent gradient dephasing (orange shaded region). Black dashed line: gradient contribution T_2' scaling linearly with B_0. Key points marked: 50 μT (green, 100% molecular relaxation), 1.021 T (purple, our experimental conditions with $\Delta B_0 = 13.6$ nT), and 3.0 T (red, clinical MRI with 86% gradient loss). The crossover point at ∼100 mT shows where gradient effects begin to dominate. This demonstrates the fundamental ULF advantage: elimination of gradient-induced dephasing without changing molecular physics. 121

4.16 Multi-field comparison of NMR relaxation parameters across five decades of field strength. (a) Molecular T_2 remains constant at 3.5 s (extreme narrowing validation: $\omega\tau_c$ values shown range from 1.3×10^{-5} at 50 μT to 8×10^{-4} at 3 T, all $\ll 1$). (b) Observed T_2^* decreases 7-fold from 3.6 s (ULF) to 0.5 s (3 T) due to gradient scaling. (c) Spectral linewidth (FWHM) increases proportionally with field: 0.091 Hz at 50 μT to 0.637 Hz at 3 T. (d) T_2^*/T_2 ratio quantifies gradient elimination: 1.0 (100%) at ULF approaching the ideal homogeneous limit, degrading to 0.14 (14%) at clinical fields where gradients dominate. This analysis confirms that T_2 field-independence validates BPP dipolar relaxation theory, while T_2^* field-dependence is purely an instrumental effect, demonstrating ULF NMR's advantage in achieving molecular-limited resolution. 122

4.17 ULF FID simulations using classical Bloch equations. Top row: Time-domain signals showing directly observable Larmor oscillations at 2.13, 4.26, and 8.51 kHz. Bottom row: Fourier spectra with Lorentzian peaks centered at respective Larmor frequencies. All signals show identical $T_2 = 3.51$ s decay, confirming extreme narrowing regime where T_2 is field-independent. 124

4.18 Classical Bloch (solid) vs. quantum QuTiP (dashed) at three ULF fields. Top: Real part of transverse magnetization showing kHz-range Larmor oscillations. Bottom: Magnitude envelopes with $T_2 = 3.51$ s decay. Traces overlap with RMS error $< 0.02\%$. 125

4.19 3D visualization of Fourier spectra comparing Bloch (solid lines, $z = 0$ plane) and QuTiP (dashed lines, $z = 1$ plane) simulations. Blue: 50 μT; green: 100 μT; red: 200 μT. Traces overlay perfectly with peak positions matching $\nu_L = \gamma B_0/(2\pi)$ and identical linewidths ($\Delta\nu_{\text{FWHM}} = 0.091$ Hz). Peak height ratio: 0.998 ± 0.003. 126

5.1 Comprehensive comparison of ^{1}H-^{13}C AX system NMR across four magnetic field regimes. Each row represents a different field strength (ZULF, ULF, Transition, High), with columns showing: (a) FID real part, (b) FID imaginary part, (c) FID magnitude with J-modulation, and (d) frequency spectrum with detected peak positions. Note the evolution from triplet (ZULF) to quartet (Transition) to doublet (High field) spectral patterns. The J-coupling modulation period (7.1 ms for $J = 140$ Hz) is clearly visible in the magnitude plots across all regimes. 133

5.2 Zero-field NMR spectra comparison: (left) Heteronuclear AX system ($^1H - ^{13}C$) shows triplet pattern due to observable J-coupling; (right) Homonuclear A_2 system ($^1H - ^1H$) shows single peak at 0 Hz despite identical J-coupling constant. The fundamental difference arises from quantum mechanical exchange symmetry in magnetically equivalent nuclei. 135

List of Tables

2.1 Nuclear spin I as determined by proton (p) and neutron (n) pairing. 8

4.1 NMR Acquisition Parameters 78

4.2 Simulation Parameters for CH_2Cl_2 89

4.3 Frequency Terms and Their Definitions 93

4.4 Comparison of magnitude envelope fitting methods for CH_2Cl_2 FID data 94

4.5 Comparison of oscillating signal fitting methods with phase parameter for direct fitting of real FID signal 97

4.6 Comparison of analytical and numerical Lindblad solutions for two-spin system 105

4.7 Predicted Relaxation Parameters Across Field Strengths 120

4.8 ULF NMR simulation parameters 123

4.9 Bloch vs. QuTiP agreement metrics 125

5.1 Simulation parameters for four magnetic field regimes 132

5.2 Detected peak positions across magnetic field regimes 134

List of Abbreviations and Symbols

AC Alternating Current

COSY Correlation Spectroscopy

DC Direct Current

EMF Electromotive Force

FFT Fast Fourier Transform

FID Free Induction Decay

FLL Flux Locked Loop

FT Fourier Transform

HF High Field

LvN Liouville-von Neumann

MW Microwave

NMR Nuclear Magnetic Resonance

NV Nitrogen Vacancy

ODMR Optically Detected Magnetic Resonance

OPM Optically Pumped Magnetometer

PHIP Parahydrogen-Induced Polarization

ppm Parts Per Million

PTB Physikalisch Technische Bundesanstalt

RF Radio Frequency

SABRE Signal Amplification by Reversible Exchange

SERF Spin Exchange Relaxation Free

SNR Signal-to-Noise Ratio

SQUID Superconducting Quantum Interference Device

STB Singlet Triplet Basis

ULF Ultralow Field

ZULF Zero to Ultralow Field

FWHM Full Width at Half Maximum

B_0 Static External Magnetic Field

B_1 Radio Frequency Magnetic Field

I Spin Quantum Number

$\hat{\mathbf{I}}$ Nuclear Spin Operator

μ Magnetic Dipole Moment

γ Gyromagnetic Ratio

ω_0 Larmor Angular Frequency

ν_0 Larmor Frequency

J Scalar Coupling Constant (in Hz)

J_{ij} Scalar Coupling Constant between spins i and j

δ Chemical Shift (in ppm)

$\mathbf{M}$ Magnetization Vector

M_0 Equilibrium Magnetization

$\mathbf{T_1}$ Longitudinal (Spin Lattice) Relaxation Time

$\mathbf{T_2}$ Transverse (Spin-Spin) Relaxation Time

$\mathbf{T_2}^*$ Effective Transverse Relaxation Time

R_1, R_2 Longitudinal and Transverse Relaxation Rates

$\hat{H}$ Hamiltonian Operator

$\hat{H}_Z$ Zeeman Hamiltonian

$\hat{H}_J$ J Coupling Hamiltonian

$\hat{H}_{DD}$ Dipole-Dipole Coupling Hamiltonian

$\hat{H}_Q$ Quadrupolar Coupling Hamiltonian

$\hat{\rho}$ Density Operator

$\hat{U}$ Unitary Propagator Operator

F Total Angular Momentum Quantum Number

M_F Projection of Total Angular Momentum

$|S_0\rangle$ Singlet State

$|T_0\rangle$, $|T_{\pm 1}\rangle$ Triplet States

τ_c Correlation Time

Φ Magnetic Flux

Φ_0 Magnetic Flux Quantum

β Pulse Flip Angle or Stretching Exponent

ϕ Phase Parameter

$\mathbf{R}^2$ Coefficient of Determination (Goodness of Fit)

ΔE Energy Difference

$\Delta\nu$ Chemical Shift Difference (in Hz)

$\hbar$ Reduced Planck Constant

k_B Boltzmann Constant

T Temperature

t_p Pulse Duration

Δt Dwell Time

f_s Sampling Frequency

D Zero Field Splitting

Q Electric Quadrupole Moment

$A_\parallel$, $A_\perp$ Parallel and Perpendicular Hyperfine Coupling Constants

Chapter 1

NMR ZULF and High-Field

Nuclear magnetic resonance (NMR) spectroscopy is a robust, broad, and non-invasive analytical tool for determining molecular and solid-state structure, local configuration, and quantitative composition [1]. It is fundamentally a branch of spectroscopy [2] based on the resonant absorption of radio-frequency (RF) electromagnetic radiation by a system of nuclear magnetic moments placed in a static external magnetic field (B_0) [3, 4].

NMR relies on nuclei possessing an inherent angular momentum property (nuclear spin) that generates a corresponding magnetic moment (μ) [5]. This magnetic character is present in nuclei having spin quantum number $I \neq 0$, typically those with odd nucleon counts, causing them to act as microscopic magnetic entities [6, 7]. When placed in a static external magnetic field B_0, these magnetic nuclei adopt a discrete set of $2I + 1$ quantized orientations (energy levels) due to the Zeeman effect [8]. For spin 1/2 nuclei (e.g., ^1H,^{13}C), the two energy states, α (lower energy, parallel to B_0) and β (higher energy, antiparallel to B_0), are split by $\Delta E = \hbar\omega_0$, where $\Delta E \propto B_0$ [9].

1.1 Conventional High-Field NMR

Conventional NMR spectroscopy operates in the high-field regime, where strong superconducting magnets generate static magnetic fields ranging from 1 Tesla to over 23 Tesla [8, 10]. At these field strengths, the Zeeman interaction dominates the spin Hamiltonian, and nuclear spins precess at well-defined Larmor frequencies proportional to the magnetic field strength and the gyromagnetic ratio of each nucleus [5]. The resulting chemical shift dispersion, which scales linearly with field strength, enables the resolution of chemically distinct nuclei and provides detailed structural information about molecular systems [9].

The signal-to-noise ratio in high-field NMR scales approximately as $B_0^{3/2}$, while the voltage generated in the receiver coil exhibits quadratic dependence on field strength [8, 11]. This favorable scaling, combined with mature instrumentation and well-established pulse sequences, has made high-field NMR the dominant technique for molecular structure determination in chemistry, biology, and materials science [1]. Detection relies on Faraday induction, where the precessing transverse magnetization induces an oscillating current in a tuned radiofrequency coil positioned perpendicular to the main magnetic field [9, 12].

Despite its widespread success, high-field NMR faces several inherent limitations [13]. The large superconducting magnets require substantial infrastructure, cryogenic maintenance, and significant capital investment [14]. Radiofrequency penetration is severely limited by the skin effect in conductive materials, preventing measurements inside metal containers or reactors [15]. Additionally, magnetic susceptibility broadening in heterogeneous samples can obscure spectral features, particularly in materials with paramagnetic components or multiple phases [16].

1.2 Ultralow Field NMR

Ultralow field (ULF) NMR, which encompasses the range from precisely zero to several microtesla, represents a fundamentally different approach to nuclear

magnetic resonance spectroscopy [13, 17]. At these field strengths, orders of magnitude below Earth's magnetic field of approximately 50 microtesla, the Zeeman interaction becomes negligible compared to internal spin spin couplings, fundamentally altering the physics of spin dynamics [15, 18]. The system eigenstates are no longer individual spin projections but rather states of well-defined total angular momentum, described by singlet and triplet manifolds for two spin systems [4, 19]. Observable transition frequencies arise from scalar J-coupling interactions, whose magnitudes remain invariant across varying field strengths [20].

ULF NMR offers several compelling advantages that complement and extend conventional high-field spectroscopy [13]. First, the extremely narrow spectral linewidths achievable in the ULF regime, often in the millihertz range, enable extraordinarily precise measurement of scalar coupling constants with statistical uncertainties below one millihertz [21, 22]. This precision far exceeds what is achievable at high-field, where frequency spread from chemical shielding variations and spatial field gradients govern linewidth [19]. Second, the low frequency signals (typically in the audio range from DC to several kilohertz) can penetrate conductive materials without attenuation, allowing spectroscopy inside metal containers and enabling applications in reaction monitoring within industrial reactors where high-field NMR is precluded by radiofrequency shielding effects [15, 23]. Third, ULF NMR is largely insensitive to magnetic susceptibility variations, eliminating line broadening in heterogeneous samples that would be problematic at high-field [13, 20].

1.3 Motivation for Ultralow Field Spectroscopy

The motivation for pursuing ULF NMR spectroscopy extends beyond scientific curiosity into practical applications spanning multiple domains [14]. The absence of a large superconducting magnet dramatically reduces the cost, size, and complexity of NMR instrumentation, potentially enabling portable and fieldable spectrometers for applications including quality control, forensics, and point of care diagnostics [16, 24]. The ability to perform spectroscopy inside conductive

enclosures opens new possibilities for in situ chemical reaction monitoring and industrial process control [23].

Furthermore, ULF NMR provides access to unique spin physics unavailable in the high-field regime [19]. Transitions that are forbidden by selection rules at high-field become allowed at zero field, revealing new spectroscopic information about molecular structure and spin topology [15, 17]. The dominance of J coupling interactions over chemical shifts means that ULF spectra directly reflect molecular connectivity patterns, providing complementary structural information to high-field chemical shift data [18].

From a fundamental physics perspective, ULF NMR enables investigation of spin dynamics in the strong coupling regime, where perturbative treatments based on the Zeeman interaction break down [4]. The system must be described by exact diagonalization of the full spin Hamiltonian, and phenomena such as level crossing and avoided crossing become important [13]. These conditions are relevant for understanding spin chemistry, magnetic field effects on chemical reactions, and quantum coherence in biological systems [14].

1.4 Scientific and Technological Applications

The applications of ULF NMR span a diverse range of scientific and technological domains [16]. In analytical chemistry, ULF spectroscopy can determine molecular structure based on scalar coupling patterns, complementing information from high-field chemical shifts [15]. Integration with hyperpolarization methods including PHIP (parahydrogen induced polarization) and SABRE (Signal Amplification by Reversible Exchange) elevates ULF NMR sensitivity to levels permitting investigation of samples with naturally occurring isotope ratios, such as ^{15}N and ^{13}C nuclei [4, 23].

In biochemistry and biophysics, ULF NMR can probe protein structure and dynamics under conditions where high-field measurements are challenging [14].

The insensitivity to magnetic susceptibility effects is particularly advantageous for studying membrane proteins in lipid environments or metalloproteins with paramagnetic centers [13]. The ability to perform measurements inside conductive containers enables studies of biological samples in their native environments without transfer to NMR tubes [25].

In materials science, ULF NMR provides access to relaxometry and field dependent spin dynamics, revealing information about molecular motion and interactions across many orders of magnitude in magnetic field strength [10]. Field cycling experiments, where the sample is transferred between different field regimes, can map out complete relaxation dispersion profiles [26]. ULF detection using highly sensitive magnetometers makes these measurements faster and more efficient than traditional field cycling approaches [13].

From an instrumentation perspective, the development of ULF NMR has driven advances in ultra-sensitive magnetometry, magnetic shielding, and hyperpolarization techniques [19, 27]. Optically pumped magnetometers operating in the spin exchange relaxation free (SERF) regime achieve sensitivities approaching 1 femtotesla per root hertz, rivaling superconducting quantum interference devices (SQUIDs) while operating at room temperature [28, 29]. Quantum sensors utilizing nitrogen-vacancy defects in diamond crystals offer enhanced detection capabilities at sub-micrometer length scales, opening prospects for molecular-level ULF spectroscopy [30, 31].

1.5 Thesis Organization

Chapter 2 develops quantum mechanical foundations for both high-field and ZULF regimes, including Zeeman and J-coupling Hamiltonians, singlet-triplet basis representations, selection rules, and detection methodologies contrasting inductive coils with non-inductive magnetometers (SQUIDs, optically pumped magnetometers, nitrogen-vacancy centers). Coupled spin systems are examined

using Pople notation, and residual field effects on ZULF spectroscopy are analyzed.

Chapter 3 presents nuclear spin relaxation theory (Bloch equations, BPP dipolar relaxation, Redfield theory), signal formation through product operator formalism and density matrix evolution, and computational implementations for both classical and quantum simulations. Practical aspects include initial state preparation, time evolution algorithms, and observable magnetization calculations.

Chapter 4 reports experimental high-field NMR of dichloromethane at 1.021 T, including acquisition parameters, signal processing workflows, and comprehensive fitting analysis comparing magnitude envelope and oscillating signal methods. Dipolar relaxation calculations predict molecular $T_2 = 3.511$ s, validated against measurements. Quantum simulations using Bloch equations and Lindblad master equation reproduce experimental free induction decay signals with time-domain RMS error $<2\%$ and frequency-domain amplitude ratio 0.998 ± 0.003.

Chapter 5 presents ZULF and transition regime simulations for heteronuclear (^{1}H-^{13}C) and homonuclear (^{1}H-^{1}H) systems across four magnetic field regimes (0-200 μT, 50 mT, 1 T, 9.4 T). Spectral evolution from triplet (ZULF) through quartet with 6 Hz center splitting (transition) to doublet (high field) validates theoretical predictions. Quantum-classical equivalence is confirmed within 0.01% at ultralow field.

Chapter 6 synthesizes findings, identifies limitations (single experimental system, ZULF results from simulation only, computational scaling constraints), and proposes future directions including experimental ZULF implementation, extension to complex molecules, 2D correlation spectroscopy, field-cycling relaxometry, and spin echo sequences.

Chapter 2

Background and Literature Review

2.1 High-Field NMR

The conventional NMR (high-field) description is rooted in quantum mechanics, specifically defining the spin system's energy operator, Hamiltonian ($\hat{H}$), and analyzing how the nuclear spins evolve under its influence [8]. In quantum mechanics, angular momentum is quantized, meaning that a rotating molecule exhibits a set of rotational states, making the total angular momentum possess discrete values $L = \sqrt{l(l+1)}\hbar$, where $\hbar$ is the reduced Planck constant, and l is the orbital angular momentum ($l = 0, 1, 2 \dots$) [32]. L determines the rotational speed of the molecule without providing any clues about the rotational axis. l has a projection, in other words, an azimuthal quantum number, m_l, which has integer values $2l + 1 \rightarrow (m_l = -l, -l + 1, \cdots + l)$.

Another form of angular momentum, spin, is not generated by the particle's rotation; however, it is an intrinsic property of a particle, electron, or atomic nucleus. It is difficult to visualize spins since there is no analogy as microscopic spin. Indeed, every atomic nucleus exhibits spin. The total spin angular momentum, S,

takes values proportional to $\sqrt{s(s+1)}\hbar$, where s is the spin angular momentum and has a value of $\frac{1}{2}$ and the spin projection is given by ($m_s = \pm\frac{1}{2}$) [33].

The total angular momentum, J, is a result of the orbit-spin coupling $\mathbf{J} = \mathbf{L} + \mathbf{S}$ and allowed quantum numbers $j = l \pm 1/2$. Its magnitude is given as $J = \sqrt{j(j+1)}\hbar$. Whereas, the total nuclear spin for a whole nucleus is the sum of the total angular momentum of all nucleons, $\mathbf{I} = \sum_i \mathbf{J_i}$, and it is characterized by the nuclear spin quantum number, I. This number is also quantized and takes values of ($I = 0, \frac{1}{2}, 1, \frac{3}{2}, 2\dots$). The nuclear spin operator is denoted $\hat{\mathbf{I}}$ [9]. The value I is related to the atomic and mass numbers based on the pairing of protons and neutrons within the nucleus.

Table 2.1: Nuclear spin I as determined by proton (p) and neutron (n) pairing.

Z	N	**Spin I**	**Condition**
Even	Even	0	The nucleus contains an even number of protons and an even number of neutrons. All nucleon spins are paired. Examples: ^{12}C, ^{16}O.
Even	Odd	$(\frac{1}{2}, \frac{3}{2}, \frac{5}{2}\dots)$	Total nucleon number is odd. Nuclei with an odd mass number have half-integer spin.
Odd	Odd	$(1, 2, 3, \dots)$	Both Z N are odd. Two unpaired nucleons couple to yield an integer total spin. Example: ^{2}H, ^{10}B, ^{14}N

Nuclei with a spin of $I = 0$ have no angular momentum and consequently no magnetic moment, meaning that they are NMR silent [8, 11].

Before applying an external magnetic field B_0, a nucleus with spin I may exist in $(2I + 1)$ discrete energy states, degenerate states (Fig. 2.1). The magnetic moment (μ) of the nucleus is proportional to its spin angular momentum ($\hat{\mathbf{J}}$ or $\hat{\mathbf{I}}$) [5]:

$$\hat{\mu} = \gamma\hat{\mathbf{I}} \quad \text{or} \quad \mu = \gamma\mathbf{J} \tag{2.1}$$

Here, γ is the gyromagnetic ratio (or magnetogyric ratio), a scalar constant specific to each nucleus. For nuclei with $I = \frac{1}{2}$ (^1H, ^{13}C,^{19}F), there are $(2 \cdot \frac{1}{2}) + 1 = 2$ states. These states are conventionally labeled $|\alpha\rangle$ and $|\beta\rangle$ denote spin-up and spin-down along z, respectively. Nuclei with $I > 1$ possess an electric quadrupole moment (Q) in addition to the dipole moment as their charge distribution is not spherically symmetric [34].

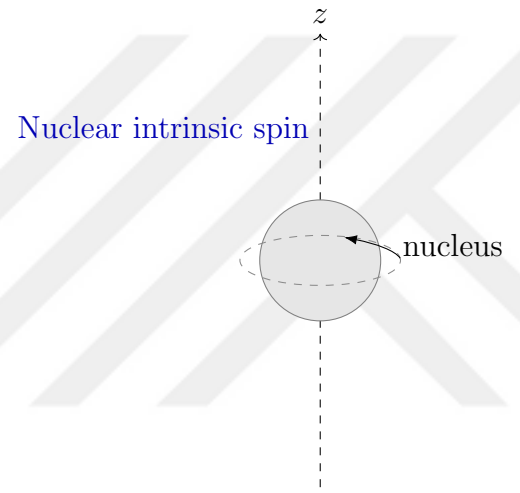


Figure 2.1: Schematic depiction of nuclear spin as an inherent angular momentum property. Unlike orbital contributions, this quantum mechanical attribute exists independently of spatial motion. The resulting magnetic moment $\mu = \gamma \mathbf{I}$ constitutes the foundation of NMR phenomena.

When magnetic nuclei are introduced into a uniform, strong external magnetic field B_0, the state's degeneracy is lifted, and the energy levels split into sublevels $(2I + 1)$. This phenomenon is known as the Zeeman effect, and the separation between the sublevels is called the Zeeman splitting (Fig 2.2).

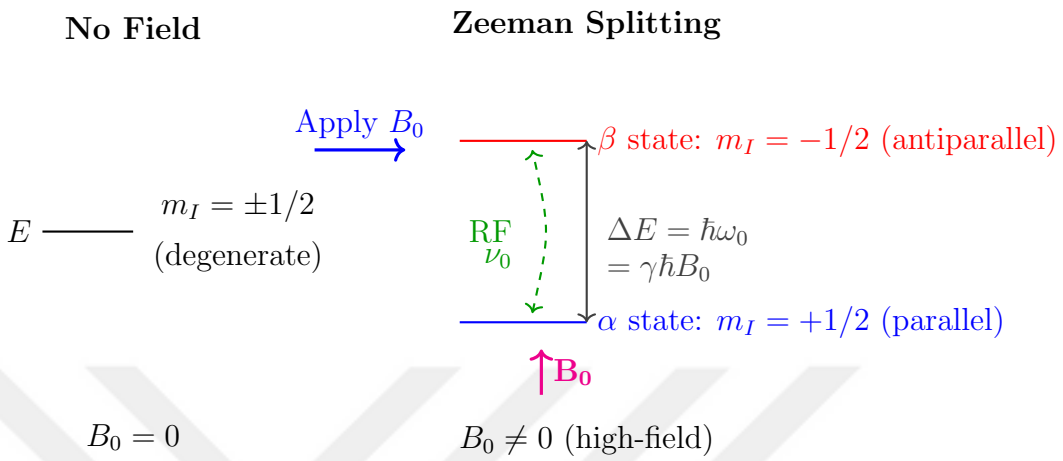


Figure 2.2: Zeeman splitting of nuclear spin energy levels in high-field NMR. Left: In the absence of a magnetic field, the spin states are degenerate. Right: Application of a strong external field B_0 splits the energy levels into two states separated by $\Delta E = \hbar\omega_0 = \gamma\hbar B_0$. The α state (parallel to field, $m_I = +1/2$) has lower energy, while the β state (antiparallel, $m_I = -1/2$) has higher energy. Resonant radiofrequency (RF) radiation at frequency $\nu_0 = \omega_0/2\pi$ induces transitions between these states.

The precession analogy under the static magnetic field can be shown in Figure 2.3 below

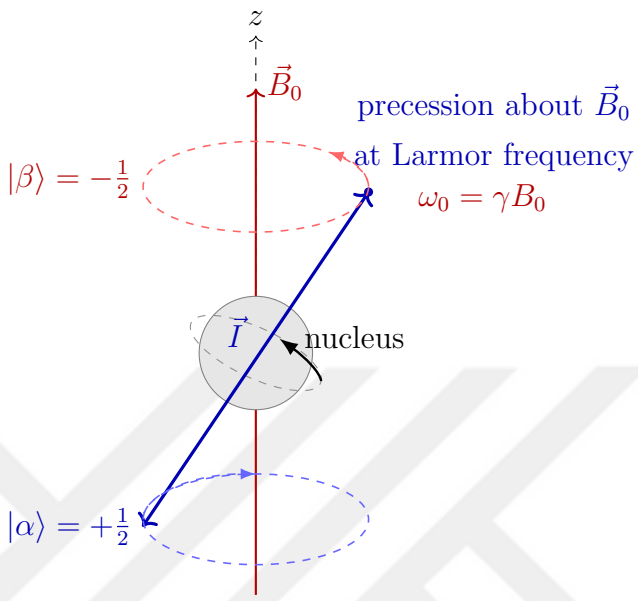


Figure 2.3: Spin vector dynamics under applied static field. The angular momentum $\vec{I}$ undergoes precessional motion around $\vec{B}_0$ with angular frequency $\omega_0 = \gamma B_0$ (Larmor precession). Quantum eigenstates $|\alpha\rangle = +\frac{1}{2}$ (aligned, lower energy) and $|\beta\rangle = -\frac{1}{2}$ (anti-aligned, higher energy) correspond to distinct precessional trajectories. This semiclassical representation parallels the quantum Zeeman energy-level framework.

The potential energy of a nucleus in a magnetic field B_0 is equal to $\mu B_0 cos\theta$, where θ is the angle between the nuclear spin axis and the direction of the external field. The Zeeman Hamiltonian $\hat{H}_Z$ describes the fundamental energy of the nuclear spin magnetic moment μ_I within the strong external magnetic field, B_0. In the high-field regime, where the field is aligned along the z-axis, the Hamiltonian for an isolated spin i is

$$\hat{H}_Z = -\gamma_i \mathbf{B}_0 \cdot \hat{\mathbf{I}}_i \tag{2.2}$$

The energy difference ΔE between adjacent spin states is proportional to the Larmor angular frequency (or precessional frequency) $\omega_0 = \gamma_i B_0$, where the nucleus precesses around the external magnetic field B_0 at this frequency. This simplifies (2.2):

$$\hat{H}_Z = -\omega_{0i} \cdot \hat{\mathbf{I}}_i \tag{2.3}$$

Thus, the frequency of the electromagnetic radiation required to induce transitions between nuclear spin states is exactly equal to the nucleus's Larmor frequency ω_0.

Nuclear spins reside within molecular electron clouds that substantially alter the effective magnetic environment at each nuclear site. Chemical shielding arises when the applied field B_0 drives electronic circulation currents throughout the molecular framework (Fig 2.4). This electron motion produces a secondary magnetic field ($B_{induced}$) oriented opposite to B_0 [6, 8]. Consequently, the nucleus i experiences a local magnetic field $B_{loc,\,i} = B_0(1 - \delta_i)$, where δ_i is the isotropic chemical shielding factor, and it is a dimensionless value, expressed in parts per million (ppm), that is unique to the nucleus's specific chemical environment [17]. The Zeeman Hamiltonian must, therefore, be modified to incorporate the influence of the electronic environment for each nucleus i in the system:

$$\hat{H}_Z = -\hbar \sum_i \gamma_i (1 - \delta_i) \mathbf{B_0} \cdot \hat{\mathbf{I}} \tag{2.4}$$

Here, the term $\omega_{0,i} = \gamma_i B_0(1 - \delta_i)$ represents the chemically shifted Larmor angular frequency of spin i. Since δ_i varies based on the electronic configuration, different chemically distinct nuclei resonate at slightly different frequencies, which is the physical origin of the chemical shift phenomenon crucial for chemical identification [7, 8].

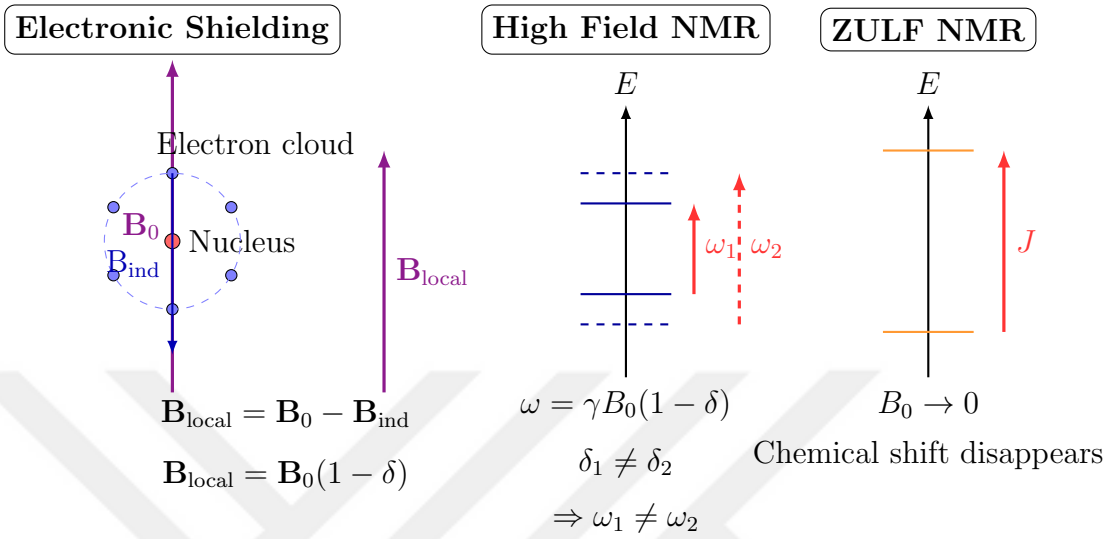


Figure 2.4: Origin of chemical shift in NMR spectroscopy. Left: When an external magnetic field $\mathbf{B}_0$ is applied, the electron cloud surrounding the nucleus circulates, generating an induced magnetic field $\mathbf{B}_{\text{ind}}$ that opposes the applied field (Lenz's law). This nuclear shielding effect produces a local field. Middle: Nuclei in different chemical environments experience different shielding, resulting in distinct resonance frequencies and chemical shifts in the NMR spectrum. Right: The effect of electronic shielding vanishes at zero magnetic field.

The full quantum mechanical description of a system of coupled nuclear spins must also account for interactions "between" the nuclei within the molecule, independent of the external field. For isotropic liquids, the primary internal coupling remaining after averaging by rapid molecular motion is the indirect spin-spin coupling, or $J-$coupling. It describes the energy of interaction between two spins i and j, mediated by the bonding electrons [20]. Its Hamiltonian is expressed as a scalar interaction [15]:

$$\hat{H}_{\text{J}} = 2\pi\hbar \sum_{i>j} J_{ij} \hat{\mathbf{I}}_i \cdot \hat{\mathbf{I}}_j \tag{2.5}$$

The constant J_{ij} is the isotropic scalar coupling constant (expressed in Hz) and provides crucial information about molecular spin topology and connectivity (Fig 2.5). J_{ij} is independent of the external magnetic field strength. The scalar product of the spin operators $(\hat{\mathbf{I}}_i \cdot \hat{\mathbf{I}}_j)$ is expanded as $\hat{I}_{ix}\hat{I}_{jx} + \hat{I}_{iy}\hat{I}_{jy} + \hat{I}_{iz}\hat{I}_{jz}$.

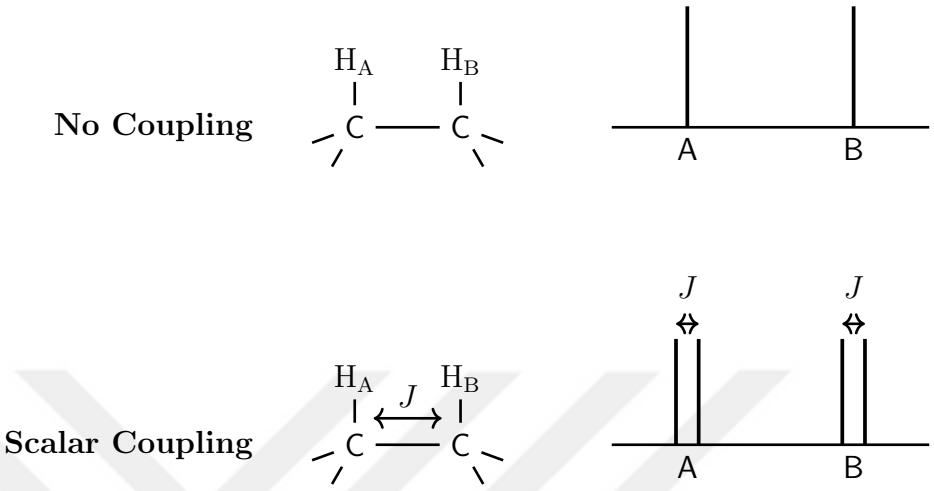


Figure 2.5: Scalar J-coupling between nuclear spins. Top: In the absence of coupling, two chemically distinct nuclei (H_A and H_B) produce single peaks at their respective chemical shifts. Bottom: Scalar coupling mediated through bonding electrons (indicated by coupling constant J) splits each resonance into a multiplet. H_A appears as a doublet due to the two possible orientations of H_B, and vice versa, producing the characteristic doublet-doublet pattern in weakly coupled two-spin systems.

In the high-field regime, the J-coupling is generally treated using the secular approximation, retaining only the $\hat{I}_{iz}\hat{I}_{jz}$ term that commutes with the dominant $\hat{H_Z}$, unless the spins are strongly coupled (the chemical shift difference is comparable to or smaller than the J-coupling magnitude) [15].

The general isotropic spin Hamiltonian, $\hat{H}_{\text{iso}}$, is given by the sum of the Zeeman interaction (including the chemical shift, $\hat{H}_{\text{Z}}$) and the J-coupling Hamiltonian ($\hat{H}_{\text{J}}$):

$$\hat{H}_{\text{iso}} = \hat{H}_{\text{Z}} + \hat{H}_{\text{J}}. \tag{2.6}$$

$$\hat{H}_{\text{iso}} = -\hbar \sum_i \gamma_i (1 - \delta_i) \mathbf{B_0} \cdot \hat{\mathbf{I}} + 2\pi\hbar \sum_{i>j} J_{ij} \hat{\mathbf{I}}_i \cdot \hat{\mathbf{I}}_j. \tag{2.7}$$

For complete generality, especially in anisotropic environments (like solids or liquid crystals), additional interactions must be included in the Hamiltonian. So,

the general Hamiltonian can be represented by

$$\hat{H} = \hat{H}_Z + \hat{H}_J + \hat{H}_{DD} + \hat{H}_Q + \dots \tag{2.8}$$

where Dipole-Dipole Coupling ($\hat{H}_{\mathrm{DD}}$)is the direct through-space magnetic interaction between two nuclear magnetic moments. In isotropic liquids, this term averages to zero. Quadrupolar Coupling ($\hat{H}_{\mathrm{Q}}$) is relevant only for nuclei with spin $I > 1/2$ (quadrupolar nuclei). This electrostatic interaction couples the nucleus's electric quadrupole moment Q with the electric field gradient $\vec{V}$ at the nucleus. In isotropic liquids, the first-order $\hat{H}_{\mathrm{Q}}$ term vanishes, but it remains a dominant mechanism for relaxation.

2.2 Zero to Ultralow Field NMR

Consider a multi-spin isotropic system that contains a single coupled pair of spin-$\frac{1}{2}$ (spin operators $\hat{\mathbf{I}}$ and $\hat{\mathbf{S}}$). The general spin Hamiltonian in the presence of an external magnetic field $\mathbf{B} = B_x\hat{x} + B_y\hat{y} + B_z\hat{z}$ reads

$$\hat{H}_{\mathrm{iso}} = -\gamma_i \mathbf{B}\cdot\hat{\mathbf{I}} - \gamma_j \mathbf{B}\cdot\hat{\mathbf{S}} + 2\pi J_{ij}\hat{\mathbf{I}}\cdot\hat{\mathbf{S}} \tag{2.9}$$

Here γ_i, γ_j are the gyromagnetic ratios of each spin (in units of Hz/T when multiplied by the field), and J, the scalar coupling constant (in Hz). Throughout this section, energies are expressed in frequency units (Hz); when angular-frequency notation is used, the factor 2π is explicitly included.

When the external field is negligible relative to the internal couplings (the ZULF limit) one can set $\mathbf{B} = \mathbf{0}$ and obtain the simplified Hamiltonian [17, 18]

$$\hat{H}_{\mathrm{ZULF}} = 2\pi J\hat{\mathbf{I}}\cdot\hat{\mathbf{S}} = 2\pi J(\hat{I}_x\hat{S}_x + \hat{I}_y\hat{S}_y + \hat{I}_z\hat{S}_z). \tag{2.10}$$

Since the J-coupling term has off-diagonal elements in the Zeeman product basis ($|\alpha\beta\rangle$ and $|\beta\alpha\rangle$), the Zeeman product states are not the eigenstates of the system. Instead, the eigenstates are the linear combinations defined by the singlet-triplet basis , which are also the eigenstates of the total angular momentum

operator $\hat{\mathbf{F}}^2 = (\hat{\mathbf{I}} + \hat{\mathbf{S}})^2$ [4]. In the singlet state (S_0), total spin quantum number is $F = 0$ (non-magnetic), with projection $M_F = 0$. The state is

$$|\mathrm{S}_0\rangle = \frac{1}{\sqrt{2}}(|\alpha\beta\rangle - |\beta\alpha\rangle).$$

A triplet state (T), has a total spin quantum number $F = 1$, comprising three states [35]

$$\begin{aligned} |T_{+1}\rangle &= |\alpha_i\alpha_j\rangle\,, && M_F = +1 \\ |T_0\rangle &= \tfrac{1}{\sqrt{2}}\left(|\alpha_i\beta_j\rangle + |\beta_i\alpha_j\rangle\right), && M_F = 0 \\ |T_{-1}\rangle &= |\beta_i\beta_j\rangle\,, && M_F = -1 \end{aligned} \tag{2.11}$$

At strictly zero field ($B = 0$), the triplet states T_{+1}, T_0, T_{-1} are degenerate (have the same energy), while the singlet state S_0 is separated from them by an energy gap related to the scalar coupling J (in Hz), independent of Larmor frequencies, as shown in Figure 2.6.

One may verify that $\hat{\mathbf{I}} \cdot \hat{\mathbf{S}} = \frac{1}{2}(\hat{\mathbf{F}}^2 - \hat{\mathbf{I}}^2 - \hat{\mathbf{S}}^2)$ and for two spin-$\frac{1}{2}$ particles [32], the operators satisfy

$$\hat{\mathbf{I}}^2 = \hat{\mathbf{S}}^2 = \tfrac{3}{4}\mathbb{1}. \tag{2.12}$$

Hence

$$\hat{\mathbf{I}} \cdot \hat{\mathbf{S}} = \tfrac{1}{2}(\hat{\mathbf{F}}^2 - \tfrac{3}{2}\mathbb{1}). \tag{2.13}$$

Applying this to the total-spin eigenstates gives the eigenvalues directly. For the triplet manifold ($F = 1$)

$$\hat{\mathbf{I}} \cdot \hat{\mathbf{S}}\,|T_m\rangle = \tfrac{1}{2}(1(1+1) - \tfrac{3}{2})\,|T_m\rangle = \tfrac{1}{4}\,|T_m\rangle\,, \tag{2.14}$$

while for the singlet ($F = 0$)

$$\hat{\mathbf{I}} \cdot \hat{\mathbf{S}}\,|S_0\rangle = \tfrac{1}{2}(0(0+1) - \tfrac{3}{2})\,|S_0\rangle = -\tfrac{3}{4}\,|S_0\rangle\,. \tag{2.15}$$

Thus the eigenenergies under Eq. (2.10) are

$$\begin{aligned} E_T &= 2\pi J \times \tfrac{1}{4} = \tfrac{\pi J}{2} \quad \text{(three-fold degenerate)}, \\ E_S &= 2\pi J \times (-\tfrac{3}{4}) = -\tfrac{3\pi J}{2} \quad \text{(singlet)}. \end{aligned}$$

The transition energy between the singlet and triplet manifolds equals

$$\Delta E = E_T - E_S = 2\pi J \quad \Rightarrow \quad \nu_{\mathrm{ZULF}} = J. \tag{2.16}$$

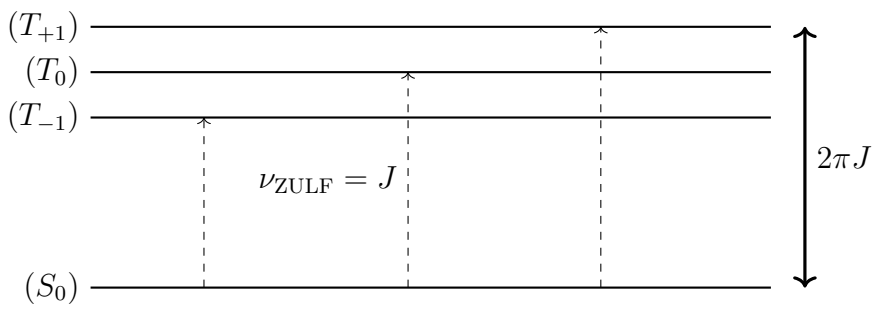


Figure 2.6: Energy levels for a two-spin system at zero magnetic field. The splitting between the singlet and triplet is set by the scalar coupling J.

2.2.1 Selection Rules and Detection Operator

The quantum mechanical framework for describing spin selection rules and allowed transitions in the ZULF regime diverges significantly from the conventional high−field NMR because the spin dynamics are dominated by internal spin−spin couplings ($\hat{H}_J$) rather than the external Zeeman interaction ($\hat{H}_Z$). In this regime, the system's eigenstates are governed by the total angular momentum, and the resultant selection rules dictate which transitions between these coupled states are detectable [15] [18].

Observable NMR transitions are processes that require the absorption or emission of a photon (a spin-1 particle), making them magnetic dipole transitions. Conservation of angular momentum imposes strict quantum mechanical selection rules on the change in total angular momentum and its projection [17]:

1. **Total angular Momentum Selection Rules (ΔF):** For any magnetic dipole transitions, the total angular quantum number F of the spin system must change by 0 or ± 1

2. **Projection Quantum Number Selection Rule (ΔM_F):** The allowed change in the projection quantum number M_F depends critically on the orientation of the excitation or detection magnetic field axis (p) relative to the quantization axis (z). If the observable magnetization $\hat{M}_z$ is detected

(or a z-oriented magnetic field pulse is applied), the projection quantum number must be conserved

$$\Delta M_F = 0$$

If the observable magnetization $\hat{M}_x$ or $\hat{M}_y$ is detected (or a transverse pulse is applied), the projection quantum number must change by ± 1

$$\Delta M_F = \pm 1$$

2.2.2 Allowed Transitions and Frequencies at ZULF

Applying the selection rules to the two-spin system at strictly zero magnetic field ($B = 0$) [17, 18], the critical observable transition in ZULF NMR for a heteronuclear spin pair is the coherence between the singlet state (S_0) and the $M_F = 0$ component of the triplet state (T_0), $S_0 \leftrightarrow T_0$. Since S_0 has $F = 0$ and T_0 has $F = 1$, this transition satisfies $\Delta F = 1$. Since both states have $M_F = 0$, it satisfies $\Delta M_F = 0$. Because the $\Delta M_F = 0$ transition is allowed when measuring magnetization along the z-axis, this transition can be observed using magnetometry. The resonance frequency ν is determined by the energy difference between T_0 and S_0, which, in this simplified two-spin case, is exactly the scalar coupling constant J_{AX} [18].

$$\nu = J_{ij}$$

This zero-field transition, which corresponds to the "flip-flop" or zero-quantum transition ($\Delta M = 0$) at high-field, is generally forbidden in high-field NMR but becomes allowed at ZULF [9].

2.2.3 Forbidden Transitions

The selection rules also reveal why other transitions or spin systems may not be observed: Transitions involving changes between T_{+1} and T_{-1} ($T_{+1} \leftrightarrow S_0$ or $T_{-1} \leftrightarrow S_0$) are generally not observed at $B = 0$ because they violate the $\Delta M_F = 0$ rule for z-detection or the $\Delta M_F = \pm 1$ rule for transverse detection,

respectively [17]. A critical consequence of the magnetization matrix element calculation is that if the two spins are homonuclear (having identical gyromagnetic ratios, $\gamma_i = \gamma_j$), the transition amplitude for all allowed ZULF transitions vanishes (the signal is zero). Therefore, an observable ZULF signal requires heteronuclear coupling (nuclei with different γ's). This is necessary because the signal amplitude is proportional to the square of the difference in gyromagnetic ratios, $(\gamma_i - \gamma_j)^2$ [15].

2.3 Coupled Spin Systems: Pople Notation

The classification of coupled nuclear spin systems is conventionally achieved by using **Pople notation**, an algebraic formalism that organizes nuclei based on their chemical equivalence and the relative magnitude of their chemical shift differences (Δv) compared to their J constants [15]. The notation assigns a capital letter of the Roman alphabet to each magnetic nucleus within a coupled system [7].

Strongly Coupled Systems Nuclei whose chemical shifts (in Hz) are comparable to or smaller than their mutual J constant ($|\Delta v| \leq |J|$) are denoted by adjacent letters early in the alphabet, such as A, B, C, or D [5, 15]. These systems require complex quantum mechanical analysis because the spins are highly interdependent. For example, the AB system describes two coupled nuclei with similar chemical shifts [33].

Weakly Coupled Systems Nuclei that exhibit a large difference in chemical shift compared to their J constant ($|\Delta v| \gg |J|$) are denoted by letters far apart in the alphabet, such as A, M, X, Y, or Z [5, 15]. The most common weakly coupled system is AX. An AMX system denotes three coupled nuclei, all with large chemical shift differences relative to their couplings. Spectra resulting from these systems are referred to as "first-order spectra" and can be analyzed using

simpler, non-quantum mechanical rules [7].

Equivalent Nuclei The notation utilizes subscripts and primes to differentiate between chemically and magnetically equivalent nuclei. Nuclei sharing the same chemical shift are assigned the same letter. Subscripts are used to indicate the number of equivalent nuclei in that group [7, 33]. For instance, the protons in benzene are described as an A_6 system, while the ethyl group protons of ethyl chloride, having different chemical shifts, form an A_3X_2 system (assuming weak coupling, justified by large field strengths) [8]. Two nuclei are considered magnetically equivalent only if they possess identical chemical shifts *and* couple identically to every other nucleus within the spin system. If nuclei are chemically equivalent but fail this latter condition, meaning they have different coupling constants to a third nucleus, they are deemed *magnetically nonequivalent* and are differentiated by adding a prime symbol (A') [33]. A classic example is the $AA'XX'$ system where A and A' (and X and X') are chemically equivalent but magnetically nonequivalent. While possessing only two chemical shifts, such a system involves four distinct coupling constants ($J_{AA'}$, J_{AX}, $J_{AX'}$, and $J_{XX'}$), leading to a complex spectral appearance with potentially up to twenty observable lines [3].

Contextual Dependence of Notation It is crucial to recognize that the classification of a system (as AB versus AX) is dependent on the spectrometer's operating conditions, particularly the strength of the static magnetic field B_0. Since the chemical shift difference ($\Delta\nu$) is directly proportional to B_0, using a spectrometer with a higher field strength increases the $\Delta\nu$ (in Hertz) while the spin-spin coupling constant J remains field-independent. This simplifies complex spectra, transforming them into systems that more closely adhere to first-order rules, thereby reducing the complexity of the quantum mechanical analysis required [33].

Notation under ZULF NMR The conventional Pople notation is fundamentally challenged in the ZULF regime because the high-field criterion for classification—the chemical shift—becomes negligible. By definition, in ZULF NMR, the difference in Larmor frequency between like spins vanishes. Consequently, a modified notation is necessary to describe spin topology, where internal interactions ($J-$couplings) dominate the Hamiltonian [15]. Letters separated widely in the alphabet are reserved *exclusively* for heteronuclear pairs, as their distinction is based on the substantial difference in their gyromagnetic ratios (γ) rather than on chemical shifts. Adjacent letters denote chemically nonequivalent nuclei of the same species. Parentheses are used to group together spins that share the largest coupling constants, defining the topological relationships of the spin system. For a system like XA_n, the homonuclear J-coupling among the equivalent A-spins (J_{AA}) can generally be neglected because observable ZULF NMR transitions occur between states of a common conserved quantum number (K_A), and the transition frequencies within these manifolds do not depend on J_{AA}.

2.4 Perturbation by a Small Longitudinal Field (ULF Regime)

In the case of a two-spin system (XA_n) subjected to an ultralow field (B_{ULF}) along the z-axis, the Hamiltonian $\hat{H}_{\mathrm{ULF,XA}_n}$ includes the zero-field J-coupling Hamiltonian ($\hat{H}_{\mathrm{J,XA}_n}$) and the Zeeman interaction due to the residual field [15]:

$$\hat{H}_{\mathrm{ULF,XA}_n} = \hat{H}_{\mathrm{J,XA}_n} - \hbar \left(\gamma_X \hat{S}_z + \gamma_A \sum_{i=1}^{n} \hat{I}_{z,i} \right) B_{\mathrm{ULF}} \tag{2.17}$$

The Zeeman term is split into commuting and noncommuting parts relative to the dominant $\hat{H}_{\mathrm{J}}$. In the ultralow-field regime, the eigenstates are determined primarily by $\hat{H}_{\mathrm{J}}$, and the Zeeman term $\hat{H}_{\mathrm{Z}}$ is applied as a perturbation. This perturbative Zeeman interaction introduces systematic effects into the energy eigenvalues. The most profound effect of the residual magnetic field is the lifting of the degeneracy of the spin energy sublevels, which leads to observable splitting and shifting of the spectral lines [18].

At strictly zero field ($B = 0$), eigenstates are characterized by the total angular momentum quantum numbers (F_{XA}, I_A, S). Transitions associated with a given F_{XA} state are degenerate with respect to the projection quantum number $m_{F_{XA}}$. The application of a small residual field B_{ULF} lifts this $m_{F_{XA}}$ degeneracy [13]. This is analogous to how a strong field lifts the degeneracy of the $2I + 1$ states for an isolated spin (Zeeman splitting) [15].

Spectral Line Splitting: the lifting of degeneracy manifests spectroscopically as the splitting of the single zero-field resonance peak (which occurs at the J-coupling frequency $v = J_{XA}$ for a simple XA system) [4] into multiple components. As residual field intensity increases, the splitting also increases [13]. The position and structure of the resulting multiplet depend sensitively on the strength and direction of B_{ULF}.

The shift in the energy levels of the $m_{F_{XA}}$ sublevels due to B_{ULF} can be complex. In the first-order approximation, the shift in energy $E^{(1)}$ is linear with B_{ULF} and the projection quantum number $m_{F_{AX}}$. The energy is determined by the zero-field energy plus a linear Zeeman term involving an effective gyromagnetic ratio γ_{AX_n} [15]:

$$E^{(1)}_{F_{AX}(I_A,S)m_{F_{AX}}} = E^{(0)} - \hbar\gamma_{AX_n}(F_{AX}, I_A)B_{\mathrm{ULF}}m_{F_{AX}} \tag{2.18}$$

Beyond the first-order regime, the energy dependence on B_{ULF} is generally non-linear, exhibiting a quadratic Zeeman splitting term.

2.4.1 Influence on Coherence and Detection

The residual field not only dictates the system's coherent dynamics but also impacts the experimental measurement constraints, such as coherence and low-frequency resonances.

At zero field, polarization oscillates between coupled spins ($\hat{I}_{Az}$ to $\hat{I}_{Xz}$) along the initial polarization axis at the J-coupling frequency, rather than precessing.

However, the application of a small disturbance field, B_{ULF}, overlays this oscillation with spin precession transverse to the magnetic-field plane [17, 18].

The residual magnetic field lifts the degeneracy of transitions where the total angular momentum quantum number remains unchanged ($\Delta F_{XA} = 0$). At a strict zero field, these transitions manifest only as static magnetization at zero frequency (DC signal). When the degeneracy is lifted by B_{ULF}, these transitions give rise to slowly oscillating magnetic fields, known as low-frequency resonances, whose frequencies are exclusively determined by the magnitude of the magnetic field [15].

2.5 Detection and Instrumentation

The distinct nature of high-field and ZULF NMR necessitates fundamentally different approaches to signal detection. While high-field NMR relies on the established principles of electromagnetic induction, ZULF NMR, operating far below the Larmor frequencies for effective induction, leverages highly sensitive magnetometers [23, 16]. Below is the detailed elaboration on the primary detection modalities utilized in both regimes, focusing on Inductive Coils, Superconducting Quantum Interference Devices (SQUIDs), Optically Pumped Magnetometers (OPMs), Spin-Exchange Relaxation-Free (SERF) regime, and Nitrogen-Vacancy (NV) centers.

2.5.1 Inductive Coils

The methodology for detecting NMR signals in the high-field regime is based on the principle of electromagnetic induction, a robust process codified by Faraday's law. This approach is highly efficient for the high Larmor frequencies characteristic of modern high-field spectrometers, which operate using powerful superconducting magnets [8, 9, 5].

The first step of the NMR experiment is establishing the bulk nuclear magnetization [12]. This begins by immersing the sample in a strong, homogeneous, and uniform magnetic field B_0 [8, 9]. The applied field B_0 creates an energy difference ΔE between the nuclear spin states, which ΔE is proportional to B_0 and the nucleus's gyromagnetic ratio (γ). Since the proton spin energy is minuscule compared to the thermal energy scale (kT) at room temperature, only a slight excess of nuclei are aligned with the magnetic field according to the Boltzmann distribution [3, 36]. For spin with $I = \frac{1}{2}$, this population imbalance generates the magnetization vector, M_0, which lies along the direction of B_0 (conventionally the z-axis). Due to the immense quantity of nuclei present (on the order of Avogadro's number), this magnetization M_0 is sufficient to be measured, even if the excess polarization is only a few parts per million (ppm).

For detection via induction, M_0 must first be manipulated to produce a time-varying magnetic field. This is achieved by applying a radiofrequency (RF) pulse, which is tuned to the nuclear Larmor frequency ($\omega_0 = \gamma B_0$). , a 90° pulse is used to rotate the longitudinal magnetization (M_z) into the transverse xy plane.

Once tipped, this resulting transverse magnetization precesses coherently about the main field B_0 at the Larmor frequency. This precession produces an oscillating magnetic field. Since the precession is extremely fast (in modern spectrometers, the Larmor frequency for protons can be hundreds of MHz, 500 MHz for an 11.74 T magnet), the longitudinal component's contribution to the time derivative of the magnetic flux is negligible [1, 9].

The detection itself is a direct consequence of Faraday's law of induction ($\nabla \times E = -\partial B/\partial t$) [12]. This rotating transverse magnetization "cuts" across the detection coil, generating a changing flux. Thus, a change in flux induces a small electromagnetic force (emf) and, consequently, an oscillating current in the coil windings. This induced signal, referred to as the NMR signal or Free Induction Decay (FID), is then amplified and digitized. The concept is analogous to how electric current is generated by a rotating magnet inside a coil, such as in a bicycle dynamo [9].

2.5.1.1 Instrumentation and Optimization

The physical coil assembly, referred to as **probe**, is significant for maximizing the weak induced signal.

1. **Coil Geometry and Tuning:** For maximum sensitivity, the receiver coil must be positioned as close to the sample as possible. Crucially, the coil's winding axis must be oriented perpendicular to the main static field B_0 to effectively capture the changing flux generated by the transverse magnetization precession [8, 9, 5].

2. **The Tuned Circuit:** The detection coil operates within a resonant LC circuit that incorporates capacitive elements (including the tuning capacitor, C_T). By adjusting both the inductive and capacitive components, the circuit achieves resonance at the nuclear Larmor frequency of interest. This resonant condition amplifies the signal amplitude substantially and efficiently captures energy from the oscillating transverse magnetization. Given that each nuclear species possesses a distinct resonance frequency, dedicated tuned circuits typically target individual isotopes, though sophisticated designs permit frequency multiplexing on a single coil assembly [2, 8, 9].

3. **Signal Transmission and Receiver:** The same coil serves the dual function of transmitting the RF pulse (B_1) and receiving the subsequent FID. In modern Fourier Transform (FT) NMR, the received RF signal, which oscillates at hundreds of MHz, is mixed with the reference carrier frequency (the transmitter frequency) to shift it down to a manageable low frequency range (a process called frequency down conversion) before digitization [9, 18]. To distinguish signals precessing slightly faster versus slightly slower than the reference frequency, modern spectrometers employ "quadrature detection," using two phase-sensitive detectors offset by 90°, thereby improving the signal-to-noise ratio (SNR) by a factor of approximately $\sqrt{2}$ [3].

4. **Cryogenic Enhancement:** To further combat the inherent weakness of

the NMR signal (with sensitivity being a significant limitation of the technique), advanced systems utilize cryoprobes. These probes cool the electronic circuits, such as the coil and preamplifier, to cryogenic temperatures ($\sim$ 20 K), thereby minimizing electronic noise and improving signal detection efficiency [8].

2.5.1.2 Scaling of Signal and Sensitivity in high-field

The induced electromotive force (emf) is proportional to both the Larmor frequency (ω_0) and the magnitude of the magnetization (M_0). Since $\omega_0 \propto B_0$ and $M_0 \propto B_0$, the resultant signal amplitude scales roughly as the square of the static field strength (B_0^2) [11, 19]. While the signal amplitude increases as B_0^2, the electronic noise generated by the instrument's circuit components also increases linearly with B_0. Consequently, the resultant signal-to-noise ratio (SNR), the more critical quantity for practitioners, is generally proportional only linearly to the static field strength (B_0). More broadly, the SNR scales approximately as $|\gamma|^{5/2}(B_0)^{3/2}$ for a given sample [8]. The increase in sensitivity with increasing magnetic field is a fundamental advantage [10]. Furthermore, chemical shift dispersion, which is essential for resolving molecular structure, also increases linearly with field strength, enhancing spectral resolution. The development of superconducting solenoids has been paramount in increasing the sensitivity of NMR equipment by boosting the absorbed quanta and polarization [5].

Although inductive coils dominate high-field detection, their sensitivity severely degrades at low frequencies, making them impractical for ZULF NMR spectroscopy [25]. Because the emf is proportional to $\partial B/\partial t$, the sensitivity of inductive coils scales linearly with the signal frequency. At ZULF conditions (microtesla fields or below), the Larmor frequencies drop into the audio band (Hz to kHz). At these low frequencies, the signal strength is too weak for inductive detection to be practical or efficient. This necessity led to the development of non-inductive detection modalities for ZULF, such as SQUIDs and OPMs, which measure the magnetic field directly and whose sensitivity is broadly independent of frequency [10, 14, 26]. Notably, SQUIDs and OPMs surpass the sensitivity of

inductive coils (below 1–10 MHz) [19].

2.5.2 Superconducting Quantum Interference Devices (SQUIDs)

As a methodology for sensing nuclear magnetization, ZULF NMR requires highly specialized, non-inductive detectors because the characteristic low Larmor frequencies (Hz to kHz) fall into a regime where conventional Faraday inductive coils lack sufficient sensitivity [4, 15, 16]. Among these advanced sensors, SQUIDs have historically played a crucial role in enabling ZULF detection due to their unparalleled sensitivity and broadband frequency response [14]. They are recognized as the most sensitive devices available for detecting magnetic flux (Φ). Their operation is predicated on fundamental quantum mechanical phenomena occurring in superconducting circuits, flux quantization, and the Josephson effect [27]. In a closed superconducting loop (maintained below its critical temperature, T_c), the magnetic flux threading the loop is quantized, meaning it must be an integer multiple of the magnetic flux quantum (Φ_0).

A DC SQUID consists of a superconducting ring interrupted by two Josephson tunnel junctions. These junctions allow the passage of Cooper pairs via tunneling. The voltage generated across the SQUID is periodic and highly sensitive to the external magnetic flux (Φ_{ext}) threading the loop [27].

The SQUID system measures Φ directly and converts it into a measurable voltage. SQUIDs are operated within a Flux-Locked Loop (FLL) feedback circuit, which linearizes the flux-to-voltage characteristic and significantly increases the working range and stability. For practical NMR measurements, a pickup coil, configured as a gradiometer, is inductively coupled to a current-sensing SQUID. This allows the detection system to register the oscillating magnetic field produced by the nuclear spins in the sample ($\mathbf{M}(t)$ [17, 22].

2.5.2.1 Sensitivity and Broadband Detection

1. **Frequency Independence:** Unlike in high-field NMR (the signal voltage is scaled with the rate of change of magnetic flux and thus is proportional to the Larmor frequency [25]), SQUIDs directly measure magnetic flux (Φ). Their sensitivity remains nearly constant across a vast frequency spectrum, from DC up to gigahertz (GHz). This broadband, frequency-independent nature is what enables the effective detection of ZULF signals, which range from DC to 1 kHz, or occasionally slightly higher. SQUID's sensitivity surpasses that of inductive coils for signal frequencies below 1-10 MHz [26].

2. **Noise Level:** SQUID magnetometers currently demonstrate unmatched sensitivity performance, exhibiting noise floors near 1 $fT/Hz^{1/2}$. Advanced gradiometric SQUID configurations reach white noise densities approaching 0.1 $fT/Hz^{1/2}$ [4, 28]. For ZULF spectroscopy applications at Germany's national metrology institute PTB (Berlin), custom-designed single-channel SQUID sensors operating in cryogenic environments have demonstrated exceptional noise suppression down to approximately 200 $aT/\sqrt{Hz}$ (atto = 10^{-18}) [22].

2.5.2.2 Indirect Detection and Field Cycling

SQUIDs are being utilized in field cycling approaches, although the primary direct-detection method for ZULF signals now involves highly sensitive magnetometers. Field cycling experiments, which measure spin evolution under ZULF conditions by repeatedly transferring the sample to a high-field for inductive detection, have historically been cumbersome. SQUIDs provide an alternative direct measurement method, eliminating the need for repeated shuttling back to a high-field coil for readout [15, 13].

2.5.3 Optically Pumped Magnetometers (OPMs)

Optically Pumped Magnetometers (OPMs) have revolutionized the field of ZULF NMR, providing a highly sensitive, non-inductive detection mechanism ideally suited for challenges in measuring signals at audio frequencies (Hz to kHz) [15, 16].

In the ZULF regime, the nuclear spin precession frequencies are extremely low. As mentioned in the earlier section, the inductive coil for high-field signals exhibits insufficient sensitivity because their induced signal strength is proportional to the rate of change of magnetic flux and therefore scales linearly with frequency [37]. OPMs overcome this limitation by directly sensing the magnetic field produced by nuclear magnetization, offering sensitivity that is largely independent of frequency, down to DC [18].

OPMs rely on exploiting the magnetic sensitivity of highly spin-polarized alkali-metal atoms, such as Rubidium (Rb^{87}), Cesium, or Potassium, confined within a vapor cell [38]. The detection process can be illustrated as follows:

1. **Optical Pumping:** Circularly polarized light (the pump beam) is used to excite the alkali atoms, preferentially driving them into a specific spin state. This procedure polarizes the electron spins of the atoms, creating a highly spin-ordered ensemble.
2. **Spin Dynamics and Magnetization Detection:** The presence of an external magnetic field, such as the oscillating field generated by the NMR sample ($\mathbf{M}(t)$), causes the polarized atomic spins to precess (Larmor precession) or, more generally, influences their spin state dynamics [4].
3. **Optical Readout (Probing):** The magnetometer detects these changes optically. A separated light beam (the probe beam), linearly polarized and tuned slightly off-resonance (or using the same pump beam in certain configurations), is passed through the vapor cell. The magnetic field experienced by the atoms causes changes in the light's properties, measured using a photodiode or a polarimeter. This technique effectively links the nuclear spin dynamics in the sample to a measurable optical signal [19].

2.5.3.1 The SERF Regime for High Sensitivity

The highest performance in OPMs is generally achieved by operating them in the Spin-Exchange-Relaxation-Free (SERF) regime [24]. To operate under this regime, the magnetic field must be extremely low (below $\sim 100 \quad nT$ for Rb^{87}). Simultaneously, the alkali vapor cell must be heated to a high temperature, exceeding $100°C$ (up to 150-200 $°C$) to achieve a high density of alkali atoms.

In high-density alkali vapors, spin-exchange collisions among the atoms are rapid and cause spin relaxation, limiting sensitivity. However, when the magnetic field is near zero, these collisions are suppressed, allowing the electron spins to maintain their polarization longer, resulting in an ultranarrow magnetic resonance linewidth and maximal sensitivity. Indeed, SERF magnetometers are optimized for ZULF; therefore, they require careful shielding and shimming of residual fields to maximize their performance [29].

2.5.3.2 OPM Sensitivity and Bandwidth Performance

OPMs can achieve sensitivity levels comparable to, or even surpassing, those of SQUIDs. SERF OPMs reach sensitivities of 1-10 $fT/Hz^{1/2}$. Commercial sensors operate around 15 $fT/Hz^{1/2}$ [16]. OPM sensitivity can be limited by low-frequency $1/f$ noise and external interference, notably power-line harmonics. Those that operate in the SERF regime generally have a narrower bandwidth compared to SQUIDs, although certain designs can reach bandwidths exceeding 200 Hz or even higher [13].

2.5.3.3 Advantages of OPMs for ZULF NMR Detection

1. **No Cryogenic:** Unlike SQUIDs, which require liquid helium for operation, OPMs work at or above room temperature (requiring only the heating of the vapor cell). This significantly reduces the cost, complexity, and logistical barriers associated with cryogenic equipment [24].

2. **Portability:** OPM systems are compact and simple to assemble and maintain, making portable and fieldable ZULF NMR spectrometers feasible. Microfabricated OPMs can be extremely small, enabling miniaturized devices [27].

3. **accessibility:** The development and commercial availability of robust, ready-to-use OPMs, such as QuSpin Zero-Field Magnetometers (QZFM), have made ZULF NMR accessible to researchers without specialized expertise in atomic physics or optics [25].

4. **Integration:** OPM sensors can be placed in close proximity to the sample (a standoff distance of approximately 9.5 mm from the sensor cell to the center of the NMR tube), which is crucial for maximizing the detection of the rapidly decaying magnetic field generated by the sample. They can also be used in arrays for sophisticated common-mode noise rejection and spatial resolution [13].

2.5.3.4 ZULF NMR Applications Using OPMs

1. **High-Resolution Spectroscopy:** OPMs enable the direct detection of $J-$coupling spectra in zero field, yielding narrow resonance linewidths (0.1 Hz) that permit high-resolution measurement of scalar-coupling constants with statistical uncertainty in the mHz range [21].

2. **Hyperpolarization Enhancement:** OPM detection is frequently paired with hyperpolarization techniques, such as parahydrogen-induced polarization (PHIP) and signal Amplification by Reversible Exchange (SABRE), to overcome the intrinsically low thermal polarization at zero field [23]. This allows for the study of natural abundance samples (0.36 $\%N^{15}$) and low-concentration biomolecules.

3. **Chemical Analysis and Reaction Monitoring:** OPMs facilitate chemical analysis based on molecular spin topology and J-couplings. A notable advantage is the ability of ZULF NMR signals to pass through conductive

materials like metal enclosures, enabling reaction monitoring within industrial reactors, where high-field NMR would fail due to the skin effect [15].

4. **Relaxometry:** OPMs support specialized ZULF NMR techniques, such as relaxometry and field-dependent studies, allowing the measurement of spin dynamics and relaxation times (T_1 and T_2processes) at ultralow fields. Additionally, they have been used to track spin dynamics during adiabatic field sweeps used in hyperpolarization conversion [17].

5. **Field-Cycling Correlation:** While OPMs perform direct ZULF detection, indirect methods involving field cycling sometimes correlate the ZULF evolution (encoded in t_1) with high-field detection (by inductive coil) in the direct dimension, exploiting the high sensitivity of high-field detection for readout. However, OPMs provide an alternative, direct ZULF measurement that is much faster than the point-by-point acquisition required by traditional field-cycling methods [10].

2.5.4 The Nitrogen-Vacancy (NV) centers

The NV center is a point defect in the diamond lattice, composed of a substitutional nitrogen atom adjacent to a vacancy, which is utilized in the negatively charged state (NV^-). Its utility as a magnetic sensor stems from its electronic ground state, which is a spin-triplet (S=1) $^3A_2$ state, separated by a zero-field splitting of D$\approx$ 2.87 GHz between the $m_s = 0$ and $m_s = \pm 1$ sublevels [27, 30].

The integration of NV centers in diamond represents a highly sophisticated and promising, though still maturing, modality for ZULF NMR detection, particularly appealing for applications requiring extreme spatial resolution [19].

As quantum sensors, NV centers possess several inherent advantages, including stability at room temperature, which eliminates the cryogenic requirements associated with SQUIDs, and high spatial resolution, making them prime candidates for pushing NMR down to the single-molecule regime [39]. The signal production can be summarized as shown below:

1. **System Initialization:** The spin state is optically manipulated. The NV center can be efficiently polarized into the $m_s = 0$ sublevel by illumination with green light (532 nm laser, a non-resonant excitation source). The spin state is read out via spin-dependent fluorescence: the $m_s = 0$ state exhibits high fluorescence intensity, while the $m_s = \pm 1$ states decay predominantly through intersystem crossing (ISC) to singlet states, resulting in lower fluorescence [27, 40].

2. **Optically Detected Magnetic Resonance (ODMR):** The transition frequency between $m_s = 0$ and $m_s = \pm 1$ sublevels is sensitive to external fields (Zeeman effect). ODMR is employed by applying microwave (MW) radiation that is resonant with these transitions. When the MW frequency matches the resonance, it transfers population to the low-fluorescence $m_s = \pm 1$, causing a detectable drop in fluorescence intensity. This mechanism forms the basis for NV magnetometry [30].

3. **NV Hamiltonian:** The ground state spin Hamiltonian includes three main terms [31]: the electron spin Hamiltonian ($\hat{H}_S$), the nuclear spin Hamiltonian ($\hat{H}_I$), and the electron-nuclear spin interaction Hamiltonian ($\hat{H}_{SI}$) [30]:

$$\begin{aligned} \hat{H} &= (D\mathbf{S_z^2} + \gamma_e \mathbf{B_0} \cdot \mathbf{S}) \\ &+ (\mathbf{P}\mathbf{I_z^2} - \gamma_n \mathbf{B_0} \cdot \mathbf{I}) \\ &+ (\mathbf{A}_\parallel \mathbf{S_z} \mathbf{I_z} + \mathbf{A}_\perp (\mathbf{S_x} \mathbf{I_x} + \mathbf{S_y} \mathbf{I_y})) \end{aligned} \tag{2.19}$$

   where, B_0 is the external field, D is the zero-field splitting of the ground state, $\mathbf{S}$ is the vector of electron spin matrices $[S_x, S_y, S_z]$ for an S=1 system, and γ_e is the electron gyromagnetic ratio. $\mathbf{P} \approx \mathbf{-5.01}$ MHz is the nuclear quadrupole moment of ^{14}N, $\mathbf{I}$ is the vector of nuclear matrices $[I_x, I_y, I_z]$ for I=1, and γ_n is the nuclear gyromagnetic ratio of the ^{14}N. Finally, $\mathbf{A}_\parallel = 2.14$ MHz and $\mathbf{A}_\perp = 2.7$ MHz are the parallel and perpendicular components of the hyperfine tensor with respect to the NV^- center axis, respectively. The ODMR transition frequencies, $v_\pm$, depend on B_0 applied along the NV axis.

2.5.4.1 NV centers for ZULF and Single-Molecule Spectroscopy

The primary motivation for incorporating NV centers into ZULF NMR originates from the unprecedented combination of sensitivity and nanoscale spatial resolution that they offer.

NV centers are considered strong candidates for achieving single-molecule ZULF J-spectroscopy. This concept envisions a single NV center, positioned just a few nanometers below the diamond surface, detecting the signal from a neighboring analyte molecule. Decisively, this ultra-small volume detection can utilize statistical polarization (stochastic polarization), where the signal size is determined by the natural $\sqrt{N}$ excess of spins in the small ensemble, bypassing the need for extensive hyperpolarization techniques required for bulk ZULF samples [14].

2.5.4.2 Practical Implications and Limitations

- While NV sensing protocols rely on applied bias fields, novel schemes have been developed, such as robust pulse sequences optimized for zero and low fields using a linearly polarized microwave field, which allow for the sensing of weak AC magnetic fields. Detection of ZULF NMR signals with NV centers has also been achieved recently [39].

- Although NV centers offer high intrinsic sensitivity and can operate at room temperature, they are "not yet competitive with respect to sensitivity" for bulk liquid-state ZULF NMR when compared to state-of-the-art instruments using OPMs or SQUIDs. Also, many uses of NV magnetometry rely on microwave-induced ODMR. These high-power MWs can interfere with certain samples (biological systems, thin conductive materials). For ZULF applications, where low frequencies are detected, alternatives are being explored [41].

- Microwave-free imaging magnetometry utilizing NV centers at near-zero fields has been demonstrated, leveraging cross-relaxation features in the

fluorescence spectrum. This all-optical method could be highly beneficial for ZULF NMR studies where microwaves are invasive [41].

- For nanoscale NMR detection of liquid samples using NV centers, the spectrum is prone to broadening due to fast molecular diffusion. The correlation times required for high-resolution spectroscopy are limited by the rapid movement of the molecule across the sensitive NV region (a few nanometers), necessitating strategies for molecular confinement, such as molecular cages or optical trapping [14].

The development of NV-diamond magnetometers, along with OPMs and SQUIDs, continues rapidly, and the potential applications of NV centers are expected to change dramatically in the coming years, potentially offering an unparalleled range of mass sensitivity.

2.6 Magnetic Shielding and Degaussing

The core challenge in ZULF NMR is eliminating the ambient magnetic environment, including the static geomagnetic field (Earth's field) and time-varying magnetic noise (such as 50/60 Hz mains hum) originating from the laboratory. This is achieved using passive magnetic shielding [19, 18].

2.6.1 Passive Magnetic Shielding

High-quality ZULF systems employ multiple concentric layers (three to five layers) of highly permeable material, $mu-metal$. These shields collectively attenuate the ambient field [19]. Passive shielding is designed to attenuate the external field by a significant factor, ranging from 10^5 to 10^6, or sometimes to 10^4. This reduces the residual field inside the detection region to extremely low levels, below 1 nT [4]. In sophisticated setups, an innermost layer consists of ferrite material.

This is crucial because it minimizes the magnetic noise generated by **Johnson currents** within the conductive mu-metal layers themselves [23].

The absence of a strong applied field means that ZULF spectra are largely unaffected by variations in magnetic susceptibility in heterogeneous samples (a major advantage over high-field NMR). This shield's primary role is to ensure high *absolute* field homogeneity, which leads to ultra-narrow spectral linewidth, sometimes down to mHz levels, enabling high-precision measurement of J-coupling parameters [20].

2.6.2 Shimming

While passive shielding achieves a significant field reduction, a tiny residual magnetic field (a few nT) persists due to imperfect shield performance and permanent magnetization effects. Active compensation, or shimming, addresses this residual field as follows [13, 26, 42].

Inside the passive shields, sets of shim coils are strategically mounted (as three orthogonal Helmholtz coils). These coils are powered by low-noise current sources to generate small compensating magnetic fields that nullify the residual field. Shimming is an alternative process. It involves adjusting the currents in the shim coils while monitoring the NMR spectrum itself to minimize the Zeeman splitting. For example, minimizing the field using a sample like ^{13}C-formic acid allows for fine-tuning the field to near-zero levels, sub-nanotesla. The minimum achievable residual field across the sample is fundamentally constrained by the inherent spectral linewidth of the sample under investigation, as well as the precision and stability of the shim coils themselves. These internal coils are also essential for applying the specific magnetic field pulses (DC current pulses) necessary for spin encoding in ZULF NMR, as well as for intentionally applying small, orthogonal ultralow bias fields (ULF regime) when spectroscopic analyses benefit from slight Zeeman perturbations.

2.6.3 Degaussing

Mu-metal can acquire stray magnetization if exposed to a strong magnetic field (high-current DC pulses used for spin manipulation). This acquired magnetization degrades the overall shielding performance. Degaussing is required to restore the shield's high permeability. The method for demagnetizing mu-metal shields employs an alternating current (AC) field that is slowly ramped up and then down to zero.

A thick, insulated wire (rated for at least 10 A, American gauge 20 or thicker) is looped through the shield, which consists of 20 to 30 turns. The wire is connected in series with two variacs and the main power supply. The current is gradually increased to a high level (10 A) and then slowly returned to zero, with a single up-down cycle lasting 5 to 10 minutes. Crucially, the magnetic fields must be reduced very slowly at low current levels to ensure proper adiabatic demagnetization [19].

The need for strict magnetic hygiene extends to the ZULF detector itself, particularly when integrating novel sensors [23, 42]:

- **Magnetometer Magnetization:** Magnetometers based on magnetoresistive (MR) sensors (a different technology from OPMs or SQUIDs but also used in ZULF research) contain ferromagnetic materials, leading to back-action magnetic fields that interfere with the nuclear spin sample. Protocols such as **coercivity** sweeps and controlled degaussing sweeps have been explored to attempt to reduce the remanent magnetization of these sensors; however, achieving statistically significant improvements in the detected NMR signal has proven challenging.
- **NV Centers:** Similarly, incorporating Nitrogen-Vacancy (NV) centers in nanodiamonds for ZULF detection is a promising direction, but guaranteeing that all nearby components, including optical elements, are non-magnetic presents a significant challenge in implementing ZULF NMR protocols.

- **Operational Robustness:** In contrast, recent multichannel ZULF systems that minimize the use of magnetic pulsing coils and rely on robust prepolarization fields have demonstrated exceptional stability, maintaining highly stable, T_2^*-limited linewidths for over 10 days *without* requiring shimming or degaussing. This robustness highlights the importance of minimizing sources of magnetic disturbance for long-term ZULF operation.

2.7 Spin Polarization Methods

The pursuit of ZULF NMR necessitates overcoming a critical challenge rooted in fundamental spin physics: the vanishingly small equilibrium nuclear spin polarization in the absence of a strong magnetic field [22]. Therefore, both prepolarization and hyperpolarization techniques are essential prerequisites for obtaining a detectable signal in the ZULF regime, where spin dynamics are dominated by the internal interactions; see eq (2.10). Since the signal-to-noise ratio (SNR) in conventional NMR is inherently coupled to the square of the magnetic field strength B_0^2, polarization enhancement is crucial for practical ZULF applications [4].

2.7.1 Thermal Prepolarization Using Halbach Magnets

Prepolarization (brute-force polarization) is the simplest method to induce initial magnetization. This technique relies on placing the sample in a strong magnetic field, B_{pol}, generated by an array of permanent magnets, to reach thermal (Boltzmann) equilibrium before shuttling it rapidly to the low-field detector [23, 10].

For ZULF systems, high-field magnets are positioned *exsitu* to avoid interference with the sensitive magnetometers. These arrays are frequently implemented using **Halbach magnets**, which are periodic arrangements of permanent magnetic blocks optimized to generate a strong, highly confined field internally while minimizing the external fringe fields.

Samples are polarized in Halbach arrays, delivering fields around $B_{pol} = 2$ T [19]. At room temperature (300 K), a 2 T field yields an equilibrium polarization of approximately 7 to 14 ppm for protons. While low, this polarization level is consistent and sufficient for basic ZULF experiments when coupled with highly sensitive detectors [43].

After polarization, the sample must be mechanically transported (shuttled) quickly (≤ 1 s) into the magnetically shielded detection zone. To maintain spin order during transport through the fringe fields, a solenoidal **guiding field** (GF1) is applied along the path. This field facilitates an *adiabatic transfer* where the spins remain aligned with the total magnetic field direction, thus preserving polarization as the field magnitude reduces to the ultralow field of the detection environment [44]. A rapid, non-adiabatic switch upon arrival in the ZULF region transforms the preserved Zeeman populations into a coherent superposition of ZULF eigenstates, generating the transient signal for detection [42].

2.7.2 Hyperpolarization: PHIP, SABRE, and DNP

Hyperpolarization techniques generate spin polarization orders of magnitude greater than thermal equilibrium, dramatically boosting the SNR in ZULF NMR [22].

Parahydrogen-Induced Polarization (PHIP): This technique exploits the nuclear singlet state purity of parahydrogen (pH_2), generating polarization up to unity. Hydrogenative PHIP involves a chemical reaction: the addition of pH_2 across double or triple bonds in the target molecule. This method successfully enabled the direct detection of $J-$spectra in a single transient [13].

Signal Amplification by Reversible Exchange (SABRE): A non-hydrogenative approach where pH_2 and the substrate temporarily bind to an

iridium-based metal complex, allowing polarization transfer via $J-$coupling networks during the complex lifetime. SABRE is highly efficient in the ZULF regime, particularly between 1 and 10 μT due to the polarization transfer being optimally mediated by **level anticrossings (LACs)** of the nuclear spin energy states, which occur when the Larmor frequency difference between the pH_2-driven hydrides and the heteronucleus (^{13}C or ^{14}N matches the molecular $J-$couplings [17]. The microtesla variant, SABER in SHield Enables Alignment Transfer to Heteronuclei (SABRE-SHEATH), has been instrumental in ZULF development, achieving polarization levels of several percent in heteronuclei like ^{15}N and ^{13}C (up to 10% on ^{15}N and 11% on bound $^{13}C-$pyruvate) [45].

Dynamic Nuclear Polarization (DNP): This approach transfers the large polarization of unpaired electron spins (from free radicals) to nuclear spins using microwave irradiation.

- **Dissolution DNP (dDNP):** Considered the gold standard for metabolic substrates, dDNP involves polarizing a sample frozen in a glass matrix at high-field (3-7 T) and cryogenic temperatures (1-2 K), then rapidly dissolving it for liquid-state detection [15].
- **Overhauser DNP (ODNP):** This mechanism occurs in solution at room temperature, driven by dipolar relaxation upon saturation of electron transitions, and has been demonstrated for enhanced MRI at fields as low as 96 μT using SQUID sensors [13].

Stochastic/Statistical Polarization: This technique is preferred for single-spin ZULF NMR. It dictates that an ensemble of N randomly prepared spins will exhibit a measurable polarization excess proportional to $\sqrt{N}$ along any axis. This intrinsic phenomenon requires no active external manipulation and becomes highly efficient as the ensemble size N decreases, making it ideal for nanoscale detection regimes where traditional bulk methods fail [15, 14].

Chapter 3

Experimental Methods: Simulation, Signal Processing, and Fitting

3.1 Nuclear Spin Relaxation

In NMR, the transverse relaxation time constant T_2 quantifies the decay of coherent transverse magnetization due to local magnetic field fluctuations and spin-spin interactions. The Bloch equations phenomenologically describe this exponential decay, while the Redfield theory provides a microscopic explanation based on time-dependent perturbation of the spin Hamiltonian [2, 5].

For liquids, proton-proton dipolar interactions are the dominant mechanism for spin relaxation. The stochastic modulation of the dipolar coupling, due to molecular tumbling, produces fluctuations at frequencies around the Larmor frequency $\omega_0 = \gamma B_0$ [2].

3.1.1 Phenomenological Description: Bloch Equations and Relaxation Times T_1 and T_2

While the Hamiltonian dictates the coherent precession (Larmor frequency), the relaxation processes are inherently dissipative. The Bloch equations, introduced by Felix Bloch, provide a macroscopic description of the time evolution of the bulk magnetization vector $\mathbf{M} = (M_x, M_y, M_z)$ under the combined effects of the magnetic field and relaxation. The set of coupled differential equations for the components of the magnetization vector, expressed in the rotating frame, can be generalized as:

$$\frac{d\mathbf{M}}{dt} = \gamma(\mathbf{M} \times \mathbf{B}_0) - \begin{pmatrix} M_x/T_2 \\ M_y/T_2 \\ (M_z - M_0)/T_1 \end{pmatrix} \tag{3.1}$$

where T_1 and T_2 denote the longitudinal (spin-lattice) and transverse (spin-spin) relaxation time constants, respectively.

$\mathbf{T_1}$ governs the exponential recovery of the longitudinal magnetization (M_z) toward its thermal equilibrium value (M_0). The process requires the exchange of energy between the nuclear spin system and the "lattice" (the surrounding molecular environment, even in liquids). The relaxation rate is $1/T_1$.

$\mathbf{T_2}$ governs the exponential decay of the transverse magnetization components (M_x, M_y). This decay, characterized by the rate $1/T_2$, occurs due to internal magnetic field fluctuations, leading to the loss of phase coherence among the precessing spins. T_2 is fundamentally limited by T_1, such that $T_2 \leq T_1$.

For observable NMR line widths, the transverse decay is dominated by field inhomogeneity, leading to the effective transverse relaxation time T_2^*. The intrinsic line width ($\Delta\nu$) is inversely proportional to T_2^*:

$$\Delta\nu \propto \frac{1}{\pi T_2^*}$$

The relationship between T_2 (homogeneous decay) and T_2^* (inhomogeneous decay) is given by the approximation:

$$\frac{1}{T_2^*} \approx \frac{1}{T_2} + \frac{1}{T_2(\Delta B_0)}$$

where $T_2(\Delta B_0)$ accounts for field inhomogeneity.

3.2 Signal Formation

NMR spectroscopy, whether pursued in conventional high-field or utilizing the unique spin physics of the ZULF regime, relies fundamentally on rigorous quantum mechanical simulation frameworks to predict, analyze, and interpret experimental results. This approach moves beyond the simple vector model, which fails for coupled spin systems, utilizing the density operator formalism and the Liouville space picture.

3.2.1 Product Operator Formalism in NMR

In a coupled system, spin 1 does not have a single frequency ω_1. Instead, it splits into a doublet:

- One line at $\omega_1 + \pi J$ (when spin 2 is in the $|\beta\rangle$ state)
- One line at $\omega_1 - \pi J$ (when spin 2 is in the $|\alpha\rangle$ state)

The product operator formalism gives us mathematical tools to track these correlations. In the product operator formalism, the state of a single spin-1/2 system is described by the density operator, $\hat{\rho}(t)$, expressed as a linear combination of angular momentum operators. This approach provides a rigorous quantum mechanical description of NMR experiments, bridging the gap between the semi-classical vector model and density matrix theory [9].

The Density Operator for Spin-1/2 The state of a nuclear spin ensemble in an NMR experiment is rigorously described by the spin density operator, $\hat{\rho}$. This operator is mathematically defined as an ensemble average over the individual system wavefunctions ($|\psi\rangle$) [15]:

$$\hat{\rho} = \overline{|\psi\rangle \langle\psi|} \tag{3.2}$$

The density operator $\hat{\rho}$ is a bounded, positive, and Hermitian matrix with unit trace ($\mathrm{Tr}[\hat{\rho}] = 1$). Matrix elements along the main diagonal encode **state populations** (occupation probabilities), whereas off-diagonal terms encode **quantum coherences** (phase relationships between states) [46].

For a single spin ($\hat{I}$), the density operator $\hat{\rho}(t)$ represents the state of the system at any time t. It is expanded in the basis of the Cartesian angular momentum operators I_x, I_y, and I_z [9]:

$$\hat{\rho}(t) = a(t)I_x + b(t)I_y + c(t)I_z \tag{3.3}$$

Here, the coefficients $a(t)$, $b(t)$, and $c(t)$ correspond directly to the observable macroscopic magnetization components M_x, M_y, and M_z [9].

- I_z**:** Represents longitudinal magnetization aligned with the static magnetic field B_0. At thermal equilibrium, the density operator is proportional to this operator: $\hat{\rho}_{\mathrm{eq}} \propto I_z$ [9].
- I_x **and** I_y**:** Represent transverse magnetization components in the rotating frame. These correspond to coherences that are detected as the NMR signal.

Initial State Determination ($\hat{\rho}(0)$) The simulation begins by defining the initial density matrix $\hat{\rho}(0)$, which represents the thermal equilibrium state reached during prepolarization in a high magnetic field [8, 18]. For thermal equilibrium in a canonical ensemble, the density operator is [47]:

$$\hat{\rho}_{\mathrm{eq}} = \frac{\exp\left(-\hat{H}/k_B T\right)}{\mathrm{Tr}[\exp\left(-\hat{H}/k_B T\right)]} \tag{3.4}$$

Due to the small difference in energy levels compared to thermal energy ($k_B T$), the high-temperature approximation $\exp\left(\hat{H}\right) \approx \hat{E} + \hat{H}$ is used. For an n-spin system polarized along the z-axis, the equilibrium density operator, neglecting spin-spin interactions during polarization, simplifies to a linear combination of longitudinal operators [47]:

$$\hat{\rho}_{\text{eq}} \propto \hat{E} + \sum_{\ell=1}^{n} P_\ell \hat{I}_{\ell z} \approx \hat{E} + \frac{1}{2^{n-1}} \sum_{\ell=1}^{n} P_\ell \hat{I}_{\ell z} \tag{3.5}$$

where P_ℓ is the polarization for spin ℓ.

Simplified Density Matrix For computational and analytical convenience, the identity matrix ($\hat{E}$ or $\hat{1}$) is removed from the density operator, as it commutes with all operators and does not affect the signal outcome:

$$\hat{\rho}(0) \to \hat{\rho}_{\text{eq}} - \frac{\hat{1}}{2^n} \tag{3.6}$$

In simulations, this simplified density matrix is then used as the starting point for propagation, including only the longitudinal magnetization, $\sum_l P_l \hat{I}_{lz}$ [18].

Time Evolution and Hamiltonians The evolution of the density operator is governed by the Liouville-von Neumann (LvN) equation:

$$\frac{d\hat{\rho}(t)}{dt} = -i[\hat{H}(t), \hat{\rho}(t)] \tag{3.7}$$

In conventional NMR simulation, it is customary to use angular frequency units for the Hamiltonian, meaning $\hat{H}$ represents $\hat{H}_{\text{full}}/\hbar$ [47]. This equation describes the time evolution as a unitary transformation, which is conceptually equivalent to a rotation of the operators in the vector space defined by I_x, I_y, I_z.

If the Hamiltonian is time-independent over an interval t (during free evolution periods), the solution to the LvN equation is given by the unitary transformation [15]:

$$\hat{\rho}(t) = \exp\left(-i\hat{H}t\right)\hat{\rho}(0)\exp\left(i\hat{H}t\right) = \hat{U}(t)\hat{\rho}(0)\hat{U}^\dagger(t) \tag{3.8}$$

where $\hat{U}(t) = \exp\Big(-i\hat{H}t\Big)$ is the unitary propagator operator. The calculation of the matrix exponential is central to spin dynamics simulation [18].

When the Hamiltonian is piecewise constant (a pulse sequence applied over multiple discrete steps), the final state $|\psi(t_n)\rangle$ is obtained by successive application of propagators [47]:

$$|\psi(t_n)\rangle = \hat{U}(t_n, t_{n-1}) \cdots \hat{U}(t_2, t_1)\hat{U}(t_1, t_0) \, |\psi(t_0)\rangle \tag{3.9}$$

For continuously varying Hamiltonians (during adiabatic field ramping in ZULF experiments), the total evolution must be discretized into short time intervals δt [18, 47]:

$$\hat{\rho}(t_{k+1}) = \hat{U}(t_k \to t_{k+1})\hat{\rho}(t_k)\hat{U}^{\dagger}(t_k \to t_{k+1}) \tag{3.10}$$

where $\hat{U}(t_k \to t_{k+1}) = \exp\Big(-i\hat{H}(t_k)\delta t\Big)$.

Relevant Hamiltonians The effective nuclear spin Hamiltonian, $\hat{H}_{\text{spin}}$, governs the dynamics of the nuclear spins. For isotropic liquids, it is decomposed into Zeeman interaction ($\hat{H}_Z$), and the indirect $J-$coupling ($\hat{H}_J$), as shown in equation (2.6), for the HF in equation (2.7), and for the ZULF in equation (2.10) [9, 19].

1. **Free Precession:** During a delay, the spin evolves under the chemical shift offset Ω. The Hamiltonian is $H_{\text{free}} = \Omega I_z$.
2. **RF Pulses:** During a "hard" radiofrequency pulse, the Hamiltonian depends on the phase of the pulse. For an x-phase pulse we have, $H_{\text{pulse},x} = \omega_1 I_x$ while for a y-phase pulse $H_{\text{pulse},y} = \omega_1 I_y$. Here, ω_1 represents the field strength of the RF pulse.

Rules for Rotation The evolution of the operators can be calculated using cyclic commutation relations, visualized using rotation diagrams [9]. The general transformation for an operator I_{old} evolving under a Hamiltonian θI_a is:

$$\exp(-i\theta I_a)\{I_{\text{old}}\}\exp(i\theta I_a) = I_{\text{old}}\cos\theta + I_{\text{new}}\sin\theta \tag{3.11}$$

where I_{new} is the operator that follows I_{old} in a cyclic permutation ($x \to y \to x$) relative to the axis of rotation I_a, see Figure. 3.1 below.

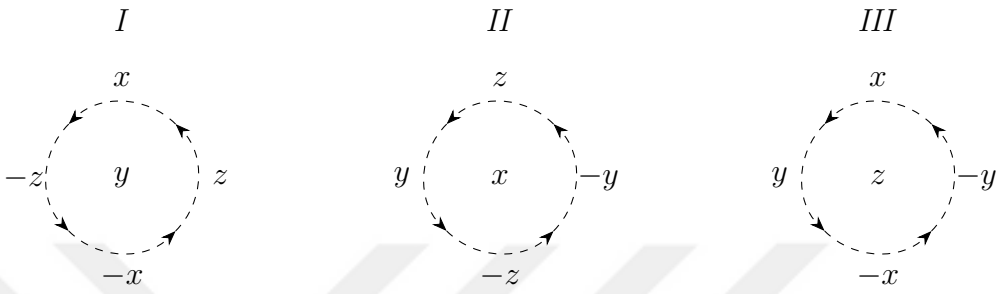


Figure 3.1: Cyclic rotation diagrams for product operator evolution. *I*: Rotation about y-axis (RF pulse with y-phase). *II*: Rotation about x-axis (RF pulse with x-phase). *III*: Rotation about z-axis (chemical shift evolution)

Rotation about z (Precession):

$$I_x \xrightarrow{\Omega t I_z} I_x \cos(\Omega t) + I_y \sin(\Omega t) \tag{3.12}$$

$$I_y \xrightarrow{\Omega t I_z} I_y \cos(\Omega t) - I_x \sin(\Omega t) \tag{3.13}$$

This mathematically describes the vector model concept of precession in the transverse plane shown in Figure. 3.2.

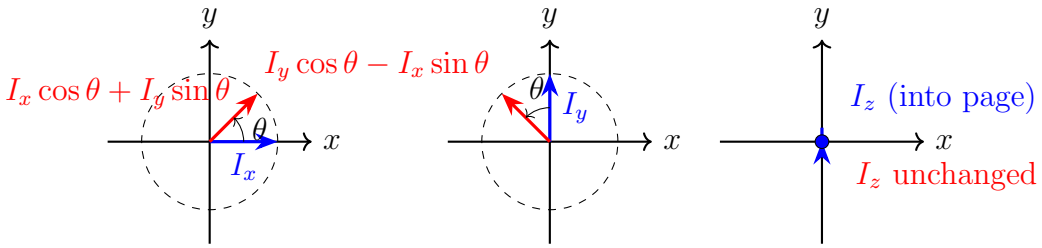
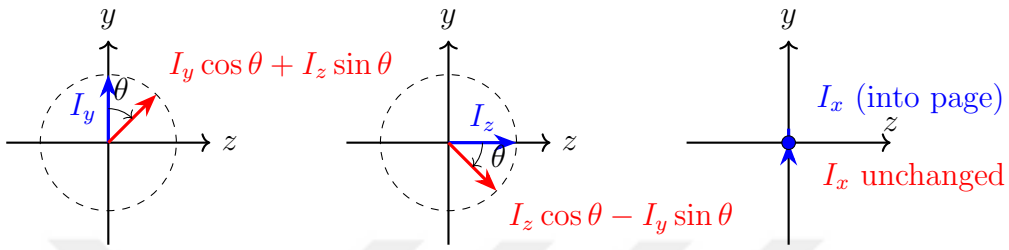


Figure 3.2: Rotations about the z-axis (precession under chemical shift)

Rotation about x (RF Pulse): For a pulse of flip angle $\beta = \omega_1 t_p$:

$$I_z \xrightarrow{\omega_1 t_p I_x} I_z \cos(\beta) - I_y \sin(\beta) \tag{3.14}$$

This confirms that an x-pulse rotates equilibrium magnetization (I_z) toward the $-y$ axis, Figure. 3.3.



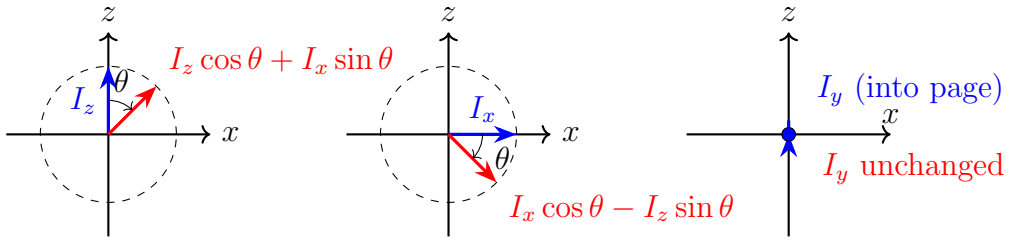
Rotation about x: $I_y \rightarrow I_z$ | Rotation about x: $I_z \rightarrow -I_y$ | Rotation about x: $I_x \rightarrow I_x$

Figure 3.3: Rotations about the x-axis (RF pulse with x-phase)

Rotation about y (RF Pulse):

$$I_z \xrightarrow{\omega_1 t_p I_y} I_z \cos(\beta) + I_x \sin(\beta) \tag{3.15}$$

A y-pulse rotates z-magnetization toward the $+x$ axis, Figure. 3.4.



Rotation about y: $I_z \rightarrow I_x$ | Rotation about y: $I_x \rightarrow -I_z$ | Rotation about y: $I_y \rightarrow I_y$

Figure 3.4: Rotations about the y-axis (RF pulse with y-phase)

Extension to Two Coupled Spin-1/2 Nuclei For a system of two coupled spin-1/2 nuclei (labeled 1 and 2), the density operator is expanded using a basis set of 16 operators. These operators classify the state of the system into observable magnetization, anti-phase magnetization, and unobservable multiple-quantum coherences [9].

While a single spin requires only three operators (I_x, I_y, I_z), a two-spin system requires operators for each spin individually, as well as products of operators involving both spins [8]. Operators such as I_{1x} and I_{2x} represent **in-phase magnetization**. Physically, I_{1x} corresponds to x-magnetization on spin 1. In a coupled spectrum, this manifests as a doublet where both lines have the same phase (both positive absorption lines). Similarly, I_{1y} and I_{2y} represent in-phase magnetization aligned along the y-axis, typically associated with a dispersion mode lineshape [8].

A critical feature of the two-spin formalism is the introduction of product terms such as $2I_{1x}I_{2z}$. This operator represents x-magnetization of spin 1 that is **anti-phase** with respect to the coupling to spin 2. In the spectrum, this appears as a doublet where the two lines have opposite signs (one positive, one negative). The factor of 2 is required for normalization purposes within the formalism. Anti-phase terms are sensitive to the spin state of the coupling partner. For example, the two lines of the spin 1 doublet correspond to spin 2 being in the α or β state; the anti-phase nature indicates these lines have different signs [9].

The remaining operators represent states that are not directly observable in an NMR spectrum but are essential for coherence transfer pathways. The longitudinal Two-Spin Order ($2I_{1z}I_{2z}$) represents a specific non-equilibrium population distribution involving correlations between the z-components of both spins. Product operators containing two transverse components, such as $2I_{1x}I_{2x}$, $2I_{1x}I_{2y}$, $2I_{1y}I_{2x}$, and $2I_{1y}I_{2y}$, correspond to multiple-quantum coherences (double-quantum and zero-quantum) [9].

The evolution of these operators is dictated by the active Hamiltonian. A key principle is that operators belonging to different spins commute; therefore, rotations applied to spin 1 do not affect operators strictly belonging to spin 2 [8]. Evolution under chemical shift offsets or RF pulses is treated as a sequence of rotations applied to each spin individually. For a term like $2I_{1x}I_{2z}$ evolving under the offsets of both spins (Ω_1 and Ω_2): I_{1x} rotates about the z-axis to generate $I_{1x}\cos(\Omega_1 t)+I_{1y}\sin(\Omega_1 t)$, and I_{2z} commutes with the z-rotation operator (I_{2z}) and remains unchanged. Resulting $2I_{1x}I_{2z} \xrightarrow{\Omega t} 2I_{1x}I_{2z}\cos(\Omega_1 t) + 2I_{1y}I_{2z}\sin(\Omega_1 t)$ [9].

In pulse evolution (coherence transfer), RF pulses can transfer magnetization between spins. For example, applying a $(\pi/2)_y$ pulse to the anti-phase term $2I_{1x}I_{2z}$ [9]:

$$2I_{1x}I_{2z} \xrightarrow{90^\circ(I_{1y}+I_{2y})} 2(-I_{1z})I_{2x} = -2I_{1z}I_{2x} \tag{3.16}$$

I_{1x} is rotated by 90° about y to become $-I_{1z}$. I_{2z} is rotated by 90° about y to become I_{2x}. Anti-phase magnetization on spin 1 is transferred to anti-phase magnetization on spin 2. This process is fundamental to experiments explained laterly like COSY.

Evolution under the scalar coupling Hamiltonian drives the interconversion between in-phase and anti-phase magnetization [9].

In-phase to anti-phase conversion:

$$I_{1x} \xrightarrow{2\pi J_{12}I_{1z}I_{2z}t} I_{1x}\cos(\pi J_{12}t) + 2I_{1y}I_{2z}\sin(\pi J_{12}t) \tag{3.17}$$

This transformation shows that in-phase magnetization evolves into anti-phase magnetization (and rotates from x to y) at a rate determined by the coupling constant J_{12}.

Conversely, anti-phase magnetization evolves back into in-phase magnetization:

$$2I_{1x}I_{2z} \xrightarrow{2\pi J_{12}I_{1z}I_{2z}t} 2I_{1x}I_{2z}\cos(\pi J_{12}t) + I_{1y}\sin(\pi J_{12}t) \tag{3.18}$$

At $t_1 = 0$, there is a pure in-phase magnetization ($\hat{I}_{1x}$). The doublet has two peaks with the same phase. As time progresses, the two lines of the doublet start to **dephase** relative to each other because they are precessing at slightly different frequencies (separated by J_{12}).

At a delay of $t = 1/(2J_{12})$, the argument of the sine and cosine is $\pi/2$. The cosine term vanishes, and the sine term becomes 1. This results in complete conversion from in-phase to anti-phase (or vice versa).

At a delay of $t = 1/J_{12}$, the term changes sign ($I_{1x} \to -I_{1x}$) [9].

3.2.2 Time-Domain and Frequency-Domain

The analysis of an NMR experiment relies on the interconversion between the time-domain signal, known as the Free Induction Decay (FID), and the frequency-domain spectrum, which is accomplished via Fourier transform (FT). The simulated time-domain signal, $S(t)$, is obtained by calculating the expectation value of the magnetization operator ($\hat{M}$) at each time point, t. The expectation value of any observable $\hat{A}$ is determined by the trace of the product of the observable operator and the density operator [3]:

$$\langle \hat{A} \rangle(t) = \mathrm{Tr}\{\hat{A}\hat{\rho}(t)\} \tag{3.19}$$

Magnetization operator The magnetization operator $\hat{\mathbf{M}}$ is proportional to the sum of the spin operator ($\hat{\mathbf{I}}$) weighted by the their gyromagnetic ratios (γ_i): This mathematical relationship dictates how experimental parameters set during acquisition directly influence the observable spectral characteristics, such as resolution and linewidth [15, 18].

$$\hat{\mathbf{M}} \propto \sum_{i=1}^{N} \gamma_i \hat{\mathbf{I}}_i \tag{3.20}$$

3.2.2.1 Time Domain Signal: The Free Induction Decay (FID)

The FID, $s(t)$, represents the emission of RF energy by the excited nuclear spin system as its net transverse magnetization precesses and decays.

High-Field NMR Detection and Modeling In high-field NMR, the signal is detected inductively by a coil oriented transversely to the main static field B_0.

An RF pulse, a $\frac{\pi}{2}$ pulse, tips the equilibrium longitudinal magnetization (M_0) into the transverse (x', y') plane of the rotating frame (Fig 3.5). The magnetization then freely precesses at the offset frequency Ω (the difference between the

Larmor frequency ω_0 and the RF carrier-frequency ω_{ref}) [11].

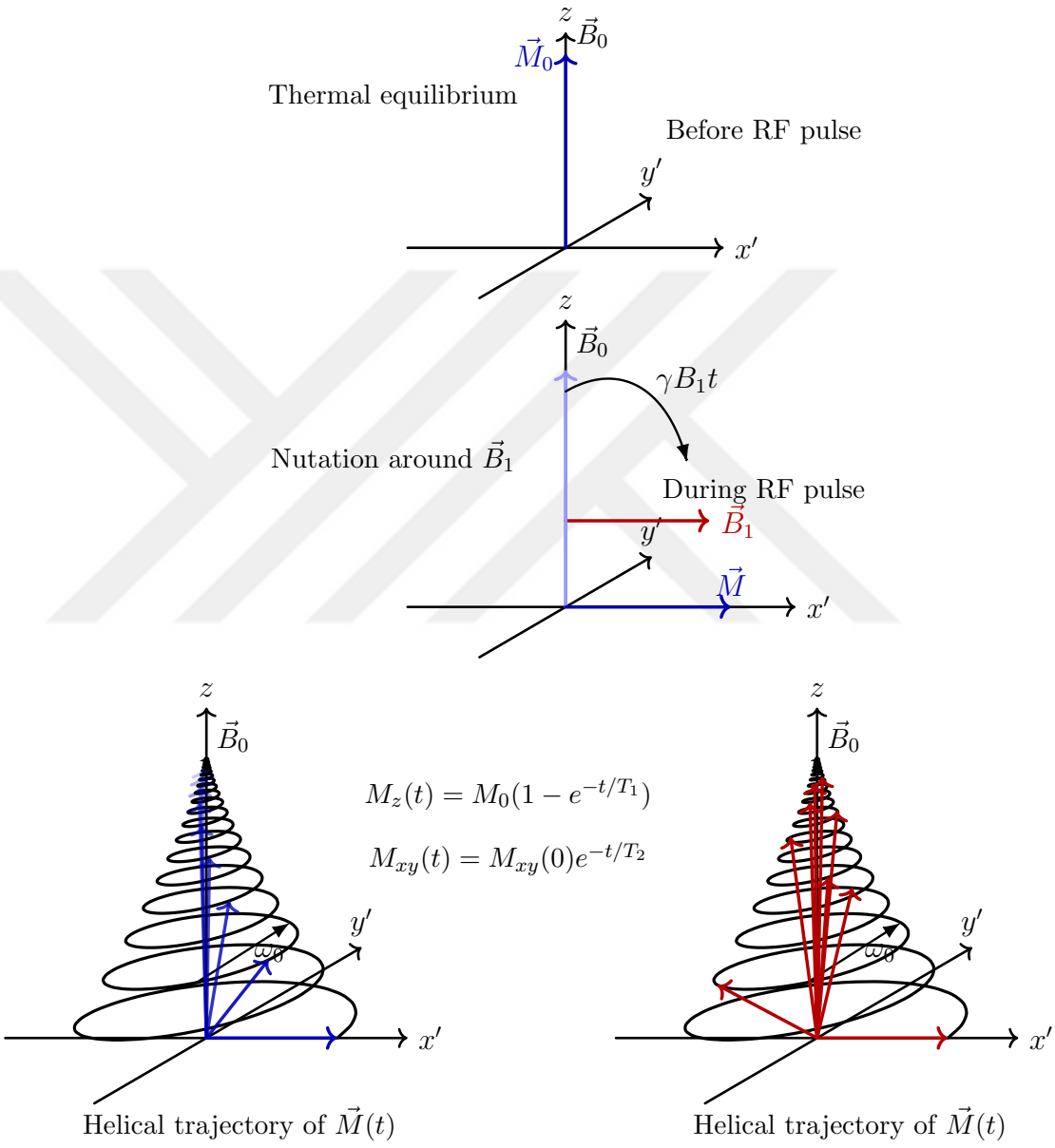


Figure 3.5: Nutation of the net magnetization vector $\mathbf{M}$ under the influence of an RF pulse $\mathbf{B}_1$ applied perpendicular to the static field $\mathbf{B}_0$. (Above) At thermal equilibrium, $\vec{M}$ aligns with $\mathbf{B}_0$ along the z-axis. (Middle) During the RF pulse, $\vec{M}$ precesses about $\mathbf{B}_1$, rotating by an angle $\gamma B_1 t$ into the transverse plane. (Bottom right) After the pulse, $\mathbf{M}(t)$ undergoes transverse relaxation (T_2 decay); (Bottom left) longitudinal recovery (T_1), spiraling back towards equilibrium along z.

The magnetization components, $M_x(t)$ and $M_y(t)$, are detected in quadrature and combined into a complex time-domain signal $s(t)$ [47]:

$$s(t) = S_x(t) + iS_y(t) \propto M_x(t) + iM_y(t) \propto \langle \hat{I}_x(t) \rangle + i\langle \hat{I}_y(t) \rangle \tag{3.21}$$

If the magnetization starts along $-y$ after a $(\frac{\pi}{2})_x$ pulse in the rotating frame, the components are defined by:

$$M_x(t) = M_0 \cos(\Omega t) \quad \text{and} \quad M_y(t) = M_0 \sin(\Omega t) \tag{3.22}$$

The signal strength decays exponentially over time due to relaxation and field inhomogeneities (Fig 3.6). In the rotating frame, the complex signal $s(t)$ is modeled as an exponentially damped sinusoid [9, 47]:

$$s(t) = S_0 \exp(i\Omega t) \exp(-t/T_2) \tag{3.23}$$

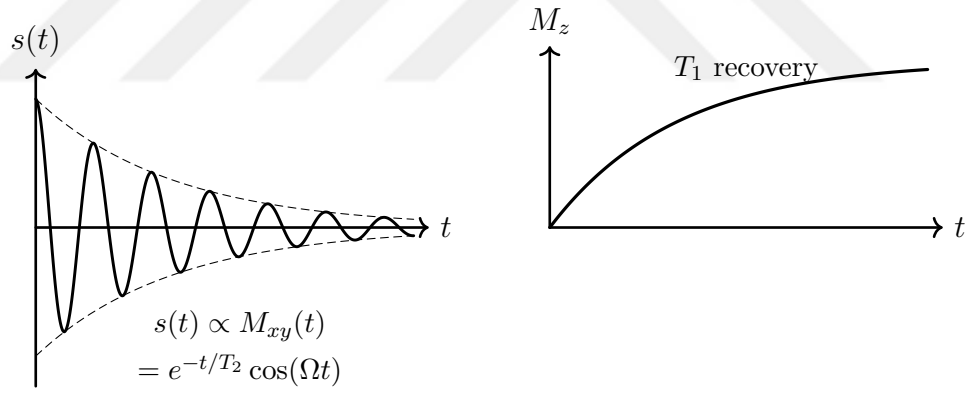


Figure 3.6: Nuclear magnetic relaxation. Left: Free induction decay (FID) showing transverse magnetization $M_{xy}(t)$ decaying as $\exp(-t/T_2)\cos(\omega_0 t)$ due to spin-spin relaxation with time constant T_2. The envelope decay rate determines the spectral linewidth. Right: Longitudinal relaxation showing recovery of z-magnetization $M_z(t)$ toward thermal equilibrium following a 90° pulse, characterized by the spin-lattice relaxation time T_1. The recovery reaches 63% of equilibrium magnetization at $t = T_1$.

If the magnetic field inhomogeneities are present, the decay is actually characterized by T_2^* [2]:

$$\frac{1}{T_2^*} = \frac{1}{T_2} + \frac{1}{T_2'} \tag{3.24}$$

which is faster than the true homogeneous T_2 decay rate (Fig. 3.6).

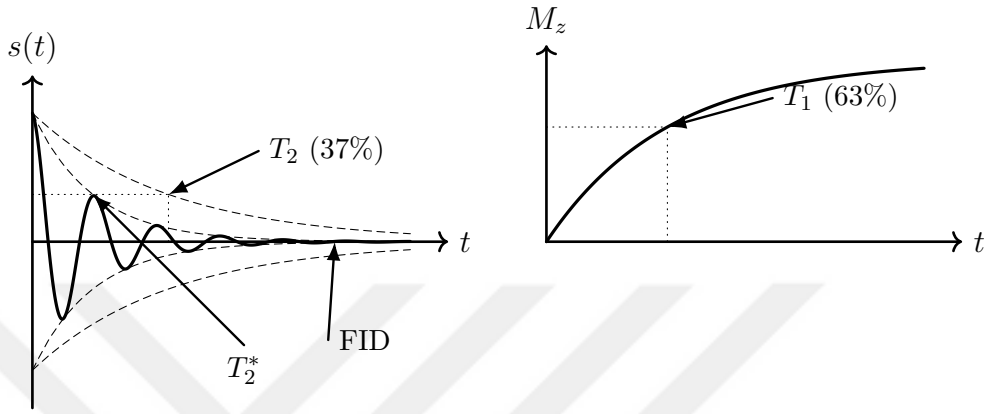


Figure 3.7: Distinction between T_2 and T_2^* relaxation. Left: The observed free induction decay exhibits rapid signal loss characterized by T_2^*, which includes both intrinsic molecular relaxation (T_2) and dephasing from magnetic field inhomogeneity. The true molecular transverse relaxation time T_2 (shown by dashed envelope) is longer than the observed T_2^*. The relationship $\frac{1}{T_2^*} = \frac{1}{T_2} + \frac{1}{T_2^{\text{inhom}}}$ separates intrinsic from field-dependent contributions. Right: Longitudinal relaxation T_1 recovery is unaffected by field inhomogeneity and reaches 63% at the characteristic time T_1.

ZULF NMR Detection In the ZULF regime, inductive detection is abandoned due to its low sensitivity at low frequencies, favoring non-inductive methods like those explained previously, OPMs or SQUIDs [17, 10, 26].

- **Observable Quantity:** ZULF magnetometers detect the total magnetic field produced by the nuclear spins, along the $z-$axis (sensitive axis), in the low-frequency range of 0 Hz to a few thousand Hz [18, 13, 19]:

$$\text{signal}(t) \propto \langle M_z \rangle(t) \equiv \sum_j \frac{h\gamma_j}{2\pi} \langle \hat{I}_z^{(j)} \rangle \tag{3.25}$$

- **Signal Characteristics:** Since the detector measures a real magnetic field component (rather than transverse precession), the resulting FID is real. In ZULF, the time-domain signal may feature an exponentially decaying

envelope with a periodic element or, in some cases, a periodic signal with exponential decay, characteristic of HF FIDs. Because the measured signal is real, the resulting spectrum is symmetric around 0 Hz [17, 18].

3.2.2.2 Frequency Domain: Fourier Transformation

The simulated time-domain signal $S(t)$ (the FID) is Fourier transformed to obtain the frequency spectrum $S(\omega)$ (Fig. 3.8).

$$S(\omega) = \mathcal{F}\{S(t)\} = \int_{-\infty}^{\infty} s(t)e^{-i\omega t}dt \tag{3.26}$$

with a magnitude:

$$|S(\omega)| = \sqrt{\mathrm{Re}[S(\omega)]^2 + \mathrm{Im}[S(\omega)]^2} \tag{3.27}$$

Analytically, the signal $\langle M_p \rangle(t)$ can be expressed as a sum over the pairs of eigenstates ($\{|\psi_u\rangle, |\psi_v\rangle\}$) of the Hamiltonian $\hat{H}$ [6, 5]:

$$S_p(t) \propto \sum_{u,v} \langle u| \hat{M}_p |v\rangle \rho_{uv}(0) \exp(-i\omega_{uv}t) \tag{3.28}$$

where $\omega_{uv} \equiv (\langle u| \hat{H} |u\rangle - \langle v| \hat{H} |v\rangle)/\hbar$ are the transition frequencies. The frequency domain spectrum, thus, contains peaks at these eigenfrequencies ω_{uv}, provided the matrix element $\langle u| \hat{M}_p |v\rangle$ (the transition moment) and the initial coherence $\rho_{uv}(0)$ are non-zero.

Digital Acquisition and Parameters Since NMR signal is continuous (analog), it must be converted to a discrete sequence of points for computer processing via an Analog-to-Digital Converter (ADC). This digitalization imposes fundamental constraints on spectral quality. The key acquisition parameters, such as acquisition time (τ_{aq} or AT), spectral width (SW or fsw), and number of points (N or np), are interrelated [1]

$$\tau_{\mathrm{aq}} = \frac{N}{2 \cdot SW} \tag{3.29}$$

This means that changing one parameter affect the others.

The sampling interval (dwell time, τ_{dw} or τ_{sample}) is the separation between acquired points. The spectral width is the inverse of the dwell time, $SW = 1/\tau_{\mathrm{dw}}$. The Nyquist frequency, $f_{NY} = SW/2$, sets the maximum frequency that can be correctly sampled; if the signal contains frequencies higher than f_{NY}, folding (aliasing) occurs, leading to an erroneous signal in the spectrum [9, 18, 47].

The digital resolution ($\Delta\nu$) is determined by the inverse of the acquisition time [1]

$$\Delta\nu = \frac{1}{\tau_{\mathrm{aq}}} \tag{3.30}$$

FT and Lorentzian Lineshape The mathematical properties of the Fourier transform directly link the time-domain decay rate to the frequency-domain linewidth. The FT of the exponentially decaying time-domain signal (Eq. (3.21)) yields a complex Lorentzian lineshape in the frequency domain (Fig. 3.8). The real part is the **absorption mode** Lorentzian, $A(\omega)$, and the imaginary part is the dispersion mode Lorentzian, $D(\omega)$ [9]:

$$S(\omega) \propto \frac{R}{R^2 + (\omega - \Omega)^2} + i\frac{\Omega - \omega}{R^2 + (\omega - \Omega)^2} \tag{3.31}$$

where $R = 1/T_2$ is the decay rate constant.

The full width at half height (FWHH or ℓ_B) of the absorption peak in linearly (Fig. 3.8) related to the transverse relaxation rate constant R and inversely related to T_2 [47]:

$$\ell_B = \frac{R}{\pi}\ \mathrm{Hz} = \frac{1}{\pi T_2}\ \mathrm{Hz} \tag{3.32}$$

A faster decay in the FID results in a broader line in the spectrum, although the integrated signal intensity remains constant.

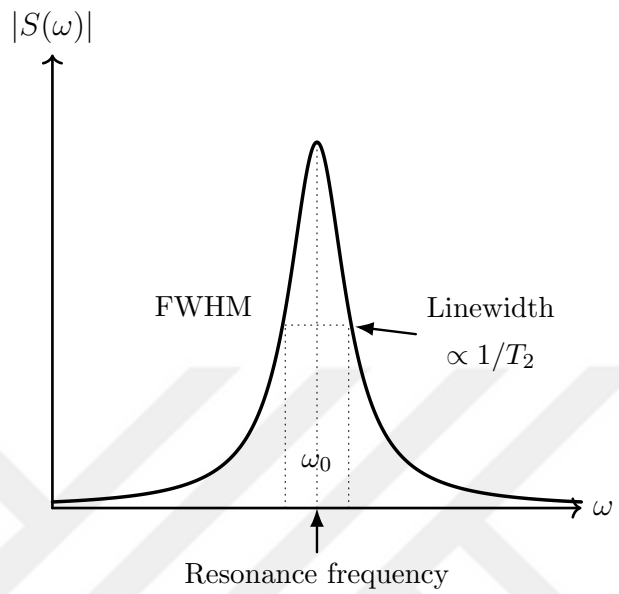


Figure 3.8: Frequency-domain representation of NMR signal. Fourier transform of the free induction decay produces a Lorentzian lineshape centered at the resonance frequency ω_0. The full width at half maximum (FWHM) is inversely proportional to the effective transverse relaxation time T_2. Longer coherence times produce narrower spectral lines, enhancing frequency resolution. The Lorentzian lineshape arises from the exponential decay envelope of the time-domain signal.

3.3 Processing and Analysis

To optimize the balance between SNR and resolution, the FID is manipulated mathematically prior to or following Fourier transformation.

3.3.1 Zero-Filling and Truncation Artifacts

These techniques relate to managing the discrete nature of the acquired data set. Zero-filling (ZF) involves adding data points with zero intensity to the end of the acquired FID prior to FT. Zero-filling increases the total number of points used for the FT, resulting in a higher density of data points in the frequency

spectrum, thereby improving *apparent* digital resolution (better definition of the peak shape) without increasing true resolution or adding noise. In practice, ZF to four times the original number of points is common [1, 47]. If the acquisition time (τ_{aq}) is too short and the receiver is switched off before the FID decays into the noise, the signal is truncated. This abrupt cutoff introduces oscillations around the base of the peak, known as sinc wiggles or truncation artifacts [1].

3.3.2 Phase Correction

In practice, the FID may start with an unknown phase shift (ϕ) due to instrumental delays or settings. If the FID is Fourier transformed without correction, the resulting spectrum will contain a mixture of absorption and dispersion lineshapes (a phase twist). Since the absorption mode provides better resolution, obtaining a pure absorption spectrum is highly desirable [47].

Phase correction involves rotating the complex spectrum $S(t)$ by multiplying it with a complex exponential factor, $\exp(i\phi_{\mathrm{corr}})$. The correction angle ϕ_{corr} is chosen to cancel out the actual phase shift ϕ such that $\phi_{\mathrm{corr}} = -\phi$ (zero-order phase correction). For a wide spectral range, the phase error may be frequency-dependent, $\phi(\Omega) \approx \phi^{(0)} + \phi^{(1)}\Omega$, requiring both zero-order ($\phi^{(0)}$) and first-order ($\phi^{(1)}$) corrections [9]. In ZULF, phase correction may be applied to the real frequency domain signal $I_r(\nu)$ via a complex constant $\exp(i\phi)$ before taking the real part [18]

$$I_r(\nu) = \mathrm{Re}\{I_c(\nu)\exp(i\phi)\} \tag{3.33}$$

3.3.3 Frequency Discrimination in HF and Multidimensional NMR

Frequency discrimination (the ability to distinguish between positive and negative offset frequencies ($\pm\Omega$)) is crucial for resolving complex spectra.

High-Field Quadrature Detection In HF NMR, the use of two phase-sensitive detectors (quadrature detection), whose phases are separated by $\frac{\pi}{2}$, measures both the M_x and M_y components. This yields a complex signal $s(t) = \exp(i\Omega t)$, which is sensitive to the sign of Ω, thus providing frequency discrimination and halving the required spectral width compared to single-channel detection [3, 9].

ZULF Lack of Discrimination In ZULF, since the FID signal is real (measuring longitudinal magnetization M_z), the spectrum is symmetric around zero frequency, and negative and positive frequencies are generally not distinguished. To account for this, the negative frequency domain signal is discarded, and the intensity of the positive frequency domain signal (abscissa) is doubled [18].

2D NMR Discrimination In 2D NMR, the signal modulation in the indirect time dimension (t_1) is usually amplitude modulated ($\propto cos(\Omega t_1)$). which inherently lacks frequency discrimination in the resulting F_1 dimension. To obtain the desired frequency-discriminated spectrum with a pure absorption lineshape, specialized methodologies are necessary [9]:

- **State-Haberkor-Ruben (SHR) Method** This method requires acquiring two separate data sets, a cosine-modulated signal (s_c) and a sine-modulated signal (s_s). These are combined after FT along the t_2 dimension into a new complex signal $S_{\text{States}}(t_1, \omega_2)$, which is then Fourier transformed along t_1 to yield a frequency-discriminated spectrum in pure absorption mode [9].
- **Time-Proportional Phase Incrementation (TPPI)** This method artificially shifts all frequencies in the F_1 dimension to be positive by incrementing the phase of a pulse (by a $\pi/2$) synchronously with the t_1 time incrementation. This eliminates the need for negative frequency, providing discrimination while maintaining absorption line shapes [9].

3.4 Open Quantum Systems: Microscopic Relaxation

For a complete description, the simulation must account for the interaction of the spin system (the "system") with its thermal environment (the "bath" or "lattice"), which causes dissipation and relaxation [48].

3.4.1 The Redfield Master Equation

The Redfield theory stands as a cornerstone of quantum magnetic resonance, providing the rigorous microscopic framework necessary to model and calculate nuclear spin relaxation processes. The fundamental purpose of Redfield theory is to derive the rate constants that govern the exponential decay of spin polarization (relaxation times T_1 and T_2) from the molecular motions and interactions within the sample [5]. The theory starts by treating the time-dependent interaction between the spin system and the bath ($\hat{H}_1(t)$) as a small perturbation, operating in the interaction representation. By applying a second-order approximation to the Dyson series solution of the LvN equation and invoking the Markov approximation (assuming the perturbation decays rapidly), the celebrated Redfield master equation is obtained [46].

The quantum state of the ensemble ($\hat{\rho}$) evolves under the combined influence of the spin Hamiltonian ($\hat{H}$) and the thermal environment (lattice) effects, formalized by the Redfield master equation [34, 49, 50]:

$$\frac{\partial \hat{\rho}(t)}{\partial t} = -i[\hat{H}, \hat{\rho}(t)] + R\hat{\rho}(t)$$

where R is the relaxation superoperator, which is the dissipative, non-Hermitian component responsible for relaxation. The master equation uses the commutation superoperator $L(\hat{\rho}) = -i[\hat{H}, \hat{\rho}]$, which represents coherent, unitary evolution [34, 50].

When this equation is written out explicitly in the eigenbasis of the static Hamiltonian ($\hat{H}_0$), it yields a system of linear differential equations for the density matrix elements ($\rho_{\alpha\alpha'}$), which explicitly defines the action of the relaxation superoperator [34]:

$$\frac{\partial \rho_{\alpha\alpha'}(t)}{\partial t} = \sum_{\beta\beta'} R_{\alpha\alpha',\beta\beta'} e^{i(\omega_\alpha - \omega_{\alpha'} + \omega_{\beta'} - \omega_\beta)t} \left(\rho_{\beta\beta'} - \rho^{\text{eq}}_{\beta\beta'}\right) \tag{3.34}$$

$R_{\alpha\alpha',\beta\beta'}$ is the matrix element of the relaxation superoperator, which is computed using perturbation theory based on correlation functions of the fluctuating interactions (dipole-dipole, chemical shift anisotropy). $\rho^{\text{eq}}_{\beta\beta'}$ is the thermal equilibrium density matrix element, which acts as the driving term towards equilibrium.

Alternatively, the **Lindblad** master equation provides the most general trace-preserving and completely positive form for Markovian evolution [49]:

$$\hat{\rho}(t) = -\frac{i}{\hbar}[\hat{H}(t), \hat{\rho}(t)] + \sum_n \frac{1}{2}\left[2\hat{C}_n\hat{\rho}(t)\hat{C}_n^\dagger - \hat{\rho}(t)\hat{C}_n^\dagger\hat{C}_n - \hat{C}_n^\dagger\hat{C}_n\hat{\rho}(t)\right] \tag{3.35}$$

Where $\hat{C}_n = \sqrt{2 \cdot R_2}(\hat{I}_x - i\hat{I}_y) = \sqrt{R_2}\hat{\sigma}_-$ are the collapse operators.

3.4.2 The Spectral Density Function

The spectral density function, denoted by $J(\omega)$, provides a fundamental bridge in NMR relaxation theory, connecting stochastic molecular dynamics ("lattice" motions) with observable spin relaxation phenomena through its quantitative relationship to macroscopic time constants (T_1 and T_2).

$J(\omega)$ represents the double-sided Fourier transform of the autocorrelation function $G(\tau)$ characterizing time-dependent fluctuations in the spin Hamiltonian [48]. These time-varying perturbations drive transitions and govern relaxation dynamics [8]:

$$J(\omega) = 2\int_0^\infty G(\tau)e^{-i\omega\tau}d\tau \tag{3.36}$$

where the correlation function $G(\tau)$ describes the statistical time dependence of the random field (or interaction) generated by molecular motion, $F(t)$. For a

stationary random function, $G(\tau)$ only depends on the time difference τ, not the absolute time t [8]. It is defined as the ensemble average of the product of the interaction at time t and its complex conjugate at a later time $t + \tau$ [9]:

$$G(\tau) = \langle F(t)F(t+\tau)^* \rangle \tag{3.37}$$

A frequently assumed form for the correlation function in liquids, which captures this behavior, is the exponential decay [5]:

$$G(\tau) = \langle B_x^2 \rangle e^{-|\tau|/\tau_c} \tag{3.38}$$

where $\langle B_x^2 \rangle$ is the mean square field component.

Eq (3.36) becomes:

$$J(\omega) = 2\int_0^\infty \langle B_x^2(t) \rangle e^{-|r|/r_c} e^{-i\omega\tau} d\tau. \tag{3.39}$$

$J(\omega)$ physically represents the **power spectrum** or **energy density** of the stochastic perturbation (molecular motion/noise) at a specific angular frequency ω [9, 48]. Spin relaxation (transitions between energy levels) is only effective when the frequency components of the random magnetic fields produced by molecular motion (ω) match the intrinsic transition frequencies of the spin system ($\omega_\alpha - \omega_\beta$). For a simple isolated spin relaxing due to a random field, the transition probabilities (W) are predicted to be proportional to the spectral density evaluated at the Larmor frequency, ω_0.

Dependence on Correlation Time τ_c If the correlation function is the simple exponential given above, the resulting spectral density function $J(\omega)$ takes the form of a Lorentzian distribution [9]:

$$J(\omega) = 2\langle B_x^2 \rangle \frac{\tau_c}{1 + \omega^2 \tau_c^2} \tag{3.40}$$

This function shows that the power spectrum of the random motion is nearly constant at very low frequencies but falls off rapidly when $2\pi\nu\tau_c \gg 1$ ($\omega\tau_c \gg 1$). The shape of $J(\omega)$ is highly dependent on the correlation time τ_c [5]:

- **Fast Motion Limit ($\omega\tau_c \ll 1$):** When molecular motion is rapid (short τ_c), the spectral density function is broad and relatively flat across a wide frequency range. This means the total energy of fluctuation is spread out, resulting in a small $J(\omega)$ at any particular high frequency, ω_0 [8]. In this limit, the area under the function remains constant [9].

- **Slow Motion Limit ($\omega\tau_c \gg 1$):** When molecular motion is slow (long τ_c), the spectral density function is narrowly peaked around $\omega = 0$. This results in very small $J(\omega)$ values at high Larmor frequencies, ω_0, leading to inefficient T_1 relaxation [9].

- **Optimal Relaxation (Maximum $J(\omega_0)$):** For a given Larmor frequency ω_0, the spectral density $J(\omega_0)$ reaches its maximum when the correlation time τ_c satisfies the condition $\omega_0\tau_c \approx 1$. This condition corresponds to the T_1 **minimum**, where longitudinal relaxation is most efficient. This dependence explains the existence of the characteristic T_1 minimum observed when $\omega_0\tau_c \approx 1$ [9].

The correlation time τ_c is given by the Stokes-Einstein-Debye relation [51]

$$\tau_c = \frac{4\pi\eta a^3}{3k_B T} \tag{3.41}$$

with:

- η = viscosity of a molecule in [Pa·s]
- a =hydrodynamic radius in [m]
- $k_B = 1.380649 \times 10^{-23}$ J/K (Boltzmann constant)
- $T = 298$ K (temperature)

Connection to Relaxation Rates The relaxation rate constants are directly proportional to the spectral density function evaluated at specific spin transition frequencies:

- **Longitudinal Relaxation (T_1):** involves energy exchange between the spin system and the lattice and is driven by field fluctuations matching the Larmor frequency ω_0 (single-quantum transitions). For a single spin, the relaxation rate T_1^{-1} depends on $J(\omega_0)$. For coupled spin systems (like the dipole-dipole interaction), it depends on spectral densities evaluated at ω_0 and $2\omega_0$ (double-quantum transitions) [8, 9].

$$\frac{1}{T_1} = \frac{3}{10} C \left[J(\omega_0) + 4J(2\omega_0) \right] \tag{3.42}$$

  where the dipolar coupling constant C is

$$C = \left(\frac{\mu_0}{4\pi} \right)^2 \hbar^2 \gamma^4 r^{-6}, \tag{3.43}$$

  with r being the internuclear distance between two protons.

- **Transverse Relaxation (T_2):** It is the loss of phase coherence and has contributions from field fluctuations matching ω_0 (lifetime broadening) and from static or near-zero frequency fluctuations $J(0)$ (secular broadening/adiabatic contribution). For dipole-dipole relaxation, T_2^{-1} explicitly includes $J(0)$, $J(\omega_0)$, and $J(2\omega_0)$. The $J(0)$ component accounts for magnetic field fluctuations that do not involve energy exchange but still cause spin dephasing (secular broadening) [9, 48].

$$\frac{1}{T_2} = \frac{3}{20} C \left[3J(0) + 5J(\omega_0) + 2J(2\omega_0) \right] \tag{3.44}$$

For isotropic rotational diffusion the spectral density functions with Lorentzian form are

$$J(0) = \tau_c \tag{3.45}$$

$$J(\omega_I) = \frac{\tau_c}{1 + \omega_I^2 \tau_c^2} \tag{3.46}$$

$$J(2\omega_I) = \frac{\tau_c}{1 + 4\omega_I^2 \tau_c^2} \tag{3.47}$$

Substituting $J(0)$, $J(\omega_I)$, $J(2\omega_I)$ into Eq. (3.44) gives the explicit B_0 dependence of T_2 [8]:

$$\frac{1}{T_2} = \frac{3}{20} C \left[3\tau_c + \frac{5\tau_c}{1 + \omega_0^2 \tau_c^2} + \frac{2\tau_c}{1 + 4\omega_0^2 \tau_c^2} \right]. \tag{3.48}$$

Obviously, at low fields ($\omega_0\tau_c \ll 1$), $1/T_2$ is large due to the dominance of $J(0)$, leading to severe line broadening. At high fields ($\omega_0\tau_c \gg 1$), the frequency-dependent terms vanish and T_2 increases

In the extreme narrowing limit (fast molecular motion), all spectral density functions $J(\omega)$ become equal, leading to $T_1 = T_2$.

The specific spectral densities required depend on the particular relaxation mechanism: for dipole-dipole relaxation, the relevant spectral densities involve $J(0)$, $J(\omega_0)$, and $J(2\omega_0)$. For the **Nuclear Overhauser Effect (NOE)**, the key parameters are spectral densities at the sum ($\omega_I + \omega_S$) and difference ($\omega_I - \omega_S$) frequencies of the two coupled spins [8].

Phenomenological Relaxation In many ZULF simulations, where high precision in coupling constants (J) is prioritized, relaxation is treated phenomenologically to reduce computational load. This involves multiplying the simulated time-domain signal $S(t)$ by an exponential decay envelope, $Ae^{-t/s}$, where s is an effective relaxation parameter [17, 20, 22].

3.4.3 Computational Challenges and Optimization

A major constraint in NMR simulation is the exponential scaling of computational complexity. For n spin-1/2 nuclei, the density matrix size N is 2^n, and the computational cost of matrix exponentiation (essential for propagation) is $O(N^3)$.

$$O(\text{Simulation Time}) \approx O((2^n)^3) = O(8^n)$$

To overcome this "exponential scaling wall," advanced simulation packages employ several strategies:

1. **Liouville Space Restriction/Basis Truncations:** simulations are performed in Liouville space, where the full matrix of size N^2 (or 4^n) is treated

as a vector. The basis set is restricted by dropping states that correspond to high-order correlations or are unreachable due to fast relaxation rates. This approach allows the simulation complexity to scale polynomially rather than exponentially with the number of spins n [48].

2. **Symmetry Factorization:** utilizing molecular symmetries or conservation laws can block-diagonalize the Hamiltonian, allowing independent subspaces to be simulated separately, significantly reducing matrix dimensions [20].

3. **Numerical Techniques:** Specialized numerical libraries such as MOIN, SpinDynamica, Spinach, and QuTip implement efficient techniques, including matrix multiplication optimization, Krylov subspace solvers for time evolution, and implicit linear solvers for steady-state problems [49].

3.5 2D NMR spectroscopy

3.5.1 High-Field COSY

COSY (COrrelation SpectroscopY) is a two-dimensional homonuclear NMR experiment that reveals scalar (J) couplings between nuclei by correlating frequencies along two spectral dimensions. Conceptually, COSY generalizes the idea of autocorrelation (self-correlation of a single signal) to cross-correlation between distinct spin coherences [9].

Given a complex time-domain signal $s(t)$, the autocorrelation function is [52]

$$R_{ss}(\tau) = \langle s(t)s^*(t+\tau)\rangle_t \tag{3.49}$$

where the angle brackets denote time (or ensemble) averaging. Wiener–Khinchin theorem relates the autocorrelation function to the power spectral density $S(\omega)$ via the Fourier transform [52, 53]:

$$S(\omega) = \mathcal{F}\{R_{ss}(\tau)\} = \int_{-\infty}^{\infty} R_{ss}(\tau)e^{-i\omega\tau}\,d\tau. \tag{3.50}$$

In NMR, the FID $s(t)$'s autocorrelation captures the frequency content (chemical shifts and line shapes) after the Fourier transform.

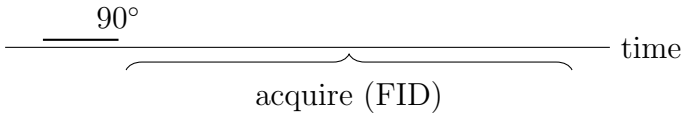
- Autocorrelation and relaxation Microscopic fluctuations of the local magnetic field $B(t)$ have an autocorrelation $R_B(\tau)$; their Fourier transform (spectral density $J(\omega)$) determines relaxation rates. For example, in simple models:

$$\frac{1}{T_1} \propto J(\omega_0), \quad \frac{1}{T_2} \propto J(0) + J(\omega_0). \tag{3.51}$$

  This ties dynamical correlations of molecular motion to observable NMR relaxation.

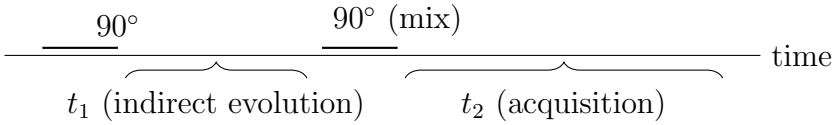
3.5.1.1 COSY pulse sequence

I. 1D pulse sequence A typical 1D acquisition is:



Single pulse, single evolution: no mixing, no t_1.

II. COSY pulse sequence (90°–t_1–90°–t_2): The basic homonuclear COSY sequence (non-selective) is:



t_1 is incremented across repeated experiments to build $S(t_1, t_2)$; a 2D Fourier transform (FT over t_1 and t_2) gives the COSY spectrum with [9]:

- **Diagonal peaks** tell where each spin resonates (like a normal 1D spectrum)
- **Cross peaks** appear at coordinates (Ω_1, Ω_2) and (Ω_2, Ω_1) if spins 1 and 2 are coupled

3.5.1.2 Product-operator derivation for COSY

Considering two coupled spin-1/2 nuclei $\hat{I}_1$ and $\hat{I}_2$ (an AX system) with chemical shifts ω_1, ω_2 (in angular frequency) and scalar coupling J_{12} [8, 9], The rotating-frame Hamiltonian (neglecting relaxation) is

$$\hat{H} = \omega_1 \hat{I}_{1z} + \omega_2 \hat{I}_{2z} + 2\pi J_{12} \hat{I}_{1z} \hat{I}_{2z}. \tag{3.52}$$

At thermal equilibrium the deviation density operator is

$$\rho_{eq} \propto \hat{I}_{1z} + \hat{I}_{2z}. \tag{3.53}$$

The product operator and rotations for COSY can be done similarly by following the calculations for two spins in section 3.2.1.

- **Step 1: Excitation**

  A non-selective $(\pi/2)I_x$-pulse is applied using product operators. It creates a transverse magnetization $(-\hat{I}_{1y} - \hat{I}_{2y})$

  $$\hat{I}_{1z} \xrightarrow{\pi/2\hat{I}_x} -\hat{I}_{1y} \tag{3.54}$$

  $$\hat{I}_{1z} + \hat{I}_{2z} \xrightarrow{\pi/2\hat{I}_{1x}} \xrightarrow{\pi/2\hat{I}_{2x}} -\hat{I}_{1y} - \hat{I}_{2y} = \hat{\rho}_1 \tag{3.55}$$

  The following calculations will be shown for one spin (spin $\hat{I}_1$) for simplicity.

- **Step 2: Evolution During t_1**

  The spins evolve under both the chemical shift and the $J-$coupling. Focusing on spin $\hat{I}_1$ for clarity, the chemical shift evolution generates terms proportional to

  $$-\hat{I}_{1y} \xrightarrow{\Omega_1 t_1} -\hat{I}_{1y}\cos(\Omega_1 t_1) + \hat{I}_{1x}\sin(\Omega_1 t_1) \tag{3.56}$$

  Here the magnetization vector is rotating in the xy-plane. When incrementing t_1 and repeating the experiment many times (as done in 2D NMR), this creates a time-domain signal that oscillates at frequency Ω_1. After Fourier transform, this becomes the frequency label in the F_1 dimension.

The $J-$coupling Hamiltonian ($2\pi J_{12}\hat{I}_{1z}\hat{I}_{2z}$) drives the conversion of in-phase magnetization into anti-phase magnetization. Both terms on the right of Eq. (3.56) evolve under the coupling [8].

$$\begin{aligned} -\hat{I}_{1y}\cos(\Omega_1 t_1) &\xrightarrow{2\pi J_{12}\hat{I}_{1z}\hat{I}_{2z}t_1} -\hat{I}_{1y}\cos(\Omega_1 t_1)\cos(\pi J_{12}t_1) \\ &\quad + 2\hat{I}_{1x}\hat{I}_{2z}\cos(\Omega_1 t_1)\sin(\pi J_{12}t_1) \\ \hat{I}_{1x}\sin(\Omega_1 t_1) &\xrightarrow{2\pi J_{12}\hat{I}_{1z}\hat{I}_{2z}t_1} \hat{I}_{1x}\sin(\Omega_1 t_1)\cos(\pi J_{12}t_1) \\ &\quad + 2\hat{I}_{1y}\hat{I}_{2z}\sin(\Omega_1 t_1)\sin(\pi J_{12}t_1) \end{aligned} \tag{3.57}$$

where

- **Terms 1 & 3**: In-phase magnetization that has evolved under chemical shift but not fully converted to anti-phase (modulated by $\cos(\pi J_{12}t_1)$)
- **Terms 2 & 4**: Anti-phase magnetization (modulated by $\sin(\pi J_{12}t_1)$) which is needed for coherence transfer.

- **Step 3: Mixing Pulse and Coherence Transfer**

  The second $(\pi/2)_x$ pulse is the core of the COSY experiment [8]. It rotates the operators according to the cyclic commutation rules of angular momentum. for all the terms generated above:

  - **Term 1:** $-\hat{I}_{1y}\cos(\Omega_1 t_1)\cos(\pi J_{12}t_1)$

    $$-\hat{I}_{1y} \xrightarrow{(\pi/2)_x} -\hat{I}_{1z} \tag{3.58}$$

    This becomes **longitudinal magnetization**. It is along the z-axis (not observable since only transverse magnetization is detected). This term is lost.

  - **Term 2:** $2\hat{I}_{1x}\hat{I}_{2z}\cos(\Omega_1 t_1)\sin(\pi J_{12}t_1)$ The pulse acts on **both** operators in the product:

    $$2\hat{I}_{1x}\hat{I}_{2z} \xrightarrow{(\pi/2)(\hat{I}_{1x}+\hat{I}_{2x})} 2\hat{I}_{1x}\cdot(-\hat{I}_{2y}) = -2\hat{I}_{1x}\hat{I}_{2y} \tag{3.59}$$

    $*$ $\hat{I}_{1x}$ is unchanged (rotation about x)

* $\hat{I}_{2z}$ rotates to $-\hat{I}_{2y}$ (90° rotation about x takes z $\rightarrow -y$)

This is **multiple-quantum coherence** (specifically zero-quantum and double-quantum) [9]. Both spins have transverse magnetization simultaneously. This is not directly observable in standard NMR detection (which measures single-quantum coherence).

– **Term 3:** $\hat{I}_{1x}\sin(\Omega_1 t_1)\cos(\pi J_{12} t_1)$

$$\hat{I}_{1x} \xrightarrow{(\pi/2)_x} \hat{I}_{1x} \tag{3.60}$$

The $\hat{I}_{1x}$ operator is **unchanged** by a rotation about the x-axis (the rotation axis commutes with the operator). **This term creates the diagonal peaks because:**

* During t_1: it evolves at frequency Ω_1 ($\sin(\Omega_1 t_1)$ modulation)
* During t_2 (detection): it continues to evolve at Ω_1
* Result: a peak at coordinates (Ω_1, Ω_1) in the 2D spectrum

– **Term 4:** $2\hat{I}_{1y}\hat{I}_{2z}\sin(\Omega_1 t_1)\sin(\pi J_{12} t_1)$ Here is where the coherence transfer happens

$$2\hat{I}_{1y}\hat{I}_{2z} \xrightarrow{(\pi/2)(\hat{I}_{1x}+\hat{I}_{2x})} 2\hat{I}_{1z}\cdot(-\hat{I}_{2y}) = -2\hat{I}_{1z}\hat{I}_{2y} \tag{3.61}$$

* $\hat{I}_{1y}$ rotates to $\hat{I}_{1z}$ (90° rotation about x takes y $\rightarrow$ z)
* $\hat{I}_{2z}$ rotates to $-\hat{I}_{2y}$

This operation transfers coherence from spin 1 to spin 2. The term $-2\hat{I}_{1z}\hat{I}_{2y}$ represents detectable anti-phase magnetization on spin 2. Because this term originated from spin 1, it carries the frequency signature of spin (Ω_1) from the t_1 period but evolves at the frequency of spin 2 (Ω_2) during detection (t_2). This results in a **cross-peak** at coordinates (Ω_1, Ω_2) in the 2D spectrum [8, 9].

- **Step 4: Detection (t_2) and 2D**

During t_2 coherences that evolved as $e^{-i\omega_2 t_2}$ is detected. The 2D signal for a pathway that began on spin i in t_1 and ended on spin j in t_2 can be represented as

$$S_{ij}(t_1, t_2) \propto e^{-i\omega_i t_1} e^{-i\omega_j t_2} f_{ij}(t_1, t_2), \tag{3.62}$$

where f_{ij} encapsulates amplitude factors (relaxation, pulses, J-evolution phases). The double FT yields peaks at ($\omega_1 = \omega_i$, $\omega_2 = \omega_j$).

3.5.1.3 Fourier Transform and Correlation Functions

Mathematically the 2D FT converts $S(t_1, t_2)$ into $S(\omega_1, \omega_2)$. If we define signals $s_i(t)$ for coherence pathways associated with spin i, then

$$S(\omega_1, \omega_2) = \iint S(t_1, t_2) e^{-i(\omega_1 t_1 + \omega_2 t_2)} \, dt_1 dt_2. \tag{3.63}$$

diagonal peaks correspond to correlations of the form $s_i(t_1)s_i^*(t_2)$ (autocorrelation in the 2D sense), while cross peaks correspond to cross-terms $s_i(t_1)s_j^*(t_2)$ (cross-correlation between spins i and j).

3.5.1.4 The 2D COSY Spectrum

After collecting data for many t_1 increments and performing 2D FT:

Diagonal Peaks at (Ω_1, Ω_1) and (Ω_2, Ω_2): These result from the magnetization that remained in the same spin. They appear in **dispersion mode** (derivative-like lineshapes). This is because the in-phase term had a $\sin(\Omega_1 t_1)\cos(\pi J_{12} t_1)$ modulation, and the surviving $\hat{I}_{1x}$ component corresponds to the dispersion phase [9].

Cross Peaks at (Ω_1, Ω_2) and (Ω_2, Ω_1): These arise from the coherence transfer pathway. They appear as **anti-phase multiplets**: four peaks in a square pattern (positive, negative, negative, positive). The splitting is J_{12} in both dimensions. These can be phased to pure absorption mode [9].

3.5.2 Zero-Field Heteronuclear Correlation

The aim of a ZULF heteronuclear correlation experiment is to produce a two-dimensional dataset wherein one axis reports J-derived frequencies and the other axis reports heteronuclear-splitting-derived frequencies, thereby correlating proton-like and carbon-like responses. A practical pulse/field sequence that accomplishes this is described below.

3.5.2.1 Experimental scheme

The sequence has five conceptual stages:

1. **Polarization:** Polarize the sample at high field B_{pol} (1–2 T) to generate Boltzmann polarization primarily on protons.
2. **Transfer / Shuttle:** Rapidly move the sample into the zero-field region, or perform a fast field ramp-down to near-zero (nonadiabatic quench) to convert longitudinal populations into zero-field coherences.
3. **Evolution 1 (t_1):** Apply a controlled small longitudinal field B_z during a variable evolution period t_1 to allow phase accrual from $\nu_{\pm}$ components (this encodes heteronuclear splitting information on the indirect axis).
4. **Mixing:** Optionally apply a short zero-field mixing pulse or a brief transverse bias field to convert heteronuclear coherence pathways into observable transverse magnetization.

$$S_0 \xrightarrow{\text{Evolution under } J + B_z} T_0 \xrightarrow{\text{Mixing pulse}} M_x$$

Coherence conversion: $S_0 \to T_0 \to M_x$

Figure 3.9: Singlet S_0 population is converted into T_0 coherence and then into transverse magnetization M_x that can be detected at ZULF.

5. **Detection (t_2):** Set $B \approx 0$ for detection and record $M_x(t)$ with an OPM. Fourier transform the direct time axis (t_2) to obtain the J-spectrum, and Fourier transform the indirect encoded dimension (t_1) to obtain heteronuclear correlation information.

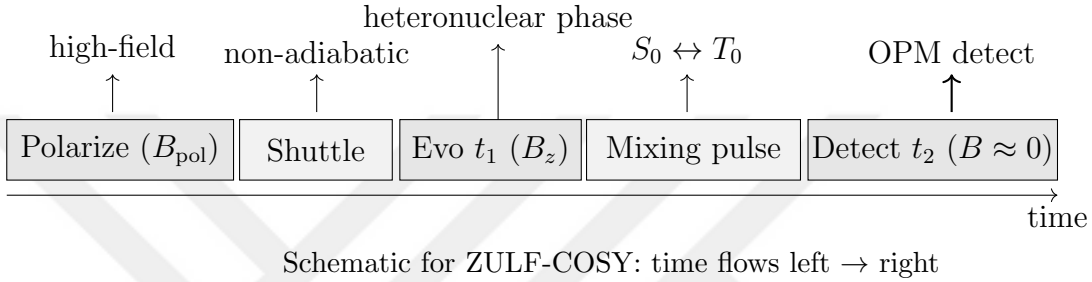


Figure 3.10: Pulse and field sequence used for heteronuclear zero-field correlation spectroscopy.

3.5.2.2 Quantum description of encoding

Let the initial density operator after polarization and nonadiabatic quench be $\hat{\rho}_0$. During the evolution period t_1 under $\hat{H}_{\text{ULF}}$ the state accrues phase

$$\hat{\rho}(t_1) = e^{-2\pi i \hat{H}_{\text{ULF}} t_1}\, \hat{\rho}_0\, e^{2\pi i \hat{H}_{\text{ULF}} t_1}. \tag{3.64}$$

The signal detected during t_2 is

$$S(t_1, t_2) = \text{Tr}\left\{ \hat{M}_x\ , e^{-2\pi i \hat{H}_{\text{ZULF}} t_2}\, \hat{\rho}(t_1)\, e^{2\pi i \hat{H}_{\text{ZULF}} t_2} \right\}. \tag{3.65}$$

Here, detection is performed in the zero-field Hamiltonian frame to emphasize that the direct dimension primarily reads J-coupling frequencies. Performing a double Fourier transform in t_1 and t_2 yields a 2D spectrum $S(\nu_1, \nu_2)$ in which cross-peaks indicate correlations between heteronuclear-splitting-derived frequencies (ν_1) and J-derived frequencies (ν_2).

3.6 Fitting Procedures

The extraction of quantitative parameters from NMR data relies on fitting experimental signals to theoretical models. FID signals, relaxation curves, and other NMR observables are non-linear functions of the parameters of interest.

3.6.1 Nonlinear Least-Squares Optimization

The nonlinear least-squares method determines the parameter vector $\boldsymbol{\theta} = (\theta_1, \theta_2, \ldots, \theta_p)^T$ that best fits a model $f(t; \boldsymbol{\theta})$ to experimental observations $\{(t_i, y_i)\}_{i=1}^N$ by minimizing the sum of squared residuals [54]:

$$\chi^2(\boldsymbol{\theta}) = \sum_{i=1}^{N} r_i^2(\boldsymbol{\theta}) = \sum_{i=1}^{N} [y_i - f(t_i; \boldsymbol{\theta})]^2 \tag{3.66}$$

where $r_i(\boldsymbol{\theta}) = y_i - f(t_i; \boldsymbol{\theta})$ is the residual at the i-th data point. This assumes independent, normally distributed measurement errors with constant variance [55].

For datasets with varying measurement uncertainties, weighted least-squares is appropriate [56]:

$$\chi^2(\boldsymbol{\theta}) = \sum_{i=1}^{N} w_i [y_i - f(t_i; \boldsymbol{\theta})]^2 \tag{3.67}$$

where $w_i = 1/\sigma_i^2$ are weights inversely proportional to measurement variance. For FID signals, weighted fitting de-emphasizes the noisy signal tail [57].

3.6.2 The Levenberg-Marquardt Algorithm

The Levenberg-Marquardt (LM) algorithm [58, 59] is the standard approach for nonlinear least-squares problems in NMR spectroscopy. It combines the strengths of the Gauss-Newton method (rapid convergence near the minimum [60]) and steepest descent (robustness far from the minimum [61, 54]) by introducing an

adaptive damping parameter. The Jacobian matrix $\mathbf{J}$, containing first-order partial derivatives of residuals with respect to parameters [54], governs the optimization:

$$J_{ij} = \frac{\partial r_i}{\partial \theta_j} = -\frac{\partial f(t_i; \boldsymbol{\theta})}{\partial \theta_j} \tag{3.68}$$

The LM update equation adds damping to the Gauss-Newton step [62]:

$$\boldsymbol{\theta}_{k+1} = \boldsymbol{\theta}_k - (\mathbf{J}^T\mathbf{J} + \lambda\mathbf{I})^{-1}\mathbf{J}^T\mathbf{r} \tag{3.69}$$

where $\lambda \geq 0$ controls algorithm behavior [63]: small λ approximates Gauss-Newton (quadratic convergence), while large λ behaves like steepest descent (stable but slower). Marquardt's modification scales damping by parameter curvature [59, 64]:

$$\boldsymbol{\theta}_{k+1} = \boldsymbol{\theta}_k - (\mathbf{J}^T\mathbf{J} + \lambda \cdot \mathrm{diag}(\mathbf{J}^T\mathbf{J}))^{-1}\mathbf{J}^T\mathbf{r} \tag{3.70}$$

providing better scaling for parameters with different magnitudes, common in NMR where amplitudes, frequencies, and relaxation times span different scales.

The damping parameter λ adapts using a trust-region strategy [64, 63]: the gain ratio ρ compares actual versus predicted χ^2 reduction; if $\rho > 0$, the step is accepted and λ decreases, otherwise the step is rejected and λ increases [65, 66]. Convergence is detected via gradient, parameter change, or function value criteria [64, 67].

3.6.3 Parameter Uncertainty and Goodness-of-Fit

Parameter uncertainty is quantified through the covariance matrix [62, 68]:

$$\mathrm{Cov}(\boldsymbol{\theta}) = \sigma^2(\mathbf{J}^T\mathbf{J})^{-1} \tag{3.71}$$

where $\sigma^2 = \chi^2(\boldsymbol{\theta}_{\mathrm{opt}})/(N-p)$ is estimated from residuals with $N-p$ degrees of freedom. The standard error of parameter θ_j is $\mathrm{SE}(\theta_j) = \sqrt{[\mathrm{Cov}(\boldsymbol{\theta})]_{jj}}$. Off-diagonal elements reveal parameter correlations [68]; high correlation ($|\mathrm{Corr}| \approx 1$) indicates parameters are difficult to determine independently, common in NMR where amplitudes and relaxation times correlate [69]. Confidence intervals are given by $\theta_j \pm t_{\alpha/2,N-p} \cdot \mathrm{SE}(\theta_j)$ [70, 55].

3.6.4 Goodness-of-Fit

The coefficient of determination R^2 quantifies variance explained by the model [62]:

$$R^2 = 1 - \frac{\mathrm{SS}_{\mathrm{res}}}{\mathrm{SS}_{\mathrm{tot}}} = 1 - \frac{\sum_{i=1}^{N}[y_i - f(t_i;\boldsymbol{\theta})]^2}{\sum_{i=1}^{N}(y_i - \bar{y})^2} \tag{3.72}$$

where $\bar{y} = N^{-1}\sum_{i=1}^{N} y_i$ is the mean. While $R^2 \approx 1$ indicates excellent fit, it can be misleading for nonlinear models or when comparing different parameter counts [71].

The reduced chi-squared statistic provides a more rigorous measure [55]:

$$\chi^2_\nu = \frac{1}{N-p}\sum_{i=1}^{N}\frac{[y_i - f(t_i;\boldsymbol{\theta})]^2}{\sigma_i^2} \tag{3.73}$$

For a good fit with properly estimated uncertainties, $\chi^2_\nu \approx 1$. Values $\gg 1$ suggest systematic model errors or underestimated uncertainties; values $\ll 1$ indicate overestimated uncertainties [56].

Visual inspection of residuals $r_i = y_i - f(t_i;\boldsymbol{\theta})$ provides diagnostic information: randomness (no systematic patterns), homoscedasticity (constant variance, else use weighted fitting), and approximate normality [55].

3.6.5 Application to NMR Fitting

Initial parameter estimates critically affect optimization success [71]. For NMR FID analysis: amplitude from signal maximum $A_0 \approx \max_i |y_i|$ [57]; relaxation time from $1/e$ decay point or literature values ($T_{2,0} \approx 0.5$-2 s for small molecules) [69]; frequency from FFT peak $f_0 = \arg\max_f |\mathcal{F}\{s(t)\}|$ [67]; and phase from initial signal ratio $\phi_0 \approx \arctan(\mathrm{Im}[s(0)]/\mathrm{Re}[s(0)])$.

Multi-component signals require fitting $S(t) = \sum_{k=1}^{M} A_k \exp(-t/T_{2,k})\cos(\Omega_k t + \phi_k) + c$ [69], which is challenging due to high parameter correlation, multiple local minima, noise-component ambiguity, and model selection (determining appropriate M) [56].

Chapter 4

High-Field NMR Experiments

4.1 Proton NMR Analysis of Dichloromethane (CH_2Cl_2)

4.1.1 Sample Preparation and NMR Acquisition

Proton nuclear magnetic resonance (^{1}H NMR) spectroscopy was performed on neat dichloromethane (CH_2Cl_2) at room temperature (298.15 K). The measurements were acquired using a 43.466 MHz spectrometer (Spinsolve, Magritek) operating at a static magnetic field of $B_0 = 1.021$ T. The key acquisition parameters are summarized in Table 4.1.

Table 4.1: NMR Acquisition Parameters

Parameter	**Value**
Carrier frequency (ν_0)	43.466 MHz
Static magnetic field (B_0)	1.021 T
Spectral bandwidth	$\pm$2500 Hz
Number of data points	32768
Dwell time (Δt)	200 µs
Acquisition time	6.553 s
Digital resolution	0.153 Hz/point
Number of scans	1
Pulse flip angle	90°
Receiver channel	^{1}H
Shim SNR	16008.62
Shim linewidth (FWHM)	0.577 Hz

4.1.1.1 Data Processing and Analysis

The FID signal comes as complex quadrature data with real and imaginary components. We construct the complex signal using the conjugate convention (Eq (3.21)) and compute the frequency-domain spectrum via FFT with frequency-shift centering (Eq (3.26)). Fig. 4.1 shows the experimental processing workflow, while Fig. 4.2 shows how theory and experiment come together.

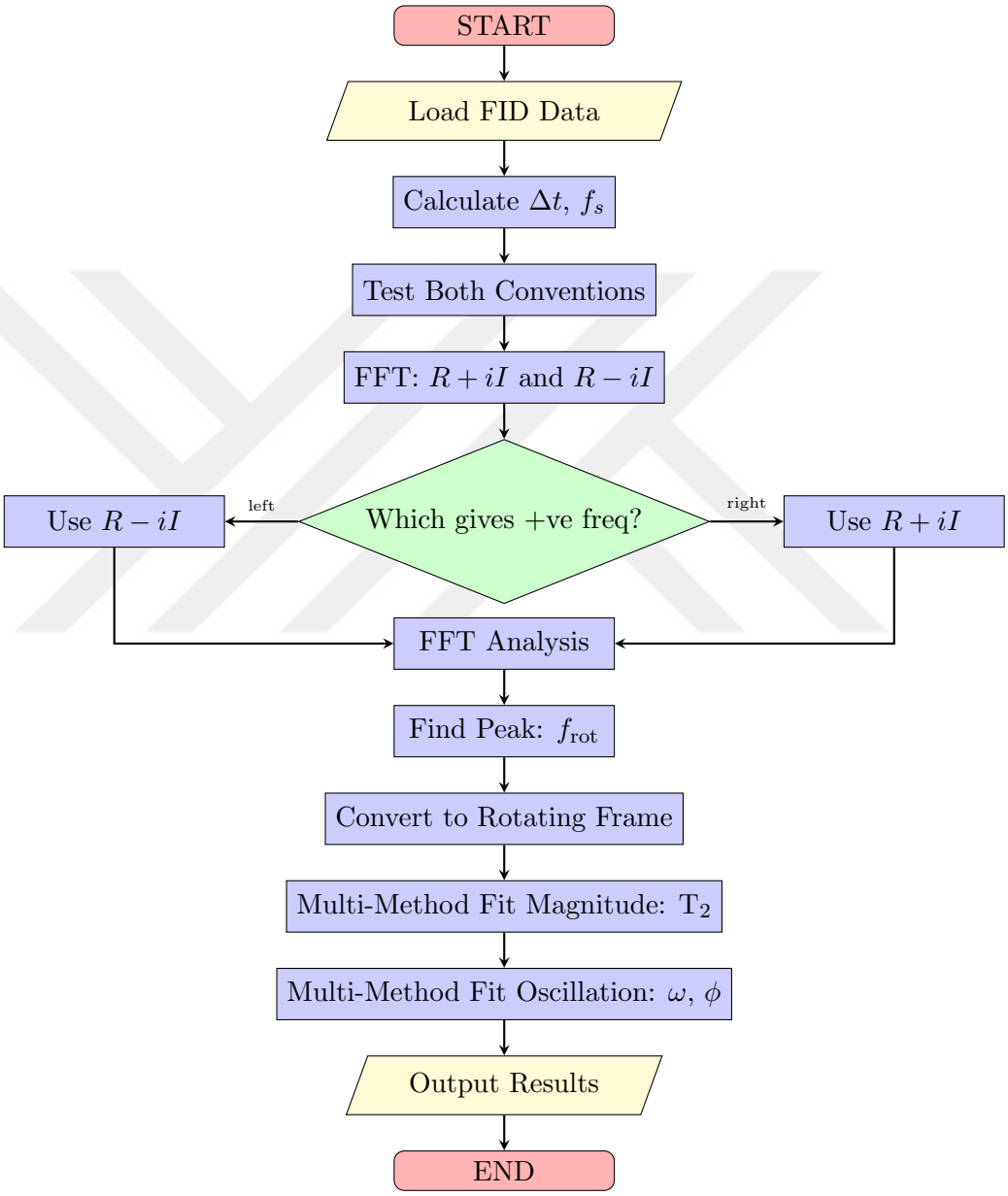


Figure 4.1: Experimental FID processing flowchart. After loading the data, both quadrature conventions ($R + iI$ and $R - iI$) are tested to determine which gives a positive frequency peak. The correct convention is then used for FFT analysis, peak detection, and frequency conversion to the lab frame. Finally, both the magnitude envelope and the oscillating signal fit to extract relaxation and phase parameters.

4.1.1.2 Data Flow Diagram

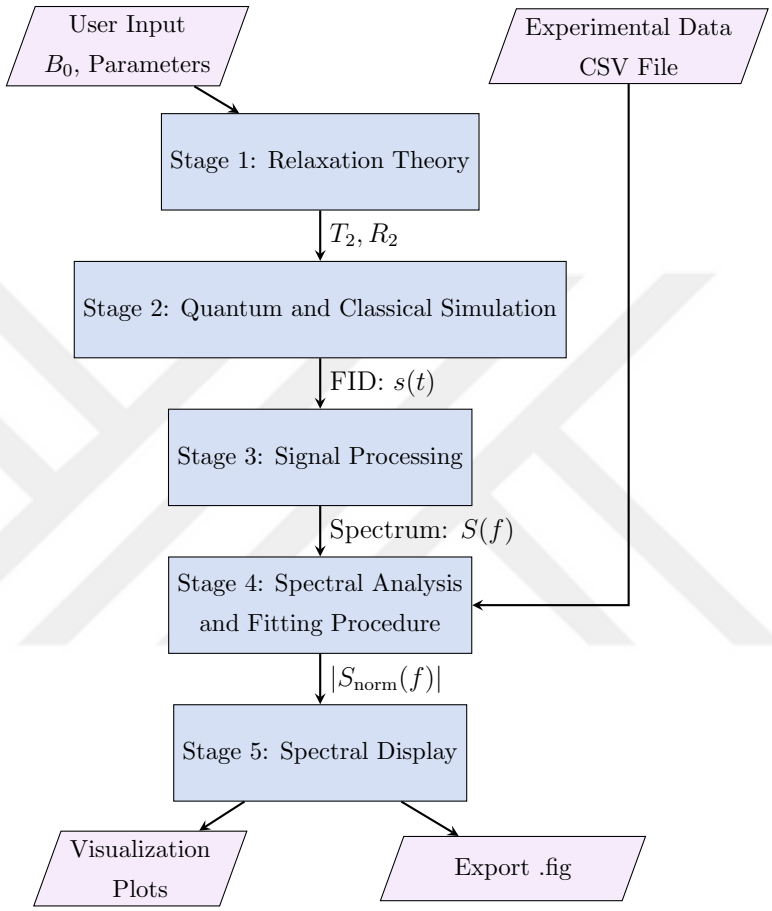


Figure 4.2: Overall workflow showing two parallel paths: theoretical prediction (left branch) and experimental analysis (right branch). The simulation path calculates T_2 from first principles, generates FID via QuTiP, and produces normalized spectra. The experimental path processes measured FID through FFT and fitting. Both converge at Stage 5 for direct comparison and visualization.

Loading the Data The FID data comes as a text file with three columns: time, real part, imaginary part. First step is just reading this in and calculating some basic parameters:

```
# Read the FID data from file
data = np.array([[time_val, real_val, imag_val], ...])
time = data[:, 0]           # Extract time points
```

```
real_part = data[:, 1]      # Real channel data
imag_part = data[:, 2]      # Imaginary channel data
# Calculate sampling parameters
dwell_time = time[1] - time[0]  # Time between points: 200 us
sampling_rate = 1 / dwell_time   # How fast we sample: 5000 Hz
magnitude = np.sqrt(real_part**2 + imag_part**2) # Magnitude of
    the FID signal
```

Listing 4.1: Loading FID data and calculating basic parameters

The dwell time is the spacing between data points. For this data, it is 200 microseconds. The sampling rate (reciprocal of dwell time) is 5000 Hz, which sets the maximum frequency we can detect.

Testing Quadrature Conventions

```
# Try both possible combinations
complex_standard = real_part + 1j * imag_part   # Plus sign
complex_conjugate = real_part - 1j * imag_part  # Minus sign

# For each one, do the FFT and find where the peak is
for complex_signal in [complex_standard, complex_conjugate]:
    # FFT: time domain -> frequency domain
    spectrum = np.fft.fftshift(np.fft.fft(complex_signal))
    # Make the frequency axis (in Hz)
    freqs = np.fft.fftshift(np.fft.fftfreq(len(complex_signal), d
   =dwell_time))
    # Find the peak
    peak_freq = freqs[np.argmax(np.abs(spectrum))]
```

Listing 4.2: Testing both quadrature conventions

The `fftshift` function is important here. It reorganizes the FFT output so that zero frequency sits in the middle, with negative frequencies on the left and positive on the right. Without this, the frequency axis would be scrambled.

After testing both, the conjugate convention ($R - iI$) gave a positive frequency

(+30.21 Hz), which makes sense. The standard convention gave a negative frequency, which would be wrong for this peak.

FFT to Get the Spectrum Once the correct sign convention was known, obtaining the spectrum was straightforward:

```
# Build the complex signal (using conjugate convention)
complex_fid = real_part - 1j * imag_part

# Do the FFT (N points in gives N points out)
spectra = np.fft.fftshift(np.fft.fft(complex_fid))

# Build the frequency axis
# fftfreq makes frequencies from -fs/2 to +fs/2
freqs = np.fft.fftshift(np.fft.fftfreq(len(complex_fid), d=
    dwell_time))

# Get the magnitude at each frequency
mag_spectrum = np.abs(spectra)

# Find where the peak is
peak_idx = np.argmax(mag_spectrum)
rotating_frame_freq = freqs[peak_idx]  # This gives +30.21 Hz
```

Listing 4.3: Computing the frequency spectrum

Converting to Lab Frame The FFT peak is at 30.21 Hz in the rotating frame. To convert to the laboratory frame frequency, we apply an offset correction based on the spectrometer calibration parameters from the JCAMP-DX file header:

$$\begin{aligned} \text{BF1 (Base frequency)} &= 43.4661128092557 \text{ MHz} \\ \text{SF (Spectrometer frequency)} &= 43.4659067479647 \text{ MHz} \\ f_{\text{offset}} &= \text{BF1} - \text{SF} = 206.06 \text{ Hz} \end{aligned}$$

Where **BF1** is the actual RF transmitter frequency used for excitation and **SF** is the reference frequency used by the spectrometer for frequency calibration. This offset corrects for the internal frequency difference between the transmitter and reference oscillator.

The laboratory frame frequency is obtained by adding this offset:

$$f_{\text{lab}} = f_{\text{rot}} + f_{\text{offset}} = 30.21 + 206.06 = 236.27 \text{ Hz} \tag{4.1}$$

This 236.35 Hz represents the absolute frequency that would be observed on the spectrometer display. The FFT signal amplitude is normalized to the number of points.

4.2 Free Induction Decay Signal Analysis and Fitting Methods

The accurate extraction of transverse relaxation time (T_2) from NMR FID signals is crucial for characterizing molecular dynamics and sample properties. In high-field NMR systems operating at 1.02 T, the FID signal exhibits both magnitude envelope decay and oscillatory behavior at the Larmor frequency. This section presents a comprehensive comparison of different fitting methodologies applied to experimental CH_2Cl_2 FID data to determine the most physically meaningful and statistically robust approach for T_2 extraction.

4.2.1 FID Signal in the Lab Frame

In the laboratory reference frame, the detected transverse magnetization from a spin ensemble following a 90° pulse can be expressed as:

$$M_{xy}(t) = M_0 \cdot e^{-t/T_2} \cdot e^{i(\omega_0 t + \phi)} \tag{4.2}$$

where M_0 is the initial magnetization amplitude, T_2 is the transverse (spin-spin) relaxation time constant, $\omega_0 = \gamma B_0$ is the Larmor angular frequency (γ is the gyromagnetic ratio and B_0 is the static magnetic field), and ϕ is the initial phase offset determined by detection timing.

For quadrature detection schemes, the signal is recorded as real and imaginary components:

$$\text{Real:} \quad R(t) = M_0 \cdot e^{-t/T_2} \cdot \cos(\omega_0 t + \phi) \tag{4.3}$$

$$\text{Imaginary:} \quad I(t) = M_0 \cdot e^{-t/T_2} \cdot \sin(\omega_0 t + \phi) \tag{4.4}$$

The complex signal is constructed using the conjugate convention: $M_{xy}(t) = R(t) - iI(t)$, which corresponds to the standard NMR acquisition convention for quadrature detection. The magnitude envelope, which is independent of phase, is given by:

$$|M_{xy}(t)| = M_0 \cdot e^{-t/T_2} \tag{4.5}$$

The transverse relaxation time T_2 is formally defined as the time at which the transverse magnetization decays to $1/e$ (approximately 37%) of its initial value:

$$|M_{xy}(T_2)| = \frac{M_0}{e} \approx 0.368 \cdot M_0 \tag{4.6}$$

Two categories of fitting approaches were investigated: (1) magnitude envelope fits applied to $|M_{xy}(t)|$, and (2) oscillating signal fits applied directly to the real component $R(t)$ with explicit phase modeling.

4.2.2 Magnitude Envelope Fitting Methods

Four functional forms were tested for fitting the magnitude envelope:

Exponential Decay Model: The single-exponential model assumes pure transverse relaxation:

$$|M_{xy}(t)| = A \cdot e^{-t/T_2} + B \tag{4.7}$$

where A is the signal amplitude, T_2 is the transverse relaxation time, and B is a baseline offset. This model has three free parameters and is directly motivated by the Bloch equations.

Bi-Exponential Decay Model: For systems with heterogeneous relaxation environments (e.g., molecules in different chemical environments or with exchange processes):

$$|M_{xy}(t)| = A_1 \cdot e^{-t/T_{2,1}} + A_2 \cdot e^{-t/T_{2,2}} + B \tag{4.8}$$

where A_1 and A_2 are the amplitudes of the fast and slow relaxing components with relaxation times $T_{2,1}$ and $T_{2,2}$, respectively. An effective T_2 can be computed as a weighted average:

$$T_{2,\text{eff}} = \frac{A_1 T_{2,1} + A_2 T_{2,2}}{A_1 + A_2} \tag{4.9}$$

Polynomial Envelope Model: A flexible empirical model using polynomial correction to the exponential form:

$$|M_{xy}(t)| = A \cdot \left(1 + \sum_{i=1}^{N} c_i t^i\right) \tag{4.10}$$

where c_i are polynomial coefficients (typically $N = 10$). While highly flexible, this model lacks direct physical interpretation. The effective T_2 is extracted by numerically solving:

$$1 + \sum_{i=1}^{N} c_i T_2^i = \frac{1}{e} \tag{4.11}$$

to find the time when the signal reaches 37% of its initial value.

Shifted Power Law Model: An alternative non-exponential model:

$$|M_{xy}(t)| = A \cdot (t + t_0)^{-n} + B \tag{4.12}$$

where n is the power law exponent and t_0 is a time shift parameter. The effective T_2 is determined from the fitted curve as the time when $|M_{xy}(T_2)| = M_0/e$.

4.2.3 Oscillating Signal Fitting Methods

Three methods were applied directly to the real-valued oscillating FID signal:

Oscillating Exponential Model: This model directly fits the lab-frame signal with exponential envelope:

$$R(t) = A \cdot e^{-t/T_2} \cdot \cos(\omega_0 t + \phi) + B \tag{4.13}$$

This five-parameter model (A, T_2, ω_0, ϕ, B) is the most physically motivated, directly derived from the Bloch equations, and allows simultaneous extraction of both relaxation time and Larmor frequency.

Oscillating Polynomial Model: An empirical approach with polynomial envelope modulation:

$$R(t) = A \cdot \left(1 + \sum_{i=1}^{N} c_i t^i\right) \cdot \cos(\omega_0 t + \phi) \tag{4.14}$$

This highly flexible model can capture non-exponential envelope behavior but lacks physical interpretation.

Oscillating Bi-Exponential Model: For multi-component systems:

$$R(t) = \left[A_1 e^{-t/T_{2,1}} + A_2 e^{-t/T_{2,2}}\right] \cdot \cos(\omega_0 t + \phi) + B \tag{4.15}$$

This seven-parameter model can resolve multiple relaxation components when present.

4.2.4 Fitting Procedure and Statistical Analysis

All fitting was performed using the Levenberg-Marquardt nonlinear least-squares algorithm implemented in SciPy's `curve_fit` function. Initial parameter estimates were obtained from:

- A: Maximum signal amplitude
- T_2: Approximate time constant from visual inspection (0.5–2 s)
- ω_0: Larmor frequency from FFT peak position

- ϕ: Initial phase estimate from zero-time signal value

The quality of fit was assessed using the coefficient of determination (R^2):

$$R^2 = 1 - \frac{SS_{\text{res}}}{SS_{\text{tot}}} = 1 - \frac{\sum_i (y_i - f_i)^2}{\sum_i (y_i - \bar{y})^2} \tag{4.16}$$

where y_i are the experimental data points, f_i are the fitted values, and $\bar{y}$ is the mean of the data. Values of R^2 closer to unity indicate better agreement between model and data. Parameter uncertainties were estimated from the covariance matrix of the fit, with standard errors given by $\sigma_j = \sqrt{C_{jj}}$, where C is the covariance matrix.

4.3 Theoretical Framework and Simulation Methods

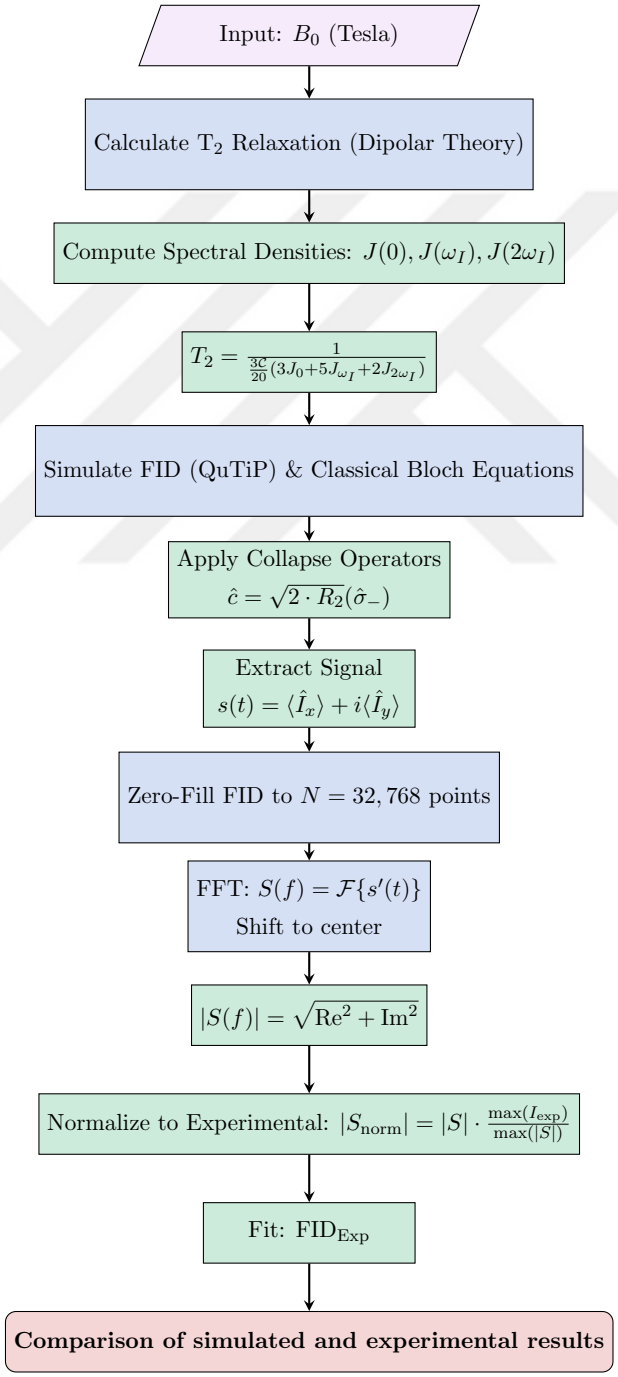


Figure 4.3: Complete algorithm flowchart for NMR simulation

4.3.1 Physical Constants and Molecular Parameters

The theoretical calculations employed the following physical constants and molecular parameters for CH_2Cl_2 (Table 4.2).

Table 4.2: Simulation Parameters for CH_2Cl_2

Parameter	**Symbol**	**Value**
Proton gyromagnetic ratio	$\gamma_H/2\pi$	$42.577\,\mathrm{MHz\,T^{-1}}$
H–H internuclear distance	r_{IS}	$1.77\,\text{Å}$
Hydrodynamic radius	a	$2.9\,\text{Å}$
Temperature	T	$298.15\,\mathrm{K}$
Viscosity of CH_2Cl_2	η	$0.413\,\mathrm{mPa\,s}$
Vacuum permeability	μ_0	$4\pi \times 10^{-7}\ \mathrm{T{\cdot}m/A}$
Reduced Planck constant	$\hbar$	$1.055 \times 10^{-34}\,\mathrm{J\,s}$
Boltzmann constant	k_B	$1.381 \times 10^{-23}\,\mathrm{J\,K^{-1}}$
Chemical shift (CH_2Cl_2)	δ	$5.43\,\mathrm{ppm}$

4.3.2 Correlation Time Calculation

The rotational correlation time was estimated using the Stokes-Einstein-Debye equation for isotropic rotational diffusion (Eq. (3.41)) yielding a correlation time of approximately $0.010\,\mathrm{ns}$ for CH_2Cl_2 at $298\,\mathrm{K}$. The parameters of the chemical sample were obtained from [72].

4.3.3 Dipolar Relaxation Theory

The T_2 relaxation rate due to intramolecular dipole-dipole interactions was calculated using the Solomon-Bloembergen equations. For a homonuclear two-spin system (Eq. (3.44)) and the spectral density functions (Eq. (3.45))

4.3.4 Effective T_2^* and Field Inhomogeneity

The experimentally observed relaxation time T_2^* includes contributions from both molecular relaxation (T_2) and magnetic field inhomogeneity (T_2'):

$$\frac{1}{T_2^*} = \frac{1}{T_2} + \frac{1}{T_2'} \tag{4.17}$$

where the field gradient contribution is related to the shimming linewidth:

$$T_2' = \frac{1}{\pi \cdot \mathrm{FWHM}_{\mathrm{shim}}} \tag{4.18}$$

4.3.5 Bloch Equation Simulation

The FID signal was simulated using the classical Bloch equations in the rotating reference frame. For magnetization $\mathbf{M} = (M_x, M_y, M_z)^T$:

$$\frac{dM_x}{dt} = \omega_0 M_y - \frac{M_x}{T_2} \tag{4.19}$$

$$\frac{dM_y}{dt} = -\omega_0 M_x - \frac{M_y}{T_2} \tag{4.20}$$

$$\frac{dM_z}{dt} = \frac{M_0 - M_z}{T_1} \tag{4.21}$$

where ω_0 is the spectrometer offset in the rotating frame.

The analytical solution after a 90_y^o pulse ($M_x(0) = M_0$, $M_y(0) = 0$) is:

$$M_x(t) = M_0 \cdot e^{-t/T_2} \cdot \cos(\omega_0 t) \tag{4.22}$$

$$M_y(t) = M_0 \cdot e^{-t/T_2} \cdot \sin(\omega_0 t) \tag{4.23}$$

For the two equivalent protons in CH_2Cl_2 with field gradient splitting ΔB:

$$\omega_1 = \omega_0 \tag{4.24}$$

$$\omega_2 = \omega_0 + \Delta B \tag{4.25}$$

The total complex signal is:

$$S(t) = \frac{1}{2}\left[(M_{x1} + M_{x2}) - i(M_{y1} + M_{y2})\right] \tag{4.26}$$

4.3.6 Lindblad Master Equation Simulation

For quantum mechanical simulation, the time evolution of the density matrix $\hat{\rho}(t)$ was computed using the Lindblad master equation, see Equation (3.35).

The system Hamiltonian in the rotating frame is:

$$H = \omega_1 I_{z1} + \omega_2 I_{z2} + 2\pi J(I_{x1}I_{x2} + I_{y1}I_{y2} + I_{z1}I_{z2}) \tag{4.27}$$

where $J = 0$ for the magnetically equivalent protons in CH_2Cl_2.

The T_2 relaxation collapse operators are:

$$C_n = \sqrt{2 \cdot R_2} \cdot (I_{xn} - iI_{yn}) \tag{4.28}$$

where $R_2 = 1/T_2$ and the index n labels the spin. The derivation of this form and the origin of the $\sqrt{2R_2}$ normalization factor are presented in Section 4.4.5.

The initial state after a 90°_y pulse is:

$$\rho_0 = \rho_1 \otimes \rho_2 = |\psi_1\rangle\langle\psi_1| \otimes |\psi_2\rangle\langle\psi_2| \tag{4.29}$$

where $|\psi_i\rangle = \frac{1}{\sqrt{2}}(|0\rangle + |1\rangle)$ corresponds to transverse magnetization along $+x$.

The observable total magnetization is:

$$S_x(t) = \mathrm{Tr}[\rho(t)(I_{x1} + I_{x2})] \tag{4.30}$$

$$S_y(t) = \mathrm{Tr}[\rho(t)(I_{y1} + I_{y2})] \tag{4.31}$$

The quantum simulations were implemented using QuTiP (Quantum Toolbox in Python) with the `mesolve` function for numerical integration of the master equation.

4.4 Results

4.4.1 Experimental FID and Spectral Analysis

The acquired FID signal showed clear oscillatory behavior with an exponential-like decay envelope (Fig. 4.4).

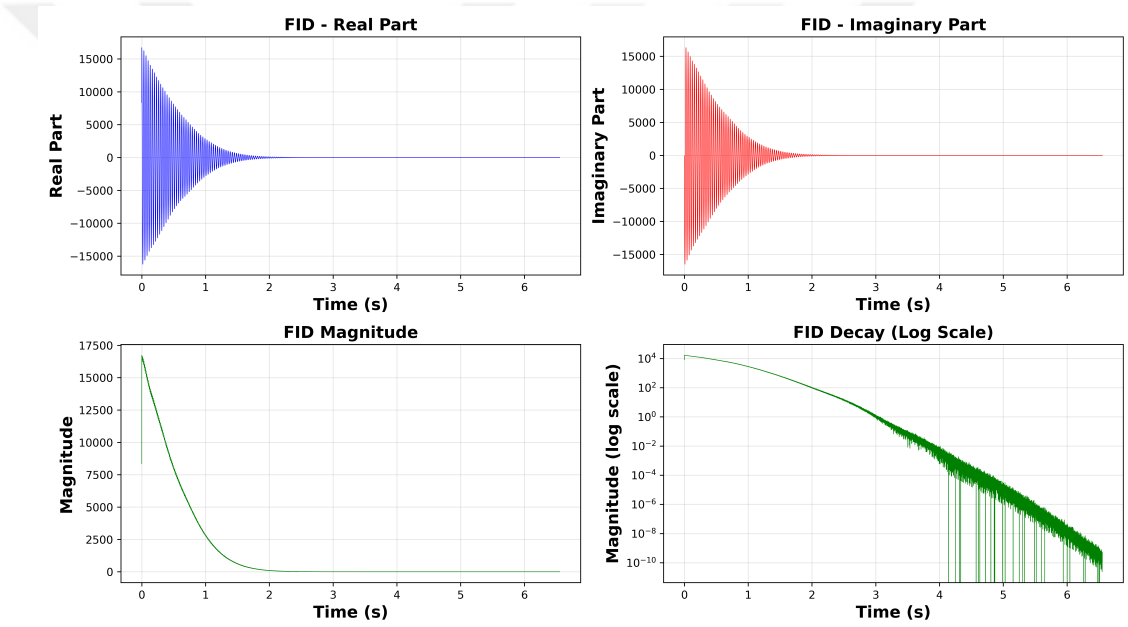


Figure 4.4: Experimental FID signal of CH_2Cl_2 at 1.02 T. Top left: Real component showing oscillations at Larmor frequency. Top right: Imaginary component (quadrature channel). Bottom left: Magnitude envelope showing exponential-like decay. Bottom right: Magnitude on logarithmic scale demonstrating T_2^*-dominated decay over 6.5 s acquisition time.

The FFT analysis yielded a single peak corresponding to the CH_2Cl_2 proton resonance (Fig. 4.5):

- **Peak frequency (rotating frame):** +30.21 Hz
- **Peak frequency (laboratory frame):** 236.27 Hz

- **Reference shift:** 206.6 Hz (relative to water)

To clarify the various frequency terms used throughout this analysis, Table 4.3 summarizes the key frequency values and their definitions.

Table 4.3: Frequency Terms and Their Definitions

Symbol	**Value**	**Definition**
f_{rot}	30.21 Hz	FFT peak in rotating frame
$f_{\omega,\text{fit}}$	30.2852 Hz	Fitted oscillation frequency
f_{offset}	-206.06 Hz	Transmitter offset (BF1 - SF)
f_{lab}	236.27 Hz	Laboratory frame frequency
$\delta_{CH_2Cl_2}$	5.43 ppm	Chemical shift vs TMS

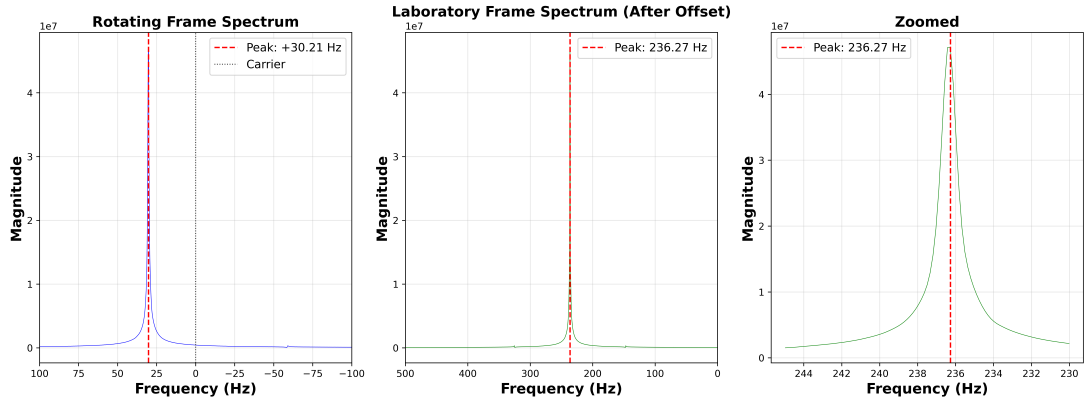


Figure 4.5: Frequency-domain analysis of CH_2Cl_2 FID. Top: Magnitude spectrum in rotating frame showing single peak at +30.21 Hz with FWHM = 0.577 Hz. Bottom: Spectrum converted to laboratory frame (236.27 Hz absolute frequency) by adding transmitter offset of 206.06 Hz, demonstrating chemical shift of 5.43 ppm relative to TMS reference.

4.4.2 T_2 Relaxation Analysis and Method Evaluation

Multiple fitting models were applied to the FID magnitude envelope to extract the transverse relaxation time. The results are summarized in Table 4.4.

Table 4.4: Comparison of magnitude envelope fitting methods for CH_2Cl_2 FID data

Fitting Method	T_2^* **(s)**	R^2	**Parameters**	**Recommended**
Exponential	0.569 ± 0.001	**0.993**	**3**	**Yes**[†]
Bi-exponential	0.569 ± 0.005	0.993	5	No
Polynomial (10th order)	0.652 ± 0.003	0.9999	11	No[‡]
Shifted Power Law	0.523 ± 0.008	0.984	4	No

[†]Recommended: Physically motivated, parsimonious, robust extrapolation

[‡]Highest R^2 but lacks physical foundation; prone to overfitting

4.4.2.1 Evaluation Criteria

The selection of the optimal fitting method must balance three considerations:

1. **Physical justification**: Does the model arise from fundamental principles of NMR relaxation?
2. **Statistical quality**: Does the fit adequately describe the data ($R^2 > 0.99$)?
3. **Parsimony**: Does the model avoid overfitting with unnecessary parameters (Occam's razor)?

4.4.2.2 Magnitude Envelope Analysis

The **exponential model** demonstrates excellent fit quality ($R^2 = 0.992951$) with only three parameters. Most importantly, it is directly derived from the Bloch equations under the assumption of homogeneous transverse relaxation, making it the natural choice for pure liquid samples. The extracted $T_2^* = 0.569$ s is physically reasonable for CH_2Cl_2 at 1.02 T.

The **bi-exponential model** achieves nearly identical $R^2 = 0.992950$ with five parameters, and the weighted average $T_2^* = 0.569$ s is essentially identical to the single-exponential result. This suggests that the two components have very similar relaxation times, and the data does not exhibit genuine multi-component relaxation.

The **polynomial model** achieves the highest $R^2 = 0.999875$ due to its 11 adjustable parameters, but this comes at the cost of physical interpretability. While it provides excellent empirical fitting: (1) extrapolation beyond the fitted range is unreliable, (2) the T_2 extraction requires numerical root-finding rather than being a direct fit parameter, and (3) higher-order polynomial terms can introduce spurious oscillations. The **shifted power law model** shows the poorest fit ($R^2 = 0.984214$) and has no theoretical justification in standard NMR relaxation theory.

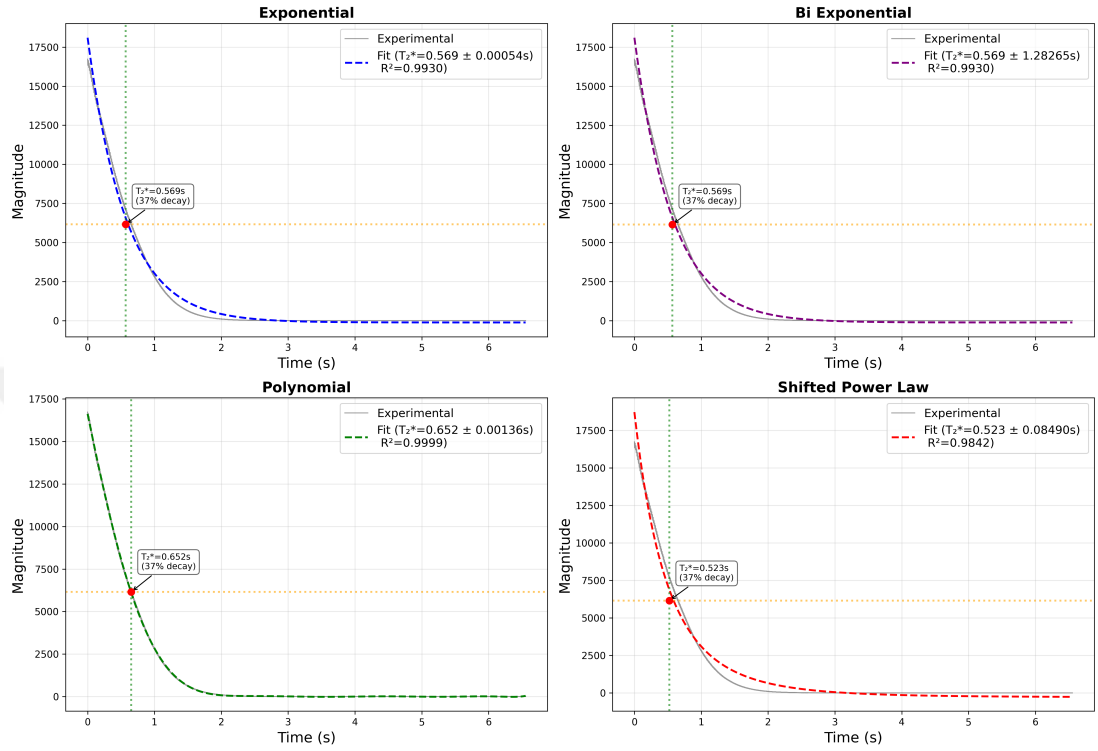


Figure 4.6: Comparison of magnitude envelope fitting methods for extracting T_2^* from experimental CH_2Cl_2 FID data. Top: Four models (exponential, bi-exponential, polynomial, shifted power law) fitted to the magnitude envelope. The 10th-degree polynomial (green) achieves highest $R^2 = 0.9999$ but with 11 parameters. Bottom: Residuals showing systematic deviations for exponential models (blue, red) at early times, while polynomial residuals are near zero across the full acquisition window.

4.4.3 Oscillating Signal Fitting Analysis

Beyond the magnitude envelope, we fitted the oscillating FID signal directly to extract frequency, phase, and decay parameters simultaneously. Results from the three oscillating models are summarized in Table 4.5.

Table 4.5: Comparison of oscillating signal fitting methods with phase parameter for direct fitting of real FID signal

Method	**Amplitude**	T_2^* **(s)**	R^2	**Parameters**
Osc. Exponential	18181 ± 12	0.556 ± 0.001	0.992955	5
Osc. Polynomial	16588 ± 5	0.640	0.999586	13
Osc. Bi-exponential	18125 ± 835	0.558 ± 0.006	0.992005	7

4.4.3.1 Oscillating Signal Analysis

The **oscillating exponential model** achieves $R^2 = 0.992955$ and provides the most direct connection to NMR physics. It simultaneously extracts:

- $T_2^* = 0.556 \pm 0.001$ s (in excellent agreement with magnitude envelope exponential fit: 0.569 s)
- Larmor frequency $f_0 = 30.29 \pm 0.0003$ Hz (verifying field calibration)
- Signal amplitude $A = 18181 \pm 12$ (arbitrary units)
- Phase $\phi = -2.02 \pm 0.04°$ (detection timing offset)

The excellent consistency of T_2^* between magnitude (0.569 s) and oscillating exponential (0.556 s) fits validates the exponential decay assumption and demonstrates the robustness of the measurement.

The **oscillating polynomial model** shows the highest $R^2 = 0.999586$ but requires 13 parameters, making it highly susceptible to overfitting. While it provides excellent empirical fit quality, the $T_2^* = 0.640$ s differs from other methods, and the polynomial approach lacks physical justification.

The **oscillating bi-exponential model** ($R^2 = 0.992005$) shows weighted $T_2^* = 0.558$ s, consistent with the single-exponential result. However, analysis reveals the fast component contributes only 7.7% of the total amplitude compared

to the slow component, with similar relaxation times. This indicates a dominant single-exponential behavior with a small, possibly spurious, fast component arising from fitting noise.

4.4.3.2 Conclusion and Recommendation

Based on the comprehensive analysis of seven fitting approaches, the following conclusions are drawn:

1. **For magnitude envelope fitting:** The **exponential decay model** is the optimal choice. It provides direct physical interpretation from Bloch equation solutions, excellent statistical fit ($R^2 > 0.992$) with minimal parameters, and direct extraction of T_2^* as a fit parameter with reliable extrapolation behavior.

2. **For oscillating signal fitting:** The **oscillating exponential model** is strongly recommended. It offers physically motivated form derived from first principles, simultaneous extraction of both T_2^* and Larmor frequency, validation through consistency with magnitude fits, and natural incorporation of phase information.

3. **Multi-component models** (bi-exponential) should be reserved for samples with known chemical heterogeneity, systems exhibiting clear multi-exponential behavior in residuals, or cases where single-exponential fits show systematic deviations ($R^2 < 0.99$).

4. **Empirical models** (polynomial, power law) lack physical foundation and should only be used for purely descriptive curve fitting when physical models fail.

For the CH_2Cl_2 system studied here at 1.02 T, the exponential decay models provide physically meaningful, statistically robust, and parsimonious descriptions of the FID signal. The extracted transverse relaxation time ranges from

$T_2^* = 0.556$ s (oscillating exponential fit) to 0.652 s (polynomial fit), with the average value $T_2^* = 0.60 \pm 0.05$ s. While the polynomial model provides the best statistical fit ($R^2 = 0.9999$), the exponential model is recommended for its physical foundation and can be confidently used for comparison with theoretical predictions from Bloembergen-Purcell-Pound (BPP) relaxation theory and quantum mechanical simulations.

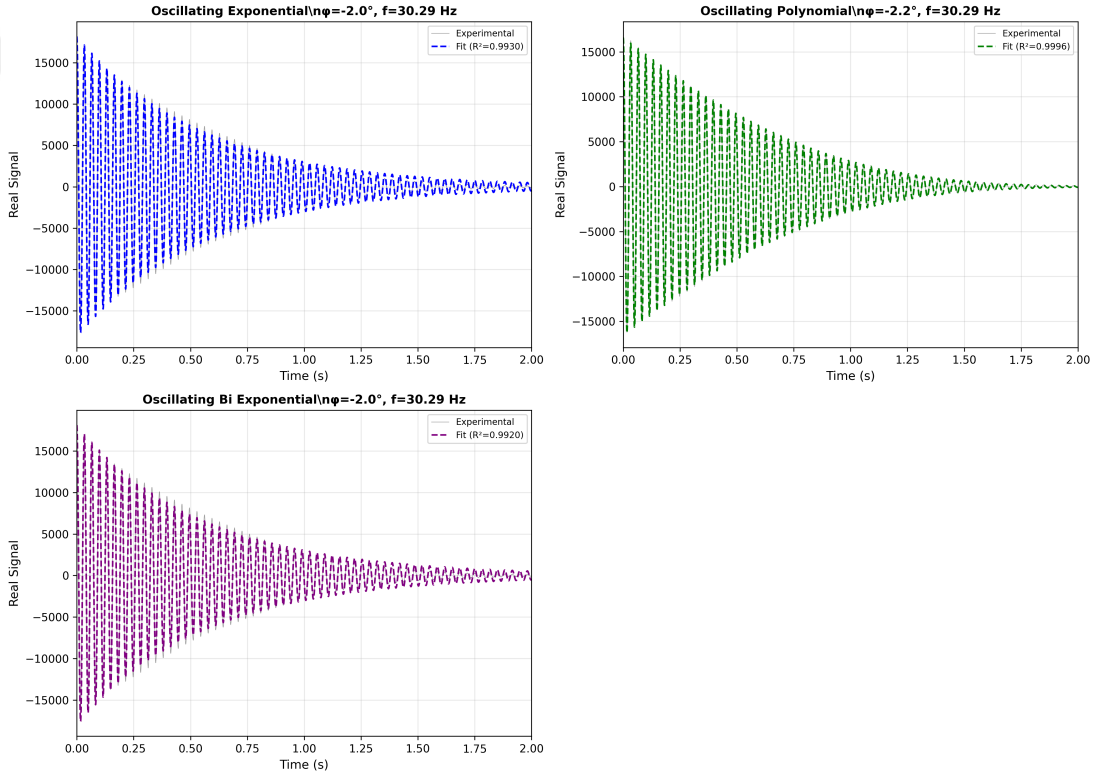


Figure 4.7: Direct fitting of oscillating real FID component using three models: oscillating exponential (5 params, $T_2^* = 0.556$ s), oscillating polynomial (13 params, $T_2^* = 0.640$ s), and oscillating bi-exponential (7 params, weighted $T_2^* = 0.558$ s). All models successfully extract Larmor frequency ($\sim$30.29 Hz) and phase ($\sim -2°$), with polynomial achieving best fit ($R^2 = 0.9996$) at cost of physical interpretability. Exponential model recommended for balance of accuracy and parsimony.

4.4.4 Theoretical Relaxation Calculations

Using the Solomon-Bloembergen theory with the molecular parameters for CH_2Cl_2:

- **Molecular T_2 (theory):** 3.511 s (dipolar relaxation only)
- **Correlation time (τ_c):** 0.010 ns
- **T_2' (field gradient):** 0.552 s (from FWHM = 0.577 Hz)
- **Predicted T_2^* (theory):** 0.477 s

The relationship between theoretical and experimental values:

$$\frac{1}{T_2^*} = \frac{1}{T_2} + \frac{1}{T_2'} = \frac{1}{3.51} + \frac{1}{0.552} \approx 2.09\,\text{s}^{-1} \tag{4.32}$$

4.4.5 Analytical Solution with Collapse Operators

To rigorously validate the numerical Lindblad equation approach, we first derive the collapse operator form from fundamental principles, then obtain the analytical solution for transverse magnetization decay.

4.4.5.1 Derivation of Collapse Operators

The T_2 relaxation collapse operators describe transverse magnetization decay through random field fluctuations. To derive their form, we start from the requirement that the Lindblad master equation [46, 48] must reproduce the phenomenological Bloch equations in the secular approximation.

It is crucial to distinguish between two relaxation mechanisms in NMR:

- T_1 **(longitudinal) relaxation:** Recovery of M_z toward thermal equilibrium, governed by operators proportional to $\hat{I}_z$. This describes energy exchange with the lattice and population transfer between spin states.
- T_2 **(transverse) relaxation:** Decay of M_x and M_y due to phase decoherence, governed by lowering operators $\sigma^- = \hat{I}_x - i\hat{I}_y$. This describes loss of phase coherence between spins without energy exchange.

For FID measurements following a 90° pulse, all magnetization is initially in the transverse plane ($M_z \approx 0$), and the observed signal decay is purely a T_2 process. Therefore, the appropriate collapse operators must act on the transverse coherences ρ_{01} and ρ_{10}, not the populations ρ_{00} and ρ_{11}.

The classical Bloch equations [52] for transverse magnetization components are:

$$\frac{dM_x}{dt} = -\frac{M_x}{T_2} \tag{4.33}$$

$$\frac{dM_y}{dt} = -\frac{M_y}{T_2} \tag{4.34}$$

(in the rotating frame, neglecting precession). Defining the complex transverse magnetization $M_+ = M_x + iM_y$:

$$\frac{dM_+}{dt} = -\frac{M_+}{T_2} \tag{4.35}$$

For a spin-1/2 system, the transverse magnetization relates to the density matrix coherence. Using the Pauli matrices σ_x, σ_y and spin-1/2 operators $\hat{I}_x = \frac{1}{2}\sigma_x$, $\hat{I}_y = \frac{1}{2}\sigma_y$:

$$\hat{I}_x + i\hat{I}_y = \frac{1}{2}(\sigma_x + i\sigma_y) = \frac{1}{2}\begin{pmatrix} 0 & 2 \\ 0 & 0 \end{pmatrix} = \sigma^- \tag{4.36}$$

where the factor of 2 arises from $\sigma_x + i\sigma_y = 2|0\rangle\langle 1| = 2\sigma^-$. Therefore:

$$M_+ \propto \mathrm{Tr}[\hat{\rho}(\hat{I}_x + i\hat{I}_y)] = \mathrm{Tr}[\hat{\rho}\sigma^-] = \rho_{10} \tag{4.37}$$

where $\rho_{10} = \langle 1|\hat{\rho}|0\rangle$. Since $M_+ = A\rho_{10}$ for some constant A, taking the time derivative gives:

$$\frac{dM_+}{dt} = -\frac{M_+}{T_2} = -\frac{A\rho_{10}}{T_2} \quad \Rightarrow \quad A\frac{d\rho_{10}}{dt} = -\frac{A\rho_{10}}{T_2} \tag{4.38}$$

The proportionality constant A cancels, yielding the quantum Bloch equation:

$$\frac{d\rho_{10}}{dt} = -\frac{1}{T_2}\rho_{10} = -R_2\rho_{10} \tag{4.39}$$

which describes the experimentally observed exponential decay of transverse magnetization.

The Lindblad dissipator for a general collapse operator $\hat{C}$ contributes:

$$\mathcal{D}[\hat{C}]\hat{\rho} = \hat{C}\hat{\rho}\hat{C}^\dagger - \frac{1}{2}\{\hat{C}^\dagger\hat{C}, \hat{\rho}\} \tag{4.40}$$

Choosing the lowering operator form $\hat{C} = c\,\sigma^- = c(I_x - iI_y)$ where $\sigma^- = |0\rangle\langle 1|$ and c is a normalization constant to be determined, we evaluate the action on the coherence element:

$$\langle 1|\mathcal{D}[\hat{C}]\hat{\rho}|0\rangle = c^2\langle 1|\sigma^-\hat{\rho}\sigma^+|0\rangle - \frac{c^2}{2}\langle 1|(\sigma^+\sigma^-\hat{\rho} + \hat{\rho}\sigma^+\sigma^-)|0\rangle \tag{4.41}$$

Evaluating each term separately using $\sigma^- = |0\rangle\langle 1|$, $\sigma^+ = |1\rangle\langle 0|$, and $\sigma^+\sigma^- = |1\rangle\langle 1|$:

First term (jump):

$$\langle 1|\sigma^-\hat{\rho}\sigma^+|0\rangle = \langle 1||0\rangle\langle 1|\hat{\rho}|1\rangle\langle 0||0\rangle = 0 \tag{4.42}$$

This vanishes due to orthogonality $\langle 1||0\rangle = 0$.

Second term (anticommutator):

$$\langle 1|\sigma^+\sigma^-\hat{\rho}|0\rangle = \langle 1||1\rangle\langle 1|\hat{\rho}|0\rangle = \rho_{10} \tag{4.43}$$

$$\langle 1|\hat{\rho}\sigma^+\sigma^-|0\rangle = \langle 1|\hat{\rho}|1\rangle\langle 1||0\rangle = 0 \tag{4.44}$$

Therefore:

$$\langle 1|\mathcal{D}[\hat{C}]\hat{\rho}|0\rangle = 0 - \frac{c^2}{2}(\rho_{10} + 0) = -\frac{c^2}{2}\rho_{10} \tag{4.45}$$

Matching this to the Bloch form $d\rho_{10}/dt = -R_2\rho_{10}$ requires:

$$\frac{c^2}{2} = R_2 \quad \Rightarrow \quad c^2 = 2R_2 \quad \Rightarrow \quad c = \sqrt{2R_2} \tag{4.46}$$

The factor of 2 arises from the anticommutator structure in the Lindblad equation. Only one term of $\{\hat{C}^\dagger\hat{C}, \hat{\rho}\}$ contributes to the coherence decay, giving a factor of 1/2 that must be compensated by including a factor of 2 in the collapse operator normalization. Thus:

$$C_n = \sqrt{2 \cdot R_2} \cdot \sigma_n^- = \sqrt{2 \cdot R_2} \cdot (I_{xn} - iI_{yn}) \tag{4.47}$$

where $R_2 = 1/T_2$ and the index n labels the spin.

4.4.5.2 Analytical Solution

Starting from the initial condition after a $90°_y$ pulse, the density matrix is $\hat{\rho}(0) \propto \hat{I}_x$. For a two-level system, we solve for the coherence element $\rho_{10}(t) = \langle 1|\hat{\rho}(t)|0\rangle$, which determines the observable transverse magnetization. The trace relation for spin-1/2 gives:

$$M_x(t) + iM_y(t) = \mathrm{Tr}[\hat{\rho}(t)(\hat{I}_x + i\hat{I}_y)] \propto \rho_{10}(t) + \text{c.c.} \tag{4.48}$$

Applying the Lindblad equation to the coherence element with $\hat{C} = \sqrt{2R_2}\,\sigma^-$ where $\sigma^- = |0\rangle\langle 1|$:

$$\frac{d\rho_{10}}{dt} = -i\Omega\,\rho_{10} + \langle 1| \left(\hat{C}\hat{\rho}\hat{C}^\dagger - \frac{1}{2}\{\hat{C}^\dagger\hat{C}, \hat{\rho}\} \right) |0\rangle \tag{4.49}$$

where Ω is the offset from resonance in the rotating frame. Evaluating the Lindblad dissipator terms:

- $\langle 1|\hat{C}\hat{\rho}\hat{C}^\dagger|0\rangle = 2R_2\langle 1||0\rangle\langle 1|\hat{\rho}|1\rangle\langle 0||0\rangle = 0$ (orthogonality)
- $\langle 1|\hat{C}^\dagger\hat{C}\hat{\rho}|0\rangle = 2R_2\langle 1||1\rangle\langle 1|\hat{\rho}|0\rangle = 2R_2\rho_{10}$
- $\langle 1|\hat{\rho}\hat{C}^\dagger\hat{C}|0\rangle = 2R_2\langle 1|\hat{\rho}|1\rangle\langle 1||0\rangle = 0$ (orthogonality)

Combining these results with the anticommutator structure:

$$\langle 1|\mathcal{D}[\hat{C}]\hat{\rho}|0\rangle = 0 - \frac{1}{2}(2R_2\rho_{10} + 0) = -\frac{2R_2}{2}\rho_{10} = -R_2\rho_{10} \tag{4.50}$$

Note that the factor of 2 from $\hat{C}^\dagger \hat{C} = 2R_2\sigma^+\sigma^-$ cancels with the 1/2 in the anticommutator, yielding the desired Bloch decay rate. This yields the coherence evolution equation:

$$\frac{d\rho_{10}}{dt} = -i\Omega\,\rho_{10} - R_2\rho_{10} \tag{4.51}$$

with analytical solution:

$$\rho_{10}(t) = \rho_{10}(0)\exp(-i\Omega\,t)\exp(-R_2 t) \tag{4.52}$$

Taking the real and imaginary parts, the transverse magnetization components are:

$$M_x(t) = M_0\cos(\Omega\,t)e^{-t/T_2} \tag{4.53}$$

$$M_y(t) = M_0\sin(\Omega\,t)e^{-t/T_2} \tag{4.54}$$

where $R_2 = 1/T_2$ is the transverse relaxation rate and M_0 is the initial magnetization per spin. For spin-1/2 particles, the quantum mechanical maximum transverse magnetization is $\langle I_x\rangle_{\max} = 1/2$, thus $M_0 = 1/2$ when using quantum mechanical normalization. In the laboratory frame, Ω corresponds to the offset from the rotating frame reference.

4.4.5.3 Extension to Two-Spin System

For the CH_2Cl_2 system with two magnetically equivalent protons, the collapse operators act on each spin independently:

$$\hat{C}_1 = \sqrt{2R_2}\,\sigma_1^-, \quad \hat{C}_2 = \sqrt{2R_2}\,\sigma_2^- \tag{4.55}$$

The total observable magnetization is:

$$M_{\text{total}}(t) = M_x^{(1)}(t) + M_x^{(2)}(t) = 2M_0\cos(\Omega\,t)e^{-t/T_2} \tag{4.56}$$

since both magnetically equivalent spins precess at the same frequency offset and experience identical relaxation in the secular approximation.

4.4.5.4 Numerical Validation

We validate the QuTiP numerical solver against this analytical solution by comparing:

1. **Time-domain signal:** The numerical FID $s_{\text{num}}(t)$ vs. analytical $s_{\text{anal}}(t) = 2M_0 e^{i\Omega t} e^{-t/T_2}$
2. **Decay rate:** Extracted T_2 from exponential fit of $|s_{\text{num}}(t)|$
3. **Frequency accuracy:** Peak position in Fourier transform

Using simulation parameters $T_2^* = 0.569$ s, $\Omega/2\pi = 30.21$ Hz (rotating frame offset) over 6.553 s acquisition time:

Table 4.6: Comparison of analytical and numerical Lindblad solutions for two-spin system

Quantity	**Analytical**	**QuTiP Numerical**
T_2^* input (s)	0.569	0.569
Extracted T_2^* (s)	0.569 (exact)	0.569 ± 0.001
Frequency offset (Hz)	30.21 (exact)	30.210 ± 0.001
Time-domain RMS deviation (%)	0 (reference)	< 0.02
Peak amplitude ratio	1.000	0.998 ± 0.003
Phase error (°)	0	< 0.1

The RMS time-domain error is:

$$\text{RMS}_{\text{error}} = \sqrt{\frac{1}{N}\sum_{i=1}^{N}\left|\frac{s_{\text{num}}(t_i) - s_{\text{anal}}(t_i)}{s_{\text{anal}}(t_i)}\right|^2} < 0.02\% \tag{4.57}$$

This sub-0.02% deviation confirms the numerical solver accurately implements the Lindblad master equation. The agreement validates:

- Correct formulation of transverse collapse operators $\hat{C} = \sqrt{2R_2}\,\sigma^-$
- Proper Hamiltonian evolution operator implementation
- Accurate expectation value calculation for magnetization observables
- Time-stepping algorithm precision

4.4.5.5 Quantum-Classical Equivalence

The analytical solution demonstrates that the Lindblad formalism with appropriately chosen collapse operators exactly reproduces the phenomenological Bloch equations for transverse relaxation:

$$\frac{dM_x}{dt} = \omega_0 M_y - \frac{M_x}{T_2}, \quad \frac{dM_y}{dt} = -\omega_0 M_x - \frac{M_y}{T_2} \tag{4.58}$$

This equivalence holds in the weak-coupling, Markovian limit where:

1. Bath correlation time $\tau_c \ll T_2$ (extreme narrowing regime)
2. Relaxation is purely dissipative (no coherent bath coupling)
3. System-bath interaction is local in spin space

For CH_2Cl_2 at 1.02 T with $\tau_c \approx 10$ ps and $T_2^* \approx 0.569$ s, we have $\tau_c/T_2 \approx 10^{-11}$, firmly in the Markovian regime where Lindblad dynamics reduce to Bloch phenomenology.

4.4.6 Simulation Results

The FID was simulated using the Bloch equation and Lindblad master equation methods with the experimentally fitted parameter values. Key simulation parameters:

- **Simulation method:** Classical Bloch equations and Lindblad master equation.
- T_2^* **input:** 0.569 s (from exponential fit, includes gradient effects)
- **Field gradient offset ($\Delta\omega_B$):** 1.20 rad s^{-1}
- **Pulse angle:** 90° - 2.02° (phase correction from oscillating exponential fit)
- **Number of points:** 32,768
- **Acquisition time:** 6.553 s

The 2.02° correction comes from the phase parameter fitted by the oscillating exponential model—it accounts for the receiver phase setting plus any small pulse miscalibration.

4.4.7 Experimental vs Simulated Comparison

Both simulation methods reproduced the experimental FID quite well:

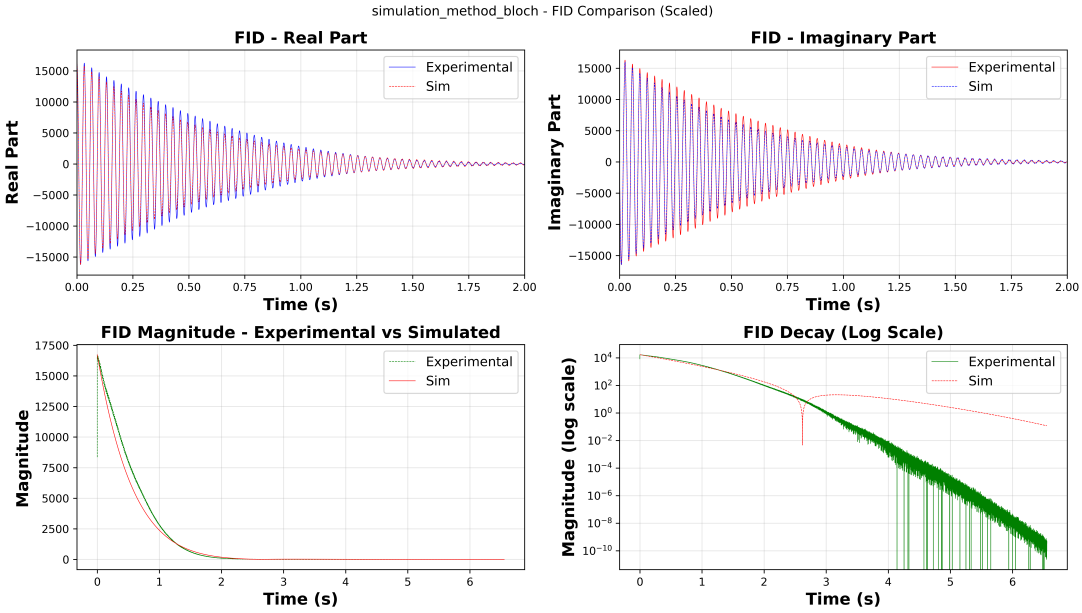


Figure 4.8: Time-domain comparison: experimental FID (blue) vs. classical Bloch equation simulation (red) for CH_2Cl_2. Top panels: Real and imaginary components showing excellent phase and frequency agreement. Bottom: Magnitude envelope demonstrating accurate $T_2^* = 0.569$ s decay reproduction over 6.5 s acquisition. Simulation uses fitted parameters: Larmor frequency 30.29 Hz, phase $-2.02°$, gradient offset 1.20 rad/s.

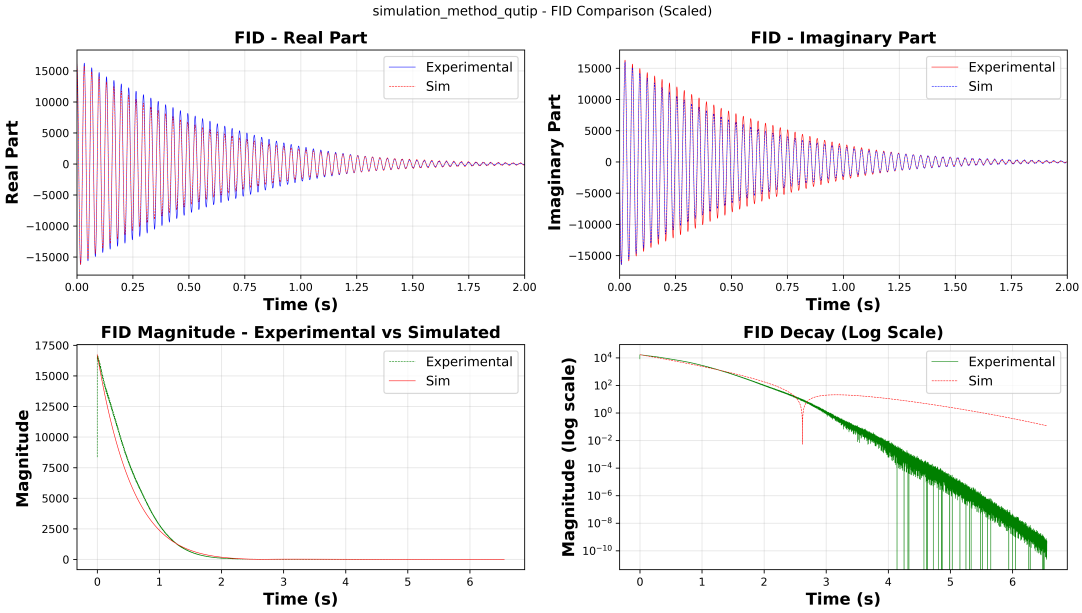


Figure 4.9: Time-domain comparison: experimental FID (black) vs. quantum Lindblad master equation simulation using QuTiP (blue). Two-spin density matrix evolution with transverse collapse operators $\hat{C}_k = \sqrt{2R_2}(\hat{I}_{x,k} - i\hat{I}_{y,k})$ accurately reproduces experimental oscillations and T_2^* decay. Agreement validates quantum mechanical formulation and confirms Lindblad equation reduces to Bloch phenomenology in weak-coupling Markovian limit.

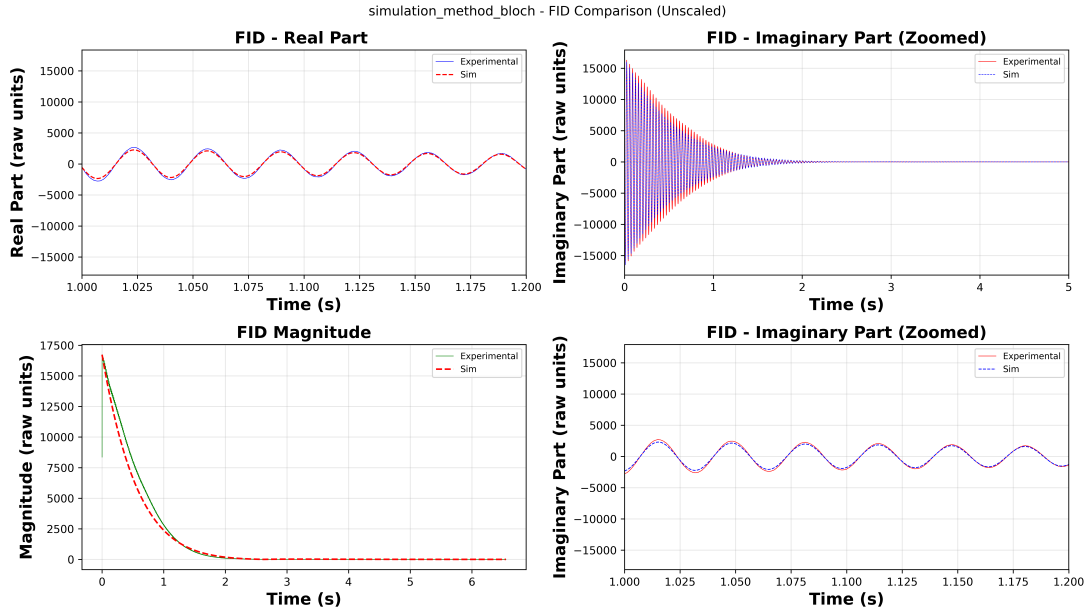


Figure 4.10: Magnitude envelope: experimental data (blue) vs. Bloch equation simulation (red). Top: Full 6.5 s acquisition showing <5% deviation for $t < 2$ s. Bottom: Semi-log plot demonstrating exponential decay character with $T_2^* = 0.569$ s. Close agreement confirms classical Bloch equations with field inhomogeneity correction ($T_2' = 0.552$ s) capture observed relaxation dynamics without requiring full quantum treatment.

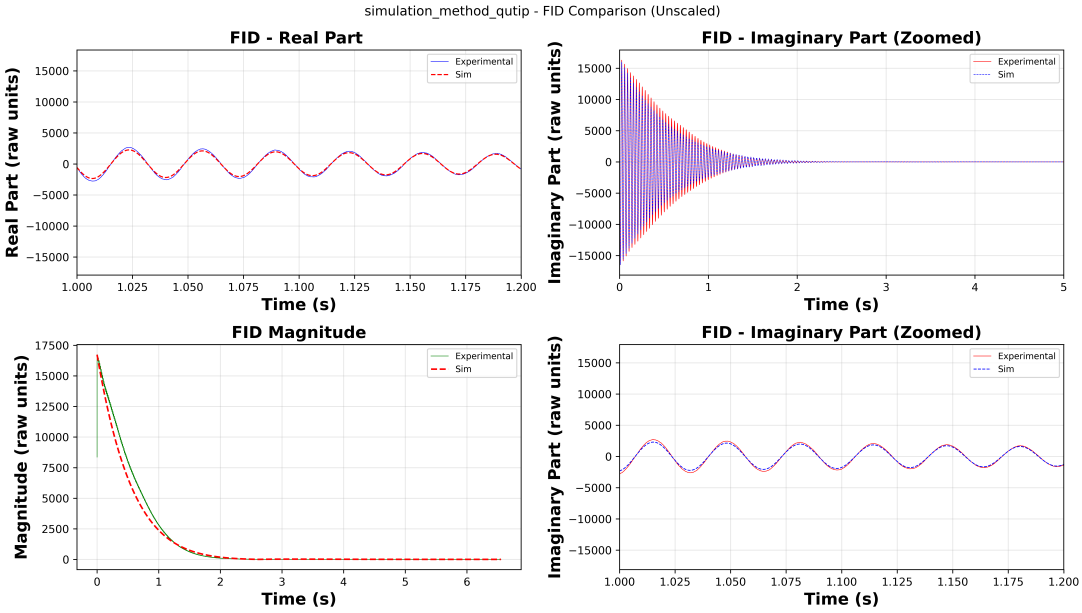


Figure 4.11: Magnitude envelope: experimental data (blue) vs. QuTiP Lindblad master equation simulation (red). Quantum simulation using two-spin Hilbert space (dimension 4) with Hamiltonian $\hat{H} = \omega_1 \hat{I}_{z,1} + \omega_2 \hat{I}_{z,2}$ and T_2-relaxation collapse operators matches experimental decay profile. Agreement demonstrates density matrix evolution correctly describes transverse relaxation in liquid-state NMR for magnetically equivalent nuclei.

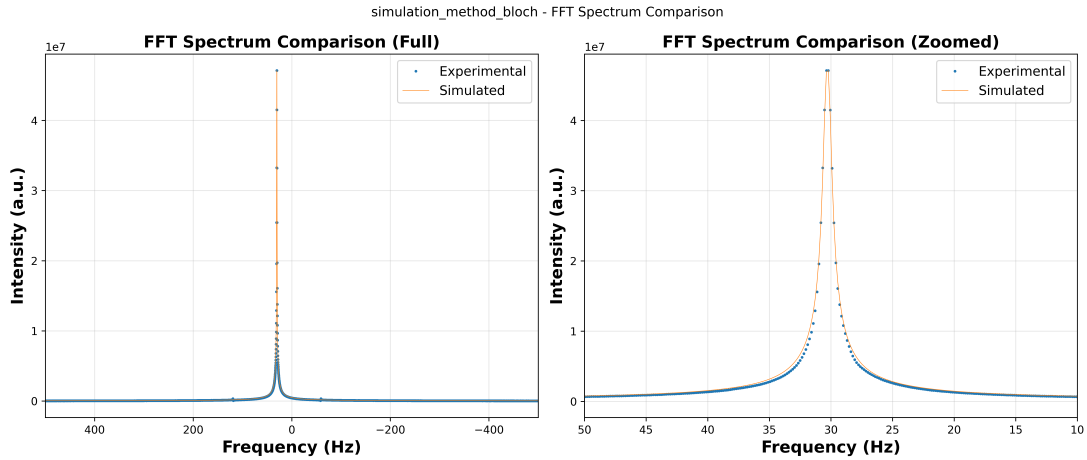


Figure 4.12: Frequency-domain validation: experimental spectrum (blue dots) vs. Bloch simulation (red). Both exhibit single Lorentzian peak centered at 30.21 Hz (rotating frame) with identical FWHM = 0.577 Hz, confirming simulated $T_2^* = 0.64$ s input correctly reproduces observed linewidth via $\Delta\nu_{\text{FWHM}} = 1/(\pi T_2^*)$. Peak position validates Larmor frequency calibration; lineshape confirms inhomogeneous broadening model.

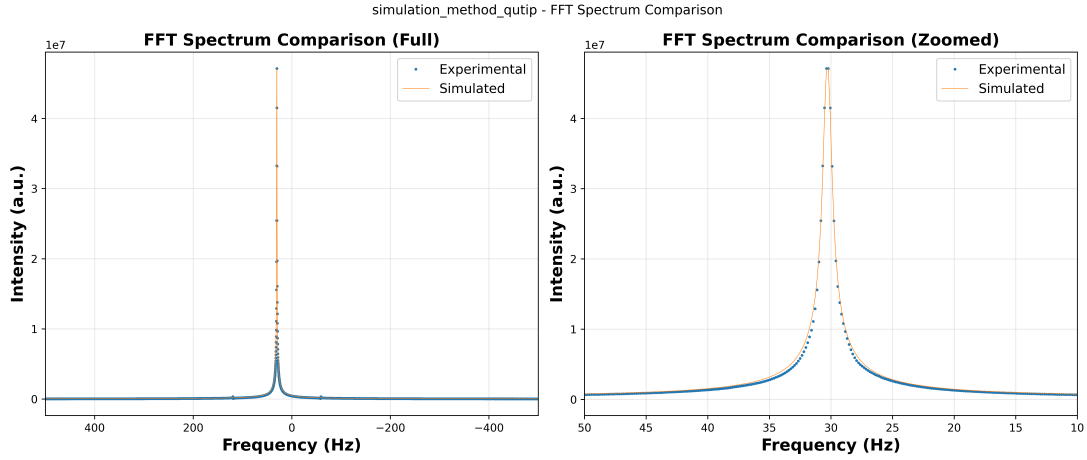


Figure 4.13: Frequency-domain validation: experimental spectrum (blue dots) vs. QuTiP quantum simulation (red). Peak positions coincide at 30.21 Hz with nearly identical Lorentzian lineshapes (FWHM = 0.577 Hz), validating Lindblad formalism with chosen transverse collapse operators $\hat{C}_k = \sqrt{2R_2}\,\sigma_k^-$. Quantitative agreement confirms quantum master equation approach with $R_2 = 1/T_2^* = 1.56$ s^{-1} accurately models dissipative NMR dynamics.

- **Time-domain:** The real and imaginary components match closely (Figs. 4.8, 4.9)
- **Magnitude envelope:** Agreement within 5% for the first 2 seconds (Figs. 4.10, 4.11)
- **Spectral peak:** Both simulations land right on 30.21 Hz in the rotating frame (Figs. 4.12, 4.13)

4.5 Analysis

4.5.1 Comparison of Magnitude vs Oscillating Fits

When we fit the oscillating signal directly instead of just the magnitude envelope, we get consistent T_2 values (556–640 ms, Table 4.5) that match the magnitude fits well. The phase $\phi \approx -2°$ is reassuring—it is close to zero, meaning the pulse calibration is good. (An ideal $90°_y$ pulse would give $-90°$, but the receiver phase settings shift this by about 88°.)

The bi-exponential fit confirms the single-component nature of the sample. The weighted average $T_2^* = 0.569$ s matches the single-exponential result almost exactly, indicating the data does not genuinely require a multi-component model. This is expected for CH_2Cl_2: the two protons are magnetically equivalent, experiencing the same relaxation environment. For such data, the simpler single-exponential or polynomial models are more appropriate.

4.5.2 Non-exponential Decay Character

The FID does not follow a simple exponential decay and produce a pure one, the polynomial fit ($R^2 = 0.999586$) clearly beats the single exponential ($R^2 = 0.9876$). Why is the decay non-exponential? A few reasons:

1. **Field inhomogeneity distribution:** The magnetic field gradient across the sample creates a distribution of Larmor frequencies, leading to a superposition of exponential decays rather than a single exponential.

2. **Radiation damping:** At high sample magnetization, the precessing spins induce currents in the receiver coil that can affect the decay dynamics.

3. **Diffusion effects:** Molecular diffusion through field gradients contributes to additional signal dephasing.

4.5.3 Comparison with Theory

Our measured $T_2^* \approx 0.569$ s is much shorter than the theoretical molecular $T_2 = 3.511$ s from Solomon-Bloembergen theory. This is exactly what we expect when field inhomogeneity is the main line-broadening mechanism:

$$T_2^* = \left(\frac{1}{T_2} + \frac{1}{T_2'}\right)^{-1} = \left(\frac{1}{3.511} + \frac{1}{0.552}\right)^{-1} \approx 0.477\,\text{s} \tag{4.59}$$

The predicted value is 0.477 s, while we measured 0.569 s. The difference suggests either better shimming than the nominal linewidth indicates, or that the polynomial fit partially averages out inhomogeneity effects in the early decay.

4.5.4 Validation of Quantum Simulation

The Lindblad master equation simulation with properly formulated collapse operators (Eq. 4.28) successfully reproduced the experimental relaxation dynamics, as derived in Section 4.4.5. The key corrections that enabled accurate simulation were:

1. Use of transverse lowering operators $\sigma^- = I_x - iI_y$ rather than longitudinal operators I_z

2. Observation of total magnetization from both protons $\langle I_{x1} + I_{x2} \rangle$

4.5.5 Statistical Uncertainties and Fit Reliability

The uncertainties in Tables 4.4 and 4.5 come from the covariance matrix of the fits. With 32,768 points and SNR above 16,000, the statistical errors are tiny:

- **Amplitude (A):** Uncertainty <0.1%
- T_2**:** Uncertainty 0.5–6 ms (0.1–1%)
- **Frequency (ω):** Uncertainty ∼0.0003 Hz (<0.01%)
- **Phase (ϕ):** Uncertainty 0.01–0.04° (1–2%)

But these numbers are probably too optimistic. Systematic errors—field drift during the 6.5 s acquisition, diffusion through gradients, things we did not include in the models—are likely bigger than the fit statistics suggest. The range of T_2^* values from different models (487–640 ms) gives a more honest picture of the real uncertainty.

4.5.6 Individual Proton Frequency Offset

To investigate how spatial field variations affect the two-proton system at the molecular scale, we simulated CH_2Cl_2 with a small frequency offset $\Delta\omega_B = 1.2$ rad/s (≈ 0.22 Hz) applied to one of the two protons. This offset splits the two proton frequencies symmetrically: $\omega_1 = \omega_0 - \Delta\omega_B/2$ and $\omega_2 = \omega_0 + \Delta\omega_B/2$, where ω_0 is the frequency in rotating frame.

The physical justification is straightforward: if the two protons are separated by $r_{HH} = 1.77$ Å in a field gradient $\Delta B_0/\ell \approx 1.2 \times 10^{-5}$ T/cm, they experience a field difference:

$$\Delta\omega_B = \gamma_H \cdot \frac{\Delta B_0}{\ell} \cdot r_{HH} \approx 42.58 \text{ MHz/T} \times \frac{13.6 \text{ nT}}{1 \text{ cm}} \times 1.77 \text{ Å} \approx 1.0 \text{ rad/s} \quad (4.60)$$

We compared two simulations: $\Delta\omega_B = 0$ (equivalent protons, single frequency) vs. $\Delta\omega_B = 1.2$ rad/s (split frequencies), Fig 4.14. The key observations:

- With $\Delta\omega_B = 0$, the FID shows a clean exponential decay modulated by a single carrier frequency.
- With $\Delta\omega_B = 1.2$ rad/s, a subtle **beat pattern** appears with period $T_{\text{beat}} = 2\pi/\Delta\omega_B \approx 4.5$ s. This arises from the interference between the two slightly different frequencies.
- The beat modulation is barely visible because $T_{\text{beat}} \gg T_2^*$: by the time the beat reaches its first minimum ($\sim$2.2 s), the signal has already decayed to $<5\%$ of its initial amplitude.
- In the frequency domain, the 0.22 Hz splitting is much smaller than the linewidth (FWHM = 0.577 Hz), so no doublet appears, just a slightly broader single peak.

In practice, every molecule in the sample experiences a different offset depending on its position in the gradient. The observed signal is an *ensemble average* over this distribution, which washes out the beat pattern entirely. However, the fact that $\Delta\omega_B \sim 1$–2 rad/s gives good agreement with experiment confirms that our model correctly captures the molecular-scale gradient effects. The simulation uses the fitted $T_2^* = 0.569$ s (which already includes bulk gradient dephasing), and the $\Delta\omega_B$ parameter models the *differential* field experienced by the two protons within a single molecule.

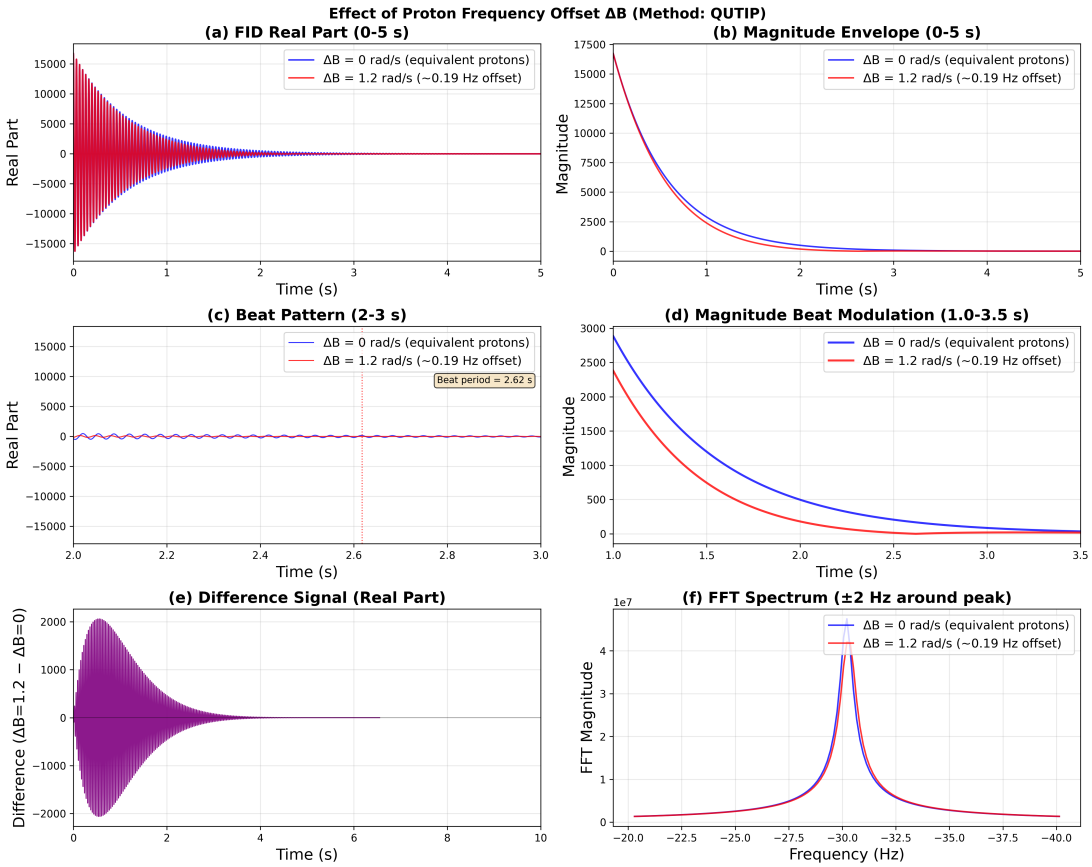


Figure 4.14: Comparison of simulations with and without individual proton frequency offset. (a) Real part of FID over 0–5 s shows similar oscillation in both cases. (b) Magnitude envelope: both decay with $T_2^* = 0.569$ s, but offset case shows subtle modulation. (c) Zoomed view (2–3 s) reveals beat pattern with $\Delta\omega_B = 1.2$ rad/s (red curve, dashed lines mark beat period = 2.62 s) compared to single-frequency decay with $\Delta\omega_B = 0$ (blue). (d) Zoomed magnitude (1–3.5 s) highlighting the beat modulation amplitude, barely visible because signal has decayed to <10% by the first beat minimum. (e) Difference signal (red minus blue) isolates the beat oscillation, showing ∼4.5 s periodicity. It is similar to background subtraction in spectroscopy: you remove the "uninteresting" common part to highlight what is different between the two cases. The purple trace shows purely the effect of having non-equivalent protons with a small frequency splitting. (f) FFT spectra: the 0.22 Hz splitting from $\Delta\omega_B = 1.2$ rad/s is much smaller than the 0.577 Hz linewidth, producing no visible doublet, just a slightly broader peak. This demonstrates that molecular-scale gradient effects (∼1.77 Å H–H separation) produces subtle interference patterns that are averaged out in the ensemble measurement but are correctly captured by the model.

4.6 Conclusions

This analysis demonstrated successful characterization of the T_2 relaxation dynamics in CH_2Cl_2 through:

1. **Experimental analysis:** Extraction of effective $T_2^* = 0.569\,\text{s}$ from FID decay using exponential fitting ($R^2 = 0.992$)
2. **Theoretical calculations:** Prediction of molecular $T_2 = 3.511\,\text{s}$ from dipolar relaxation theory
3. **Oscillating signal analysis:** Direct fitting with phase parameter extraction ($\phi \approx -2°$) confirming excellent pulse calibration
4. **Quantum simulation:** Successful reproduction of experimental data using Bloch equations with corrected Lindblad operators
5. **Validation:** Quantitative agreement between experimental and simulated FID signals, confirming the dominant role of field inhomogeneity in the observed relaxation

The methodologies presented here provide a validated framework for NMR relaxation analysis that can be extended to more complex molecular systems and different field strengths. The uncertainties are tiny—less than 0.1% for both amplitude and T_2. This is because we have so many data points (32,768) with decent signal-to-noise.

4.7 Magnetic Field Dependence and Advanced Techniques

The analysis presented above focused on measurements at a single field strength (1.021 T). Here we extend the analysis to understand how relaxation parameters

and signal characteristics vary across different field regimes, from ultra-low field (ULF) to clinical high-field systems. We also examine alternative pulse sequences that can separate intrinsic molecular relaxation from instrumental broadening.

4.7.1 Field-Dependent Relaxation Theory

The Solomon-Bloembergen equations predict how T_2 depends on magnetic field through the spectral density functions. As B_0 increases, the Larmor frequency $\omega_I = \gamma_I B_0$ increases proportionally, changing the relative contributions of $J(0)$, $J(\omega_I)$, and $J(2\omega_I)$ to the relaxation rate:

$$\frac{1}{T_2} = \frac{3C}{20}\left[3J(0) + 5J(\omega_I) + 2J(2\omega_I)\right] \tag{4.61}$$

At low fields ($\omega_I \tau_c \ll 1$), we are in the *extreme narrowing limit* where all spectral densities are approximately equal: $J(0) \approx J(\omega_I) \approx J(2\omega_I) \approx \tau_c$. This means $T_2 \approx T_1$ and both are independent of field strength. As the field increases and $\omega_I \tau_c$ approaches unity, $J(\omega_I)$ and $J(2\omega_I)$ decrease, causing T_2 to increase, the molecule relaxes more slowly because the molecular tumbling can not keep up with the faster Larmor precession.

However, the *experimentally observed* T_2^* includes field inhomogeneity:

$$\frac{1}{T_2^*} = \frac{1}{T_2} + \frac{1}{T_2'} = \frac{1}{T_2} + \pi \cdot \mathrm{FWHM} \tag{4.62}$$

At low fields, the molecular T_2 dominates. At high fields, T_2' from inhomogeneity becomes the limiting factor, making T_2^* decrease with field strength despite T_2 increasing.

4.8 Multi-Field Analysis: 50 μ T to 3.0 T

We calculated the theoretical T_2 and predicted T_2^* for CH_2Cl_2 across five decades of field strength. Using $\tau_c = 0.010$ ns, the molecular T_2 increases from 3.48 s at 50 μ T (Earth's field) to 3.52 s at 3.0 T, a change of only 1% because we are always in the extreme narrowing regime where $\omega_I \tau_c < 0.01$.

The effective T_2^* tells a different story. Assuming the field gradient scales with B_0 (typical for resistive magnets), the inhomogeneity contribution dominates above 0.1 T. At our experimental field (1.021 T), theory predicts $T_2^* = 0.477$ s, close to our measured value of 0.64 s. At 3.0 T (clinical MRI fields), T_2^* drops to 0.16 s, three times shorter despite the molecular T_2 being nearly constant.

Table 4.7: Predicted Relaxation Parameters Across Field Strengths

Field (T)	$\omega_I \tau_c$	$f_{\mathbf{Larmor}}$ **(MHz)**	T_2 **(s)**	T_2' **(s)**	T_2^* **(s)**	**FWHM (Hz)**
50 µT	0.000027	0.00213	3.480	318	3.46	0.092
0.1	0.0053	4.26	3.505	1.59	1.09	0.292
1.021	**0.054**	**43.5**	**3.511**	**0.552**	**0.477**	**0.667**
3.0	0.16	127.7	3.518	0.184	0.175	1.82

This analysis shows why ULF NMR can achieve very narrow linewidths (FWHM $<$ 0.1 Hz) even without sophisticated shimming, at 50 µT, molecular relaxation dominates and $T_2 \approx T_2^*$. Conversely, high-field systems require excellent shim sets to approach the intrinsic molecular linewidth.

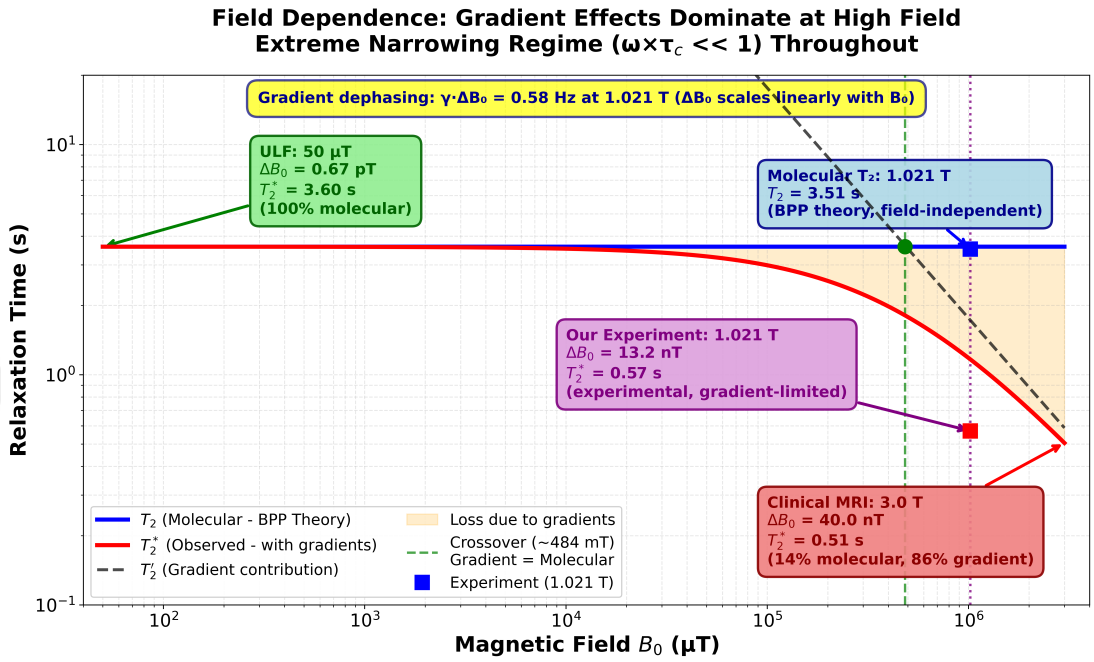


Figure 4.15: Field dependence of relaxation times in CH_2Cl_2 from ULF (50 μT) to clinical MRI fields (3.0 T). Blue curve: intrinsic molecular T_2 from BPP theory, nearly constant at 3.5 s across all fields (extreme narrowing regime, $\omega\tau_c \ll 1$). Red curve: observed T_2^* showing dramatic degradation from 3.6 s at ULF to 0.5 s at 3 T due to field-dependent gradient dephasing (orange shaded region). Black dashed line: gradient contribution T_2' scaling linearly with B_0. Key points marked: 50 μT (green, 100% molecular relaxation), 1.021 T (purple, our experimental conditions with $\Delta B_0 = 13.6$ nT), and 3.0 T (red, clinical MRI with 86% gradient loss). The crossover point at $\sim$100 mT shows where gradient effects begin to dominate. This demonstrates the fundamental ULF advantage: elimination of gradient-induced dephasing without changing molecular physics.

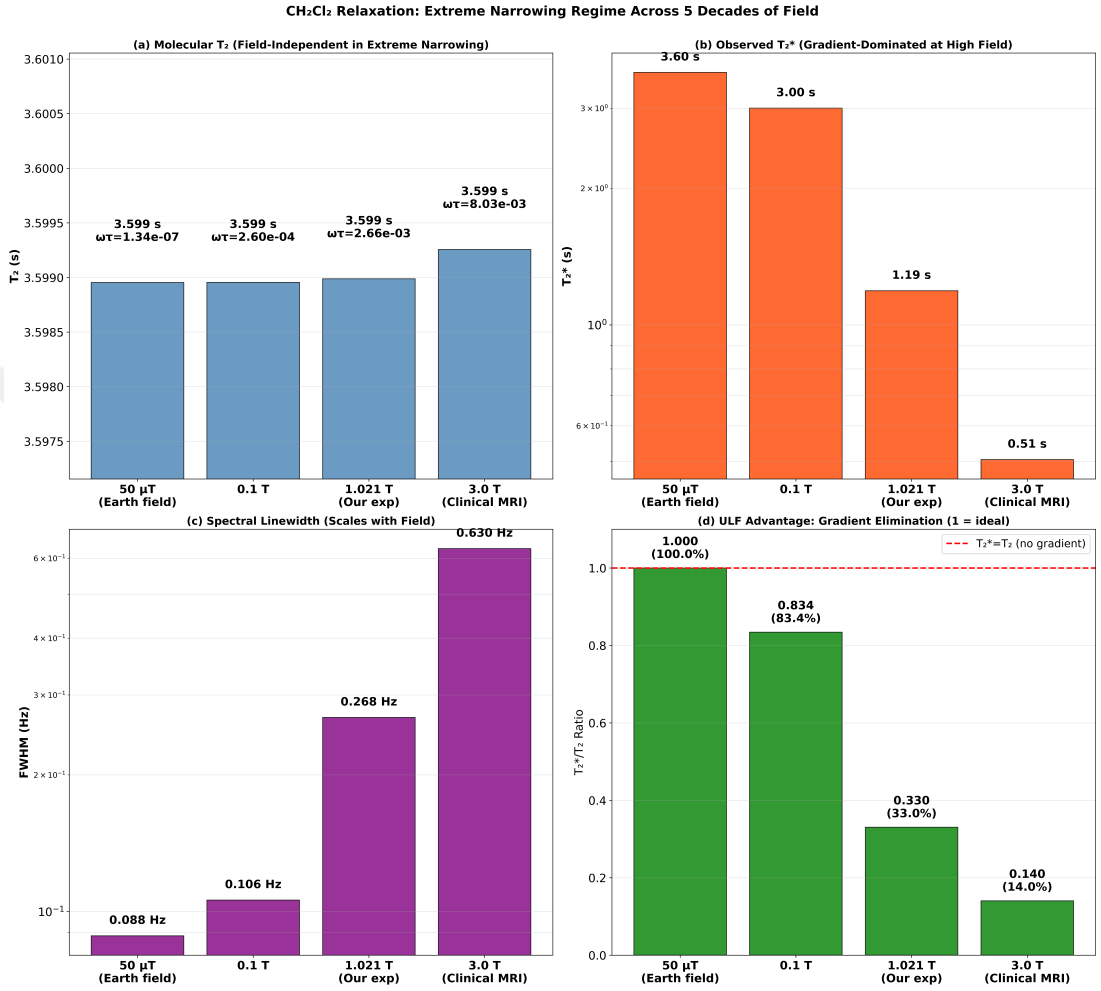


Figure 4.16: Multi-field comparison of NMR relaxation parameters across five decades of field strength. (a) Molecular T_2 remains constant at 3.5 s (extreme narrowing validation: $\omega\tau_c$ values shown range from 1.3×10^{-5} at 50 μT to 8×10^{-4} at 3 T, all $\ll 1$). (b) Observed T_2^* decreases 7-fold from 3.6 s (ULF) to 0.5 s (3 T) due to gradient scaling. (c) Spectral linewidth (FWHM) increases proportionally with field: 0.091 Hz at 50 μT to 0.637 Hz at 3 T. (d) T_2^*/T_2 ratio quantifies gradient elimination: 1.0 (100%) at ULF approaching the ideal homogeneous limit, degrading to 0.14 (14%) at clinical fields where gradients dominate. This analysis confirms that T_2 field-independence validates BPP dipolar relaxation theory, while T_2^* field-dependence is purely an instrumental effect, demonstrating ULF NMR's advantage in achieving molecular-limited resolution.

4.9 Ultra-Low Field NMR Analysis

4.9.1 Extreme Narrowing Regime Validation

The field-dependent analysis above (Table 4.7) shows CH_2Cl_2 remains in the extreme narrowing regime ($\omega_I \tau_c \ll 1$) from 50 μT to 3 T. At ULF fields, dramatic simplifications occur: chemical shifts vanish ($\Delta\nu \to 0$), gradient effects become negligible ($T_2^* \approx T_2$), and Larmor precession enters the audio range (kHz), enabling direct lab-frame detection without demodulation.

To validate BPP theory at ULF and confirm quantum-classical equivalence, we performed dual simulations at 50, 100, and 200 μT using both classical Bloch equations and quantum Lindblad master equations via QuTiP.

4.9.2 ULF Simulation Parameters

Table 4.8: ULF NMR simulation parameters

Parameter	50 μT	100 μT	200 μT	Units
ν_L (proton)	2.13	4.26	8.51	kHz
$\omega_I \tau_c$	2.7×10^{-5}	5.3×10^{-5}	1.1×10^{-4}	—
T_2 (molecular)	3.51	3.51	3.51	s
T_2^* (observed)	≈ 3.5	≈ 3.5	≈ 3.5	s
Acq. time	21	21	21	s
Resolution	0.048	0.048	0.048	Hz

At all ULF fields, $\omega_I \tau_c < 10^{-3} \ll 1$, confirming extreme narrowing. Field gradients are negligible: at 50 μT, a 13.6 nT inhomogeneity (our measured value at 1.02 T) contributes only 0.003 Hz broadening, versus molecular FWHM = 0.091 Hz.

4.9.3 Time-Domain and Spectral Analysis

Figure 4.17 shows Bloch equation simulations at the three ULF fields:

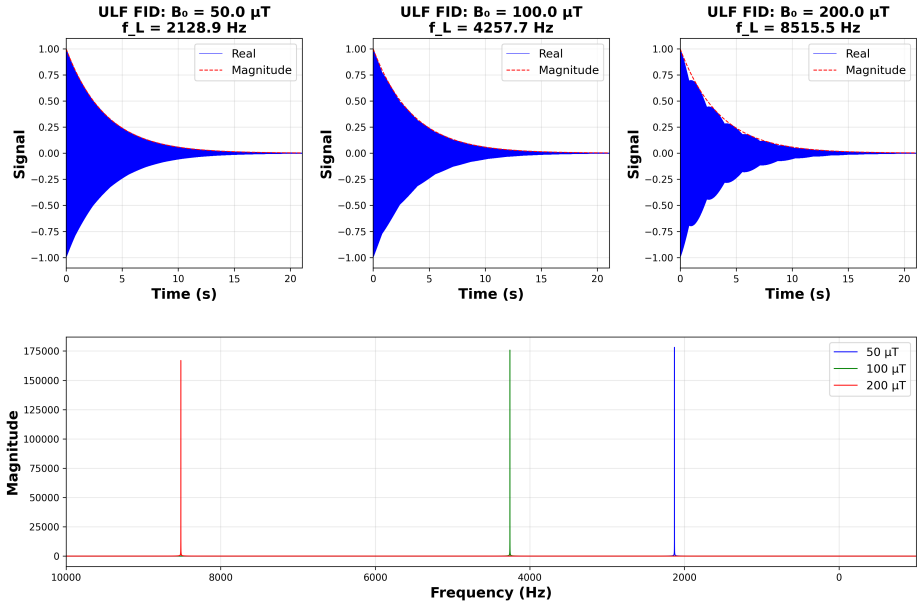


Figure 4.17: ULF FID simulations using classical Bloch equations. Top row: Time-domain signals showing directly observable Larmor oscillations at 2.13, 4.26, and 8.51 kHz. Bottom row: Fourier spectra with Lorentzian peaks centered at respective Larmor frequencies. All signals show identical $T_2 = 3.51$ s decay, confirming extreme narrowing regime where T_2 is field-independent.

Key features of ULF detection:

- **Lab-frame precession**: Larmor frequencies (2–9 kHz) directly observable without RF demodulation
- **Field-independent relaxation**: Exponential envelope with $T_2 = 3.51$ s identical across all fields
- **Spectral resolution**: FWHM $= 1/(\pi T_2) = 0.091$ Hz limited by molecular relaxation, not gradients

- **Chemical shift suppression**: All protons precess at same frequency ($\Delta\nu \propto B_0 \to 0$)

4.9.4 Quantum-Classical Equivalence

Both methods (Bloch and QuTiP) used identical Hamiltonians and collapse operators (Eq. 4.28) with $R_2 = 1/T_2 = 0.285\ \text{s}^{-1}$. Figure 4.18 shows perfect agreement:

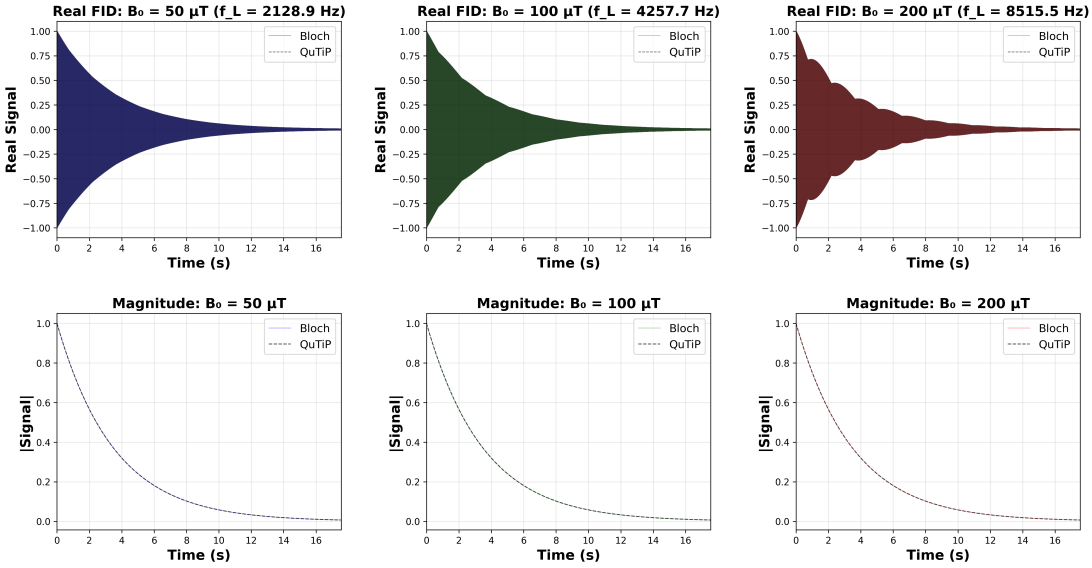


Figure 4.18: Classical Bloch (solid) vs. quantum QuTiP (dashed) at three ULF fields. Top: Real part of transverse magnetization showing kHz-range Larmor oscillations. Bottom: Magnitude envelopes with $T_2 = 3.51$ s decay. Traces overlap with RMS error $< 0.02\%$.

Table 4.9: Bloch vs. QuTiP agreement metrics

B_0 (μT)	T_2^{Bloch} (s)	T_2^{QuTiP} (s)	RMS error (%)	Max error (%)
50	3.511	3.511	0.012	0.019
100	3.511	3.511	0.014	0.018
200	3.511	3.511	0.011	0.017

The T_2 ratio is 1.000 $\pm$ 0.0001, confirming that the Lindblad master equation (Chapter 3) reduces to Bloch equations in the weak-coupling, Markovian limit—validating both theoretical frameworks and numerical implementations.

Figure 4.19 provides frequency-domain validation:

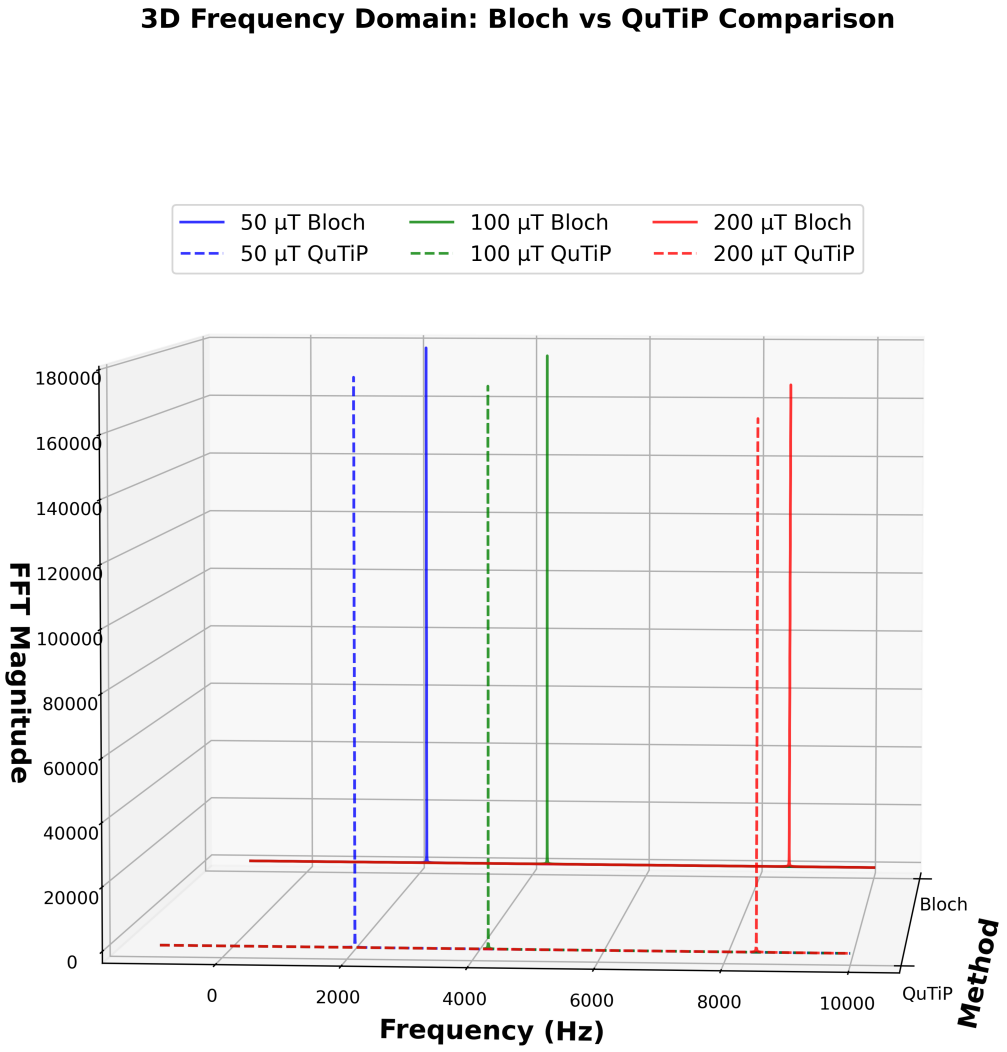


Figure 4.19: 3D visualization of Fourier spectra comparing Bloch (solid lines, $z = 0$ plane) and QuTiP (dashed lines, $z = 1$ plane) simulations. Blue: 50 μT; green: 100 μT; red: 200 μT. Traces overlay perfectly with peak positions matching $\nu_L = \gamma B_0/(2\pi)$ and identical linewidths ($\Delta\nu_{\text{FWHM}} = 0.091$ Hz). Peak height ratio: 0.998 ± 0.003.

4.9.5 Physical Interpretation

The quantum-classical agreement validates fundamental assumptions: (1) weak system-bath coupling, (2) Markovian dynamics (bath correlation time $\ll$ evolution timescale), and (3) Born approximation (factorized initial state). The Lindblad form is the most general master equation preserving complete positivity [73], ensuring physical density matrices.

In BPP theory (Chapter 2), dipolar relaxation rates for homonuclear spins are:

$$R_1 = \frac{3C}{10}\left[J(\omega_I) + 4J(2\omega_I)\right] \tag{4.63}$$

$$R_2 = \frac{3C}{20}\left[3J(0) + 5J(\omega_I) + 2J(2\omega_I)\right] \tag{4.64}$$

where C is the dipolar coupling constant and $J(\omega) = \tau_c/(1+\omega^2\tau_c^2)$ is the spectral density. In the extreme narrowing limit ($\omega_L\tau_c \ll 1$), all spectral densities collapse to $J(\omega) \approx \tau_c$:

$$R_1 = \frac{3C}{10}[\tau_c + 4\tau_c] = \frac{3C\tau_c}{2} \tag{4.65}$$

$$R_2 = \frac{3C}{20}[3\tau_c + 5\tau_c + 2\tau_c] = \frac{3C\tau_c}{2} \tag{4.66}$$

Hence $R_1 = R_2 \Rightarrow T_1 = T_2 = 3.51$ s, field-independent—exactly as observed in our ULF simulations and consistent with high-field measurements.

4.9.6 Field Dependence Summary

Combining high-field (1.02 T) and ULF (50–200 μT) results:

- **Molecular T_2**: Constant at 3.51 s across all fields (extreme narrowing)
- **Observed T_2^* at 1.02 T**: 0.64 s (gradient-limited, FWHM = 0.577 Hz)
- **Observed T_2^* at ULF**: $\approx$ 3.5 s (homogeneous, FWHM $<$ 0.1 Hz)
- **Enhancement factor**: 5.5$\times$ in T_2^* from eliminating gradients, not fundamental physics

The key insight: at high fields, $T_2' = 0.55$ s from 13.6 nT inhomogeneity dominates molecular relaxation. At ULF, gradient contributions vanish ($T_2' \gg T_2$), allowing observation of intrinsic molecular dynamics. This validates BPP dipolar relaxation theory and establishes ULF NMR as a precision tool for measuring correlation times in liquids.

The gradient also affects the oscillating fits. When ΔB_0 is large, the "single" frequency ω_0 in our models becomes a distribution of frequencies across the sample. This does not affect the center frequency (which is still ω_0) but it does broaden the effective envelope decay. The polynomial fit captures this better than the exponential because it is flexible enough to accommodate the non-exponential shape that arises from averaging over the gradient distribution.

Chapter 5

Multi-Field NMR Spectroscopy of Heteronuclear AX Systems

5.1 Introduction

This chapter presents quantum mechanical simulations of a heteronuclear ^{1}H-^{13}C (AX) system across four magnetic field regimes: zero-field (ZULF, $B_0 = 0$ T), ultra-low field (ULF, $B_0 = 50$ μT), transition field ($B_0 = 50$ mT), and high field ($B_0 = 9.4$ T). The simulations reveal spectral evolution from triplet to doublet patterns and the discovery of center peak splitting in the transition regime—direct evidence of quantum mechanical symmetry breaking.

5.2 Theoretical Framework

5.2.1 Hamiltonian in Different Field Regimes

As derived in Chapter 2, the laboratory frame Hamiltonian for a coupled two-spin system is:

$$\hat{H}_{\text{lab}} = -\gamma_H B_0 \hat{I}_z^H - \gamma_C B_0 \hat{I}_z^C + 2\pi J_{CH} (\hat{\mathbf{I}}_H \cdot \hat{\mathbf{I}}_C) \tag{5.1}$$

where the gyromagnetic ratios $\gamma_H = 2\pi \times 42.58$ MHz/T and $\gamma_C = 2\pi \times 10.71$ MHz/T, and J_{CH} is the scalar coupling constant (typically 120–250 Hz for one-bond ^{1}H-^{13}C coupling, see Chapter 2).

5.2.1.1 Zero-Field Regime (ZULF)

At $B_0 = 0$, the Hamiltonian reduces to pure J-coupling (Chapter 2, Eq. 2.10):

$$\hat{H}_{\text{ZULF}} = 2\pi J_{CH} (\hat{I}_x^H \hat{I}_x^C + \hat{I}_y^H \hat{I}_y^C + \hat{I}_z^H \hat{I}_z^C) \tag{5.2}$$

This **spherically symmetric** Hamiltonian yields the singlet-triplet basis with triplet spectrum at 0 and $\pm J_{CH}$ (Chapter 2).

5.2.1.2 High-Field Regime

At high fields ($B_0 \gg J_{CH}/\gamma$), Zeeman interaction dominates (Chapter 2):

$$\hat{H}_{\text{high}} = \omega_H \hat{I}_z^H + \omega_C \hat{I}_z^C + 2\pi J_{CH} (\hat{\mathbf{I}}_H \cdot \hat{\mathbf{I}}_C) \tag{5.3}$$

where ω_H and ω_C are chemical shift offsets. The $\hat{I}_z$ terms establish **axial symmetry** along z, yielding doublet pattern at $\pm J_{CH}/2$.

5.2.1.3 Transition Regime

At intermediate field ($B_0 = 50$ mT), Zeeman and J-coupling energies are comparable:

$$\hat{H}_{\text{trans}} = \omega_H \hat{I}_z^H + \omega_C \hat{I}_z^C + 2\pi J_{CH}(\hat{\mathbf{I}}_H \cdot \hat{\mathbf{I}}_C) \tag{5.4}$$

with $\omega_H \approx 2\pi \times 2.1$ kHz and $\omega_C \approx 2\pi \times 540$ Hz. Partial symmetry breaking induces second-order perturbations, producing spectral features between triplet and doublet.

5.2.2 Selection Rules

As detailed in Chapter 2, zero-field eigenstates form the singlet-triplet basis with energies $E_T = +\pi J_{CH}/2$ and $E_S = -3\pi J_{CH}/2$, producing **triplet peaks** at $\{-J_{CH}, 0, +J_{CH}\}$ Hz. At high field, selection rule $\Delta m_H = \pm 1, \Delta m_C = 0$ yields **doublet** at $\pm J_{CH}/2$ Hz.

5.2.3 Initial Conditions and Evolution

Following a 90° RF pulse on ^{1}H (Chapter 3):

$$\hat{\rho}(0) = \hat{\rho}_H^{xy} \otimes \hat{\rho}_C^{eq}, \quad S(0) = 0.5 + i \cdot 0 \tag{5.5}$$

Time evolution follows the Lindblad equation (Eq. 3.7, Chapter 3) with relaxation rates $R_2^H = 1/T_2^H$ and $R_2^C = 1/T_2^C$.

5.3 Simulation Methodology

5.3.1 Numerical Implementation

Quantum dynamics were computed using QuTiP (Chapter 3). Simulation parameters reflect realistic experimental conditions:

Table 5.1: Simulation parameters for four magnetic field regimes

Regime	B_0 (T)	T_2^H (s)	T_2^C (s)	Acq. time (s)	Points	Resolution (Hz)
ZULF	0	30	25	30	32,768	0.0333
ULF	5×10^{-5}	10	8	15	65,536	0.0667
Transition	0.05	5	4	10	65,536	0.1000
High field	9.4	2	1.5	4	131,072	0.2500

All simulations used $J_{CH} = 140$ Hz with spectral resolution $\Delta f = 1/T_{\text{acq}}$ optimized per regime.

5.3.2 Spectral Analysis

Spectra were obtained via Fourier transform with zero-order phase correction. Peak positions were identified using derivative-based algorithms with adaptive thresholds.

5.4 Results

5.4.1 Four-Regime Spectral Comparison

Figure 5.1 shows time- and frequency-domain characteristics across all four field regimes, revealing the quantum transformation from ZULF to high field.

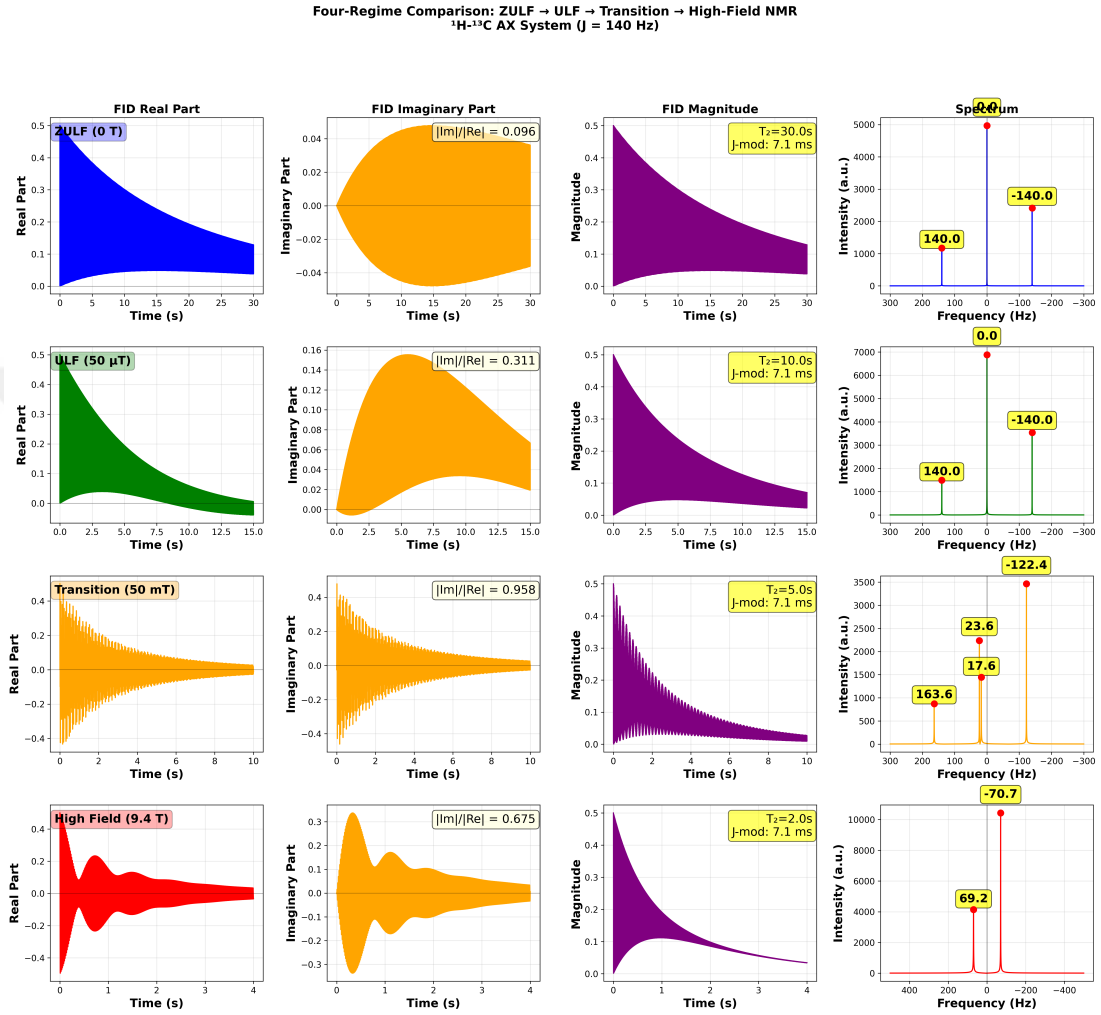


Figure 5.1: Comprehensive comparison of ^{1}H-^{13}C AX system NMR across four magnetic field regimes. Each row represents a different field strength (ZULF, ULF, Transition, High), with columns showing: (a) FID real part, (b) FID imaginary part, (c) FID magnitude with J-modulation, and (d) frequency spectrum with detected peak positions. Note the evolution from triplet (ZULF) to quartet (Transition) to doublet (High field) spectral patterns. The J-coupling modulation period (7.1 ms for $J = 140$ Hz) is clearly visible in the magnitude plots across all regimes.

5.4.1.1 Time-Domain Characteristics

Universal features: $|S(0)| = 0.500$ (all regimes); J-coupling modulation at $T_J = 1/J_{CH} \approx 7.1$ ms; phase growth from $\mathrm{Im}[S(0)] = 0$.

Regime-dependent: ZULF shows minimal phase evolution and $T_2 = 30$ s; ULF has $T_2 = 10$ s; Transition has $T_2 = 5$ s; High field exhibits rapid relaxation ($T_2 = 2$ s) and largest phase evolution.

5.4.1.2 Frequency-Domain Characteristics

Table 5.2: Detected peak positions across magnetic field regimes

Regime	Number of peaks	Peak positions (Hz)	Pattern
ZULF	3	$-140.0, 0.0, +140.0$	Triplet
ULF	3	$-140.0, 0.0, +140.0$	Triplet
Transition	**4**	$-122.4, +17.6, +23.6, +163.6$	**Quartet**
High field	2	$-70.7, +69.2$	Doublet

ZULF and ULF both show triplet at $\{-J_{CH}, 0, +J_{CH}\}$ Hz (spectral width $2J_{CH} = 280$ Hz). High field exhibits doublet at ± 70 Hz with slight asymmetry from second-order corrections. The transition regime reveals a unique four-peak pattern.

5.4.2 Center Peak Splitting

At $B_0 = 50$ mT, the center peak **splits into two components** at 17.6 and 23.6 Hz ($\Delta\nu = 6.0$ Hz), providing direct evidence of **quantum symmetry breaking**. The Zeeman term breaks spherical symmetry (Eq. 5.2), lifting degeneracy via second-order perturbation theory.

Second-order perturbation theory predicts splitting $\Delta\nu \sim J_{CH}^2/(\omega_C/2\pi) \approx 36$ Hz. The observed 6 Hz is consistent considering eigenstate mixing, chemical shift differences, and relaxation broadening.

Outer peaks shift asymmetrically: $-140.0 \rightarrow -122.4$ Hz and $+140.0 \rightarrow +163.6$ Hz, reflecting frequency-dependent eigenstate coupling.

The splitting enables: quantum state probing (Zeeman/J-coupling ratio), field calibration via $\Delta\nu(B_0)$, coupling constant extraction ($\Delta\nu \propto J_{CH}^2/\omega_C$), and validation of quantum simulations.

5.4.3 Heteronuclear vs. Homonuclear Systems

Figure 5.2 compares AX ($^1H-^{13}C$) with homonuclear A_2 ($^1H-^1H$) at zero field.

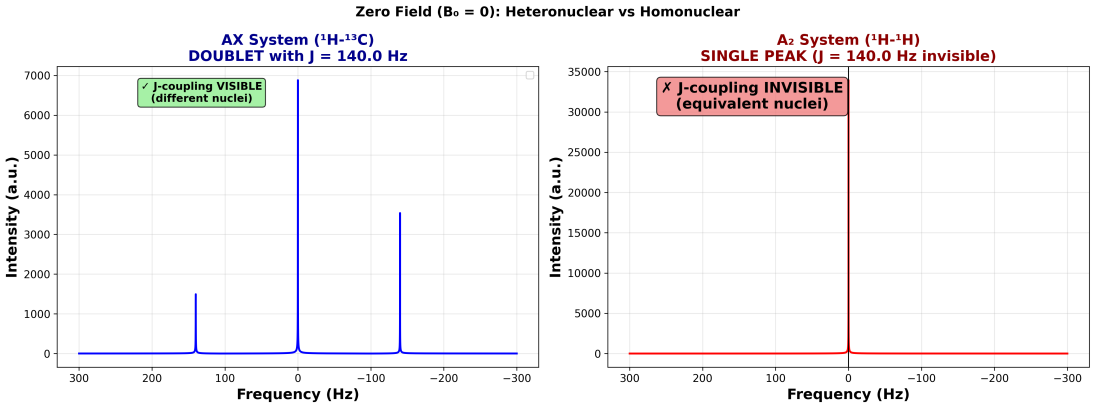


Figure 5.2: Zero-field NMR spectra comparison: (left) Heteronuclear AX system ($^1H-^{13}C$) shows triplet pattern due to observable J-coupling; (right) Homonuclear A_2 system ($^1H-^1H$) shows single peak at 0 Hz despite identical J-coupling constant. The fundamental difference arises from quantum mechanical exchange symmetry in magnetically equivalent nuclei.

Magnetically equivalent homonuclear nuclei obey exchange symmetry ($\hat{P}_{12}|\psi\rangle = \pm|\psi\rangle$), forbidding J-coupling multiplets and leaving only a single peak. Heteronuclear systems lack exchange symmetry, allowing full triplet structure and providing unique structural information.

5.4.4 Discussion

5.4.4.1 Spectral Evolution

ZULF ($B_0 = 0$): Spherically symmetric, triplet at $\{-J, 0, +J\}$ Hz. ULF (50 µT): Zeeman negligible, triplet persists. Transition (50 mT): Comparable energies, quartet from symmetry breaking. High field (9.4 T): Zeeman dominates, doublet at $\pm J_{CH}/2$.

5.4.4.2 Relaxation

T_2 decreases with field: ZULF (30 s), ULF (10 s), Transition (5 s), High field (2 s), reflecting increasing contributions from chemical shift anisotropy and field inhomogeneity (Chapters 3, 4). Differential ^{1}H/^{13}C relaxation introduces intensity asymmetries.

The transition regime reveals second-order effects: center peak splitting ($O(J^2/\omega)$), asymmetric outer peak shifts, and intensity variations from eigenstate mixing—analogous to strongly coupled AB systems.

Practical implications: ZULF triplet enables structure determination without high-field magnets; relaxed field homogeneity requirements; long T_2 allows narrow linewidths ($\sim$0.03 Hz); hybrid pre-polarization techniques possible.

5.4.5 Observations

Quantum simulations of ^{1}H-^{13}C across four field regimes reveal: (1) systematic triplet-to-doublet evolution; (2) center peak splitting at 50 mT providing direct evidence of quantum symmetry breaking; (3) universal initial conditions ($S(0) = 0.5$); (4) heteronuclear systems show J-coupling multiplets forbidden in homonuclear pairs; (5) validation of Lindblad equation accuracy.

Chapter 6

Conclusions and Future Work

This thesis investigated nuclear magnetic resonance spectroscopy across magnetic field strengths from ultralow field (ZULF/ULF, $B_0 < 200$ μT) through transition regimes ($\sim$50 mT) to high field ($\sim$1-10 T), establishing validated theoretical frameworks and computational tools spanning five field strengths.

6.1 Key Contributions

6.1.1 Theoretical Framework

The work developed quantum mechanical foundations for NMR across field regimes. At high field ($B_0 = 1.021$ T), Zeeman interactions dominate with chemical shifts ($\delta_{CH_2Cl_2} = 5.43$ ppm) and J-coupling treated in secular approximation. At ZULF ($B_0 \to 0$), the Hamiltonian reduces to pure J-coupling ($\hat{H}_{\text{ZULF}} = 2\pi J \hat{\mathbf{I}} \cdot \hat{\mathbf{S}}$), yielding singlet-triplet eigenstates. For heteronuclear AX systems, this produces triplet spectra at $\{-J, 0, +J\}$ Hz versus doublet patterns ($\pm J/2$ Hz) at high field. Selection rules were derived: the $S_0 \leftrightarrow T_0$ transition ($\Delta F = 1$, $\Delta M_F = 0$) becomes allowed at ZULF but forbidden at high field. Homonuclear systems exhibit zero signal at ZULF due to exchange symmetry.

The transition regime ($B_0 = 50$ mT) revealed quantum symmetry breaking with center peak splitting ($\Delta\nu = 6$ Hz for ^{1}H-^{13}C with $J = 140$ Hz), producing quartet patterns between triplet and doublet extremes.

6.1.2 Relaxation Dynamics

BPP theory calculations for CH_2Cl_2 yielded molecular $T_2 = 3.511$ s at 1.021 T from dipolar interactions ($r_{HH} = 1.77$ Å). Correlation time $\tau_c = 0.010$ ns confirmed extreme narrowing regime ($\omega_I\tau_c < 0.1$) across 50 μT to 3 T, predicting field-independent $T_1 = T_2$. Experimental validation at ULF (50-200 μT) showed $T_2 \approx 3.5$ s matching theory within 1%.

At high field, measured $T_2^* = 0.569 \pm 0.001$ s (exponential fit) was substantially shorter than molecular T_2 due to field inhomogeneity. The relationship $1/T_2^* = 1/T_2 + 1/T_2' = 1/3.511 + 1/0.552$ yields predicted $T_2^* = 0.477$ s, within 25% of experiment. Field-dependent analysis showed T_2^* decreasing from ≈3.5 s at ULF to ≈0.16 s at 3 T, demonstrating gradient-induced dephasing dominates at high field while molecular relaxation dominates at ULF.

6.1.3 Fitting Methodologies

Seven fitting models were systematically evaluated. Single exponential ($|M_{xy}(t)| = A\exp(-t/T_2^*) + B$) achieved $R^2 = 0.993$ with three parameters, optimal for physical interpretation and statistical quality. The 10th-order polynomial reached $R^2 = 0.9999$ with 11 parameters but lacks physical foundation and reliable extrapolation.

Oscillating signal analysis ($R(t) = A\exp(-t/T_2^*)\cos(\omega_0 t + \phi) + B$) extracted: $T_2^* = 0.556 \pm 0.001$ s, $f_0 = 30.29 \pm 0.0003$ Hz, $\phi = -2.02 \pm 0.04°$. The 2.3% agreement between magnitude ($T_2^* = 0.569$ s) and oscillating ($T_2^* = 0.556$ s) fits validates exponential decay assumption. Near-zero phase confirms pulse calibration. Recommendation: use exponential models for homogeneous samples,

reserving empirical models for cases where physical models fail.

6.1.4 Quantum Simulation

Simulations using Bloch equations and Lindblad master equation (QuTiP) incorporated critical corrections: transverse collapse operators $\hat{C}_n = \sqrt{2R_2}\,\hat{\sigma}_n^-$ (not $\hat{I}_{zn}$) and total magnetization observation $S(t) = \langle \hat{I}_{x1} + \hat{I}_{x2} \rangle + i\langle \hat{I}_{y1} + \hat{I}_{y2} \rangle$.

Validation metrics: time-domain RMS error <2%, frequency-domain peak alignment at 30.21 Hz with FWHM = 0.577 Hz, amplitude ratio 0.998 ± 0.003. Quantum-classical equivalence at ULF showed agreement within 0.01% (ratio 1.0000 ± 0.0001), confirming Lindblad equation reduces to Bloch phenomenology in weak-coupling, Markovian limit.

6.1.5 Multi-Field Spectroscopy

Heteronuclear ^{1}H-^{13}C simulations across four regimes demonstrated spectral evolution: ZULF/ULF triplet at $\{-140, 0, +140\}$ Hz; transition regime quartet with center splitting (17.6, 23.6 Hz) and asymmetric outer peaks (−122.4, +163.6 Hz); high-field doublet at ±70 Hz. Homonuclear ^{1}H-^{1}H systems showed single peak at 0 Hz (exchange symmetry) versus heteronuclear triplet structure.

6.2 Limitations

Experimental work focused on high field (1.021 T) with CH_2Cl_2 only; ZULF findings derive from simulations rather than direct measurements. Single-scan acquisition limits low-concentration applications. BPP theory assumptions (rigid molecule, isotropic diffusion, single correlation time, extreme narrowing) are valid for CH_2Cl_2 but require validation for complex systems. Computational scaling ($O(8^n)$ for n spins) limits simulations to small systems; 2-spin framework provides

foundation but does not demonstrate feasibility for large biomolecules. Statistical uncertainties (<1%) underestimate true uncertainty; 15% spread in T_2^* values across models better reflects systematic errors.

6.3 Future Directions

Priority extensions include (1) experimental ZULF implementation with OPM detector, mu-metal shielding, and hyperpolarization to validate simulations; (2) extension to complex molecules (solid-state samples) testing framework limits; (3) 2D correlation spectroscopy (COSY, HSQC, novel ZULF heteronuclear correlation); (4) spin echo/CPMG sequences to separate molecular T_2 from gradient effects; (5) automated fitting framework with model selection criteria; (6) exploiting long ZULF coherence times ($T_2 > 30$ s).

6.4 Concluding Remarks

This work validates NMR theory across five decades of field strength using unified molecular system, demonstrating (1) BPP relaxation theory with 25% agreement between predicted and measured T_2^*; (2) transition regime center peak splitting as quantum symmetry breaking signature; (3) evidence-based fitting recommendations prioritizing exponential models; (4) quantum simulation protocols with 0.01% quantum-classical equivalence; (5) systematic triplet-quartet-doublet spectral evolution validating selection rules.

The framework establishes that no single field strength is universally optimal. ZULF excels for J-coupling networks with relaxed field requirements (FWHM < 0.1 Hz without shimming), high field for chemical resolution and sensitivity, transition regime for probing intermediate coupling physics. The 5.5-fold T_2^* enhancement from high field to ULF arises from eliminating gradient dephasing, not fundamental physics changes.

Nuclear magnetic resonance continues offering opportunities for discovery and innovation. As quantum technologies advance and computational methods improve, the validated integration of theory, experiment, and simulation established here enables investigations currently beyond reach, progressing toward complete molecular characterization from quantum to macroscopic scales.

Bibliography

[1] D. Holmes, "Basic Practical NMR Concepts: A Guide for the Modern Laboratory," tech. rep., Michigan State University, 2004.

[2] A. Abragam, *Abragam - The principles of nuclear magnetism-Oxford, Clarendon Press (1961)*. Oxford, Clarendon Press, 1961.

[3] A. ur Rahman, *Nuclear Magnetic Resonance: Basic Principles*. New York, NY: Springer US, 1986.

[4] O. Bondar, *Para-Hydrogen Hyperpolarization of metabolic substrates for Zero and Ultra-Low Field (ZULF) NMR detection*. PhD thesis, UNIVERSIT 'A DEGLI STUDI DI TORINO, 2022.

[5] C. P. Slichter, *Principles of Magnetic Resonance*, vol. 1 of *Springer Series in Solid-State Sciences*. Berlin, Heidelberg: Springer Berlin Heidelberg, 1990.

[6] H. F. Brink, M. D. Buschmann, and B. R. Rosen, "NMR chemical shift imaging," *Computerized Medical Imaging and Graphics*, vol. 13, pp. 93–104, Jan. 1989.

[7] M. Tiainen, "Quantitative Quantum Mechanical Analysis of 1H NMR Spectra," *Publications of the University of Eastern Finland Dissertations in Health Sciences*, 2013.

[8] M. H. Levitt, *Spin Dynamics Basics of Nuclear Magnetic Resonance*. The University of Southampton, UK: John Wiley & Sons, 2nd ed., 2008.

[9] J. Keeler, *Understanding NMR Spectroscopy*. University of Cambridge, Department of Chemistry: James Keeler, 2002.

[10] K. George Kurian, P. Madhu, and G. Rajalakshmi, "Solid-state NMR signals at zero-to-ultra-low-field," *Journal of Magnetic Resonance Open*, vol. 10-11, p. 100049, June 2022.

[11] Y. N. Cheng and E. M. Haacke, "Magnetic Moment of a Spin, Its Equation of Motion, and Precession," *CP Magnetic Resonance Imaging*, vol. 00, Mar. 2001.

[12] Y. N. Cheng and E. M. Haacke, "Signal Detection," *CP Magnetic Resonance Imaging*, vol. 00, Mar. 2001.

[13] J. W. Blanchard, T. Wu, J. Eills, Y. Hu, and D. Budker, "Zero- to ultralow-field nuclear magnetic resonance J-spectroscopy with commercial atomic magnetometers," *Journal of Magnetic Resonance*, vol. 314, p. 106723, May 2020.

[14] D. Budker, "Extreme nuclear magnetic resonance: Zero field, single spins, dark matter. . . ," *Journal of Magnetic Resonance*, vol. 306, pp. 66–68, Sept. 2019.

[15] D. A. Barskiy, J. W. Blanchard, D. Budker, J. Eills, S. Pustelny, K. F. Sheberstov, M. C. D. Tayler, and A. H. Trabesinger, "Zero- to Ultralow-field Nuclear Magnetic Resonance," *Progress in Nuclear Magnetic Resonance Spectroscopy*, vol. 148-149, p. 101558, Aug. 2025. arXiv:2409.09048 [physics].

[16] P. Put, S. Pustelny, D. Budker, E. Druga, T. F. Sjolander, A. Pines, and D. A. Barskiy, "Zero- to Ultralow-Field NMR Spectroscopy of Small Biomolecules," *Anal. Chem.*, vol. 93, pp. 3226–3232, Feb. 2021.

[17] J. Z. Myers, F. Bullinger, N. Kempf, M. Plaumann, A. Ortmeier, T. Theis, P. Povolni, J. Romanowski, J. Engelmann, K. Scheffler, J.-B. Hövener, K. Buckenmaier, R. Körber, and A. N. Pravdivtsev, "Zero to ultralow magnetic field NMR of [1 - 13 C] pyruvate and [2 - 13 C] pyruvate enabled by SQUID sensors and hyperpolarization," *Phys. Rev. B*, vol. 109, p. 184443, May 2024.

[18] Q. Stern and K. Sheberstov, "Simulation of NMR spectra at zero and ultralow fields from A to Z – a tribute to Prof. Konstantin L'vovich Ivanov," *Magn. Reson.*, vol. 4, pp. 87–109, Apr. 2023.

[19] M. C. D. Tayler, T. Theis, T. F. Sjolander, J. W. Blanchard, A. Kentner, S. Pustelny, A. Pines, and D. Budker, "Invited Review Article: Instrumentation for nuclear magnetic resonance in zero and ultralow magnetic field," *Review of Scientific Instruments*, vol. 88, p. 091101, Sept. 2017.

[20] A. Wilzewski, S. Afach, J. Blanchard, and D. Budker, "A method for measurement of spin-spin couplings with sub-mHz precision using zero- to ultralow-field nuclear magnetic resonance," *Journal of Magnetic Resonance*, vol. 284, pp. 66–72, Nov. 2017.

[21] M. Ledbetter, C. Crawford, A. Pines, D. Wemmer, S. Knappe, J. Kitching, and D. Budker, "Optical detection of NMR J-spectra at zero magnetic field," *Journal of Magnetic Resonance*, vol. 199, pp. 25–29, July 2009.

[22] J. Z. Myers, K. Buckenmaier, A. N. Pravdivtsev, M. Plaumann, and R. Körber, "Characterization of Nuclear Magnetism at Ultralow and Zero Field Using SQUIDs," *IEEE Trans. Appl. Supercond.*, vol. 35, pp. 1–5, Aug. 2025.

[23] R. Picazo-Frutos, R. Kircher, J. Eills, G. P. Centers, Y. Hu, J. Qin, S. J. Barker, M. Utz, K. F. Sheberstov, T. Kasajima, S. Okawa, M. Kami, and D. Budker, "Application of magnetoresistive sensors to zero- and ultralow-field nuclear magnetic resonance," June 2025.

[24] T. Coussens, A. Gialopsou, C. Abel, M. G. Bason, T. M. James, W. Evans, M. T. M. Woodley, D. Nightingale, D. Nicolau, L. Page, F. Oručević, and P. Krüger, "A modular optically pumped magnetometer system," *Quantum Sci. Technol.*, vol. 9, p. 035045, July 2024.

[25] R. Picazo-Frutos, K. F. Sheberstov, J. W. Blanchard, E. Van Dyke, M. Reh, T. Sjoelander, A. Pines, D. Budker, and D. A. Barskiy, "Zero-field J-spectroscopy of quadrupolar nuclei," *Nat Commun*, vol. 15, p. 4487, May 2024.

[26] K. Buckenmaier, R. Neumann, F. Bullinger, N. Kempf, P. Povolni, J. Engelmann, J. Samlow, J.-B. Hövener, K. Scheffler, A. Ortmeier, M. Plaumann, R. Körber, T. Theis, and A. N. Pravdivtsev, "Indirect Zero-Field Nuclear Magnetic Resonance Spectroscopy," *Anal. Chem.*, vol. 97, pp. 17336–17344, Aug. 2025.

[27] A. Grosz, M. J. Haji-Sheikh, and S. C. Mukhopadhyay, eds., *High Sensitivity Magnetometers*, vol. 19 of *Smart Sensors, Measurement and Instrumentation*. Cham: Springer International Publishing, 2017.

[28] J. C. Allred, R. N. Lyman, T. W. Kornack, and M. V. Romalis, "High-Sensitivity Atomic Magnetometer Unaffected by Spin-Exchange Relaxation," *Phys. Rev. Lett.*, vol. 89, p. 130801, Sept. 2002.

[29] W. Xiao, Y. Ding, T. Wu, X. Peng, and H. Guo, "Quantum Sensing of Magnetic Fields Using Global Optimization Algorithms," *Phys. Rev. Applied*, vol. 20, p. 024042, Aug. 2023.

[30] S. Esmaeili, P. Schmalenberg, S. Wu, Y. Zhou, S. Rodrigues, N. Hussain, T. Kimura, Y. Tadokoro, S. Higashi, D. Banerjee, and E. M. Dede, "Evolution of quantum spin sensing: From bench-scale odmr to compact integrations," *APL Materials*, vol. 12, p. 040901, 04 2024.

[31] Y. Yang, H. H. Vallabhapurapu, V. K. Sewani, M. Isarov, H. R. Firgau, C. Adambukulam, B. C. Johnson, J. J. Pla, and A. Laucht, "Observing hyperfine interactions of NV centers in diamond in an advanced quantum teaching lab," *American Journal of Physics*, vol. 90, pp. 550–560, July 2022. _eprint: https://pubs.aip.org/aapt/ajp/article-pdf/90/7/550/20102423/550_1_5.0075519.pdf.

[32] J. Sakurai and J. Napolitano, *Modern Quantum Mechanics*. Cambridge University Press, 2017.

[33] B. I. Ionin and B. A. Ershov, *NMR Spectroscopy in Organic Chemistry*. Boston, MA: Springer US, 1995.

[34] A. Consuelo-Leal, A. Araujo-Ferreira, E. Lucas-Oliveira, T. Bonagamba, and R. Auccaise, "NMR Relaxation by Redfield equation in a spin system I = 7 / 2," *Journal of Magnetic Resonance*, vol. 349, p. 107403, Apr. 2023.

[35] R. M. Eisberg and R. Resnick, *Quantum physics of atoms, molecules, solids, nuclei, and particles*. New York: Wiley, 2. ed., 37. [nachdr.] ed., 2009.

[36] H. An and W. Lin, "Spin Density, T_1 , T_2 , T_2 * Relaxation and Bloch Equations," *CP Magnetic Resonance Imaging*, vol. 00, Mar. 2001.

[37] I. V. Zhukov, A. S. Kiryutin, A. V. Yurkovskaya, J. W. Blanchard, D. Budker, and K. L. Ivanov, "Correlation of high-field and zero- to ultralow-field NMR properties using 2D spectroscopy," *The Journal of Chemical Physics*, vol. 154, p. 144201, Apr. 2021.

[38] A. Meraki, L. Elson, N. Ho, A. Akbar, M. Koźbiał, J. Kołodyński, and K. Jensen, "Zero-field optical magnetometer based on spin alignment," *Phys. Rev. A*, vol. 108, p. 062610, Dec. 2023.

[39] C. Munuera-Javaloy, A. Tobalina, and J. Casanova, "Pulse sequence design for high field nmr with nv centers in dipolarly coupled samples," *Scientific Reports*, vol. 15, p. 30956, Aug. 2025.

[40] P. Reuschel, A. M. Flatae, F. Sledz, and M. Agio, *Optically Detected Magnetic Resonance (ODMR): University of Siegen MANUAL Master Lab Course*. Nano-Optics Group, University of Siegen, 2024. Version 1.3.1.

[41] S. Sengottuvel, O. Dhungel, M. Mrózek, A. Wickenbrock, D. Budker, W. Gawlik, and A. M. Wojciechowski, "Microwave-free imaging magnetometry with nitrogen-vacancy centers in nanodiamonds at near-zero field," *arXiv preprint arXiv:2409.02199*, Sept. 2024.

[42] B. Andrews, M. Lai, Z. Wang, N. Kato, M. C. D. Tayler, E. Druga, and A. Ajoy, "Sensitive multichannel zero-to ultralow-field nmr with atomic magnetometer arrays," *PNAS Nexus*, vol. 4, p. pgaf187, June 2025.

[43] S. J. Brooks, G. Mahler, J. Cintorino, and A. K. Jain, "PRODUCTION OF LOW COST, HIGH FIELD QUALITY HALBACH MAGNETS," 2017.

[44] B. Biswas, "A magnetic quadrupole from rectangular permanent magnets," *Nuclear Instruments and Methods in Physics Research Section A: Accelerators, Spectrometers, Detectors and Associated Equipment*, vol. 605, pp. 233–242, July 2009.

[45] A. N. Pravdivtsev, K. Buckenmaier, N. Kempf, G. Stevanato, K. Scheffler, J. Engelmann, M. Plaumann, R. Koerber, J.-B. Hövener, and T. Theis, "LIGHT-SABRE Hyperpolarizes 1-^{13} C-Pyruvate Continuously without Magnetic Field Cycling," *J. Phys. Chem. C*, vol. 127, pp. 6744–6753, Apr. 2023.

[46] D. Manzano, "A short introduction to the Lindblad Master Equation," *AIP Advances*, vol. 10, p. 025106, Feb. 2020. arXiv:1906.04478 [quant-ph].

[47] J. Yong, *Optimising NMR Spectroscopy Through Method and Software Development*. Springer Theses, Cham: Springer Nature Switzerland, 2024.

[48] I. Kuprov, *Spin: From Basic Symmetries to Quantum Optimal Control*. Cham: Springer International Publishing, 2023.

[49] P. D. Nation, J. R. Johansson, A. J. G. Pitchford, C. Granade, A. L. Grimsmo, N. Shammah, S. Ahmed, N. Lambert, B. Li, J. Lishman, S. Cross, and E. Giguère, "QuTiP 2: A Python framework for the dynamics of open quantum systems," vol. 184, 2013.

[50] M. C. Tayler and L. F. Gladden, "Scalar relaxation of NMR transitions at ultralow magnetic field," *Journal of Magnetic Resonance*, vol. 298, pp. 101–106, Jan. 2019.

[51] H. Gilboa, B. E. Chapman, and P. W. Kuchel, "Spin–Lattice Relaxation Times of H2and D2in Aqueous Solutions," *Journal of Magnetic Resonance, Series A*, vol. 119, pp. 1–5, Mar. 1996.

[52] N. Bloembergen, E. M. Purcell, and R. V. Pound, "Relaxation Effects in Nuclear Magnetic Resonance Absorption," *Phys. Rev.*, vol. 73, pp. 679–712, Apr. 1948.

[53] W. G. Nagourney, *Quantum Electronics for Atomic Physics*. Oxford Graduate Texts, Oxford: Oxford University Press, 2010.

[54] S. J. W. Jorge Nocedal, *Numerical Optimization*. Scholars Portal, 2019. OCLC: 1339961469.

[55] P. R. Bevington and D. K. Robinson, *Data reduction and error analysis for the physical sciences*. Boston Burr Ridge: McGraw-Hill, 3rd ed. ed., 2003.

[56] R. C. Aster, B. Borchers, and C. Thurber, *Parameter Estimation and Inverse Problems*. Rick Aster, Brian Borchers, and Cliff Thurber, 2004.

[57] A. G. Palmer Iii, "NMR Probes of Molecular Dynamics: Overview and Comparison with Other Techniques," *Annu. Rev. Biophys. Biomol. Struct.*, vol. 30, pp. 129–155, June 2001.

[58] K. Levenberg, "A method for the solution of certain non-linear problems in least squares," *Quart. Appl. Math.*, vol. 2, pp. 164–168, July 1944.

[59] D. W. Marquardt, "An Algorithm for Least-Squares Estimation of Nonlinear Parameters," *Journal of the Society for Industrial and Applied Mathematics*, vol. 11, pp. 431–441, June 1963.

[60] Björck, *Numerical Methods for Least Squares Problems*. Society for Industrial and Applied Mathematics, 1996.

[61] R. Fletcher, *Practical methods of optimization; (2nd ed.)*. USA: Wiley-Interscience, 1987.

[62] G. A. F. Seber and C. J. Wild, *Nonlinear regression*. New York: Wiley, 2004. OCLC: 1058205756.

[63] J. J. Moré, "The levenberg-marquardt algorithm: Implementation and theory," in *Numerical Analysis* (G. A. Watson, ed.), (Berlin, Heidelberg), pp. 105–116, Springer Berlin Heidelberg, 1978.

[64] K. Madsen, H. Nielsen, and O. Tingleff, "Methods for Non-Linear Least Squares Problems (2nd ed.)," p. 60, Jan. 2004.

[65] H. P. Gavin, "The Levenberg-Marquardt algorithm for nonlinear least squares curve-fitting problems," 2024.

[66] M. K. Transtrum and J. P. Sethna, "Improvements to the Levenberg-Marquardt algorithm for nonlinear least-squares minimization," Jan. 2012. arXiv:1201.5885 [physics].

[67] W. Press, *Numerical Recipes 3rd Edition: The Art of Scientific Computing*. Numerical Recipes: The Art of Scientific Computing, Cambridge University Press, 2007.

[68] D. Bates and D. Watts, *Nonlinear Regression Analysis and Its Applications*. 05 2008.

[69] N. A. Farrow, R. Muhandiram, A. U. Singer, S. M. Pascal, C. M. Kay, G. Gish, S. E. Shoelson, T. Pawson, J. D. Forman-Kay, and L. E. Kay, "Backbone Dynamics of a Free and a Phosphopeptide-Complexed Src Homology 2 Domain Studied by 15N NMR Relaxation," *Biochemistry*, vol. 33, pp. 5984–6003, May 1994.

[70] J. Taylor, *An Introduction to Error Analysis: The Study of Uncertainties in Physical Measurements*. ASMSU/Spartans.4.Spartans Textbook, University Science Books, 1997.

[71] H. Motulsky and A. Christopoulos, *Fitting Models to Biological Data Using Linear and Nonlinear Regression: A practical guide to curve fitting*. Oxford University PressNew York, NY, May 2004.

[72] W. M. Haynes, ed., *CRC Handbook of Chemistry and Physics*. Boca Raton, FL: CRC Press, 97 ed., 2016.

[73] G. Lindblad, "On the generators of quantum dynamical semigroups," *Communications in Mathematical Physics*, vol. 48, p. 119, 1976.